I. Meridional Energy Balance of Uranus

II. Viscosity of Rock-Ice Mixtures

III. The Thermosphere of Titan

Thesis by

Andrew James Friedson

In partial fulfillment of the requirements

for the degree of

Doctor of Philosophy

California Institute of Technology

Pasadena, California

1987

(submitted August 8, 1986)

To Dena and Bob

Acknowledgements

I wish to express my heartfelt thanks to Dr. Andy Ingersoll for suggesting the topic of Part I of this thesis, and for his invaluable guidance and insight. Andy deserves special thanks for pulling a scrawny, dripping wet fourth-year graduate student out of the drink and setting him to work on a problem that has plagued man's curiosity since the dawn of time: the meridional energy balance of Uranus. Thanks, Andy, for your confidence, patience, support, and fabulous 4th of July parties.

I am also grateful to Dr. Dewey Muhleman for taking a little of the ivory out of the ivory tower around here. Dewey has helped put life at Caltech in the proper perspective. Dewey, I owe you a French vanilla on a cup cone. (I know this is extremely generous of me, but you deserve it.)

I wish to thank Dr. Dave Stevenson for suggesting the subject of Part II, and for always being willing to drop what he was doing to answer a question. Thanks also, Dave, for organizing so many marvelous hikes.

I am grateful to Dr. Yuk Yung for proposing the topic of Part III, my first research topic in Planetary Science. I feel that Yuk has always had a sincere interest in my

progress and welfare during my graduate career, and for that I will always be very grateful.

I also wish to thank Dr. Peter Goldreich for encouraging me to come to Planetary Science at Caltech and for the flattering opportunity to give some lectures in his Uranus course. May your jump shot swish and your serve terrify, Peter. I thank Dr. Robert Sharp for organizing Project Pahoehoe 1986, which was a wonderful experience.

Special thanks go to Drs. Mark Allen, Dave Crisp, and Richard Zurek for stimulating scientific discussions.

To my fellow graduate students and friends Dan, Tony, Randy, Jim, Mary, Andy, Don, Todd and Maria, Mike, Randy, Don, Cindy, Carol, Ken and Lottie, Greg, Tim, Arie, and many others (you know who you are), thanks for your friendship and commiseration during the gnarly times. I look forward to heckling some of you at conferences.

Last but not least, thanks to Kay Campbell and Donna Lathrop for invaluable assistance in many areas. You ladies have made it (nearly) a joy to come into work in the morning.

Abstract

Part I:

The seasonal meridional energy balance and thermal structure of the atmosphere of Uranus is investigated using a two-dimensional radiative-convective-dynamical model. Diurnal-average temperatures and heat fluxes are calculated as a function of pressure, latitude, and season. In addition to treating radiation and small-scale convection in a manner typical of conventional radiative-convective models, the dynamical heat fluxes due to large-scale baroclinic eddies are included and parameterized using a mixing length formulation (Stone, 1972; Ingersoll and Porco, 1978). The atmosphere is assumed to be bounded below by an adiabatic, fluid interior with a single value of potential temperature at all latitudes. The internal heat flux is found to vary with latitude and season. The total internal power and the global enthalpy storage rate are seen to oscillate in phase with a period of 1/2 Uranian year. On an annual-average basis, equatorward heat transport can take place in both the atmosphere and the convective interior. For a weak internal heat source, the meridional transport takes place predominantly in the atmosphere. If the internal heat source is larger, a greater share of the transport is taken up by the interior. For a value of the

internal heat near the current upper limit for Uranus (~27% of the absorbed sunlight), about 1/3 of the equatorward heat transport at mid-latitudes occurs in the interior. For a given internal heat source, placing the peak of the solar heating at high altitudes or depositing the solar energy into a narrow altitude range favors heat transport by the atmosphere over the interior. Deep penetration of sunlight favors transport by the interior. For the time corresponding to the Voyager 2 Uranus encounter, the effective temperature at the south (sunlit) pole is calculated to be ~1.5 K higher than that at the equator. Horizontal contrasts of the mean 450-900 mbar temperature are found to be $\lesssim$1.5 K, in fair agreement with Voyager 2 IRIS results (Hanel et al., 1986), but the model fails to reproduce the local minimum in this temperature seen at 30°S. Nevertheless, it is concluded that meridional heat transport in the atmosphere is efficient in keeping seasonal horizontal temperature contrasts below those predicted by radiative-convective models (Wallace, 1983).

Part II:

Theory and experiments are used to establish lower and upper bounds on the ratio of actual viscosity to pure ice viscosity for a suspension of rock particles in a water ice matrix. For typical conditions encountered in icy satellites, this ratio is of order ten or possibly larger,

depending on unknown factors such as the particle size distribution. It is shown that even this modest increase in viscosity may be enough to have caused a failure of solid-state convective self-regulation early in the evolution of a homogeneous, rock-water ice satellite, provided the satellite is large enough and sufficiently silicate-rich. The criteria for this failure are satisfied by Ganymede and are marginal for Callisto, if the silicates are hydrated. Failure of self-regulation means that the viscosity is too high for the interior to remain completely solid and eliminate the heat production of long-lived radioisotopes by solid state convection. Partial melting of the ice then occurs. It is further shown that satellites of this size may then undergo runaway differentiation into a rock core and almost pure ice mantle, because the gravitational energy release is sufficient to melt nearly all the ice, and the Rayleigh-Taylor instability time scale is short. (Although the high pressure phases of ice melt, the resulting water quickly refreezes at a higher level.) We conjecture that these results explain the striking surface dissimilarity of Ganymede and Callisto, if these satellites accreted cold and undifferentiated. Ganymede may have gone supercritical (melted and differentiated) because of a failure of self-regulation, whereas Callisto remained undifferentiated to the present day. Like all proposed explanations for the Ganymede-Callisto dichotomy, this conjecture cannot be

quantified with confidence, because of inadequate or incomplete observations, theory and experimental data.

Part III:

The diurnal variation of the vertical structure of Titan's thermosphere is calculated through simultaneous solution of the equations of heat transfer and hydrostatic equilibrium. The temperature and density profiles are found above the mesopause. The dynamical response of the thermosphere to heating is for the most part neglected. Nevertheless, we are able to draw some interesting qualitative and quantitative conclusions regarding the vertical structure. Heating of the upper thermosphere occurs primarily through absorption of solar Lyman α radiation by methane, with an additional amount of heating ($\lesssim$20%) due to low-energy magnetospheric electron precipitation. The heat is conducted downward to the mesopause, where it is removed by IR cooling due principally to acetylene. The mesopause is found to occur where the density is 2.2×10^{12} cm^{-3} (736 km) and has a temperature of ~110 K. The exospheric temperature is unlikely to exceed 225 K in the course of a Titan day. The diurnally averaged exospheric temperature is in the range 187-197 K, depending on the amount of magnetospheric electron heating that is included in the model. The amplitude of the diurnal variation is found to be $\lesssim$28 K. We find that the vertical

extent of the hydrogen cloud is too large to be explained in terms of simple thermal escape of hydrogen from a ~225 K exosphere and conclude that other processes must be important for populating or heating the neutral torus.

Table of Contents

List of Figures

Part I:

Part III:

List of Tables

Part II:

PART I. Seasonal Meridional Energy Balance and Thermal Structure of the Atmosphere of Uranus: A Radiative-Convective-Dynamical Model

Chapter 1

INTRODUCTION

This study is concerned with the nature of the meridional (north-south) heat transport on Uranus, which develops in response to the uneven solar heating of its atmosphere. On Earth, and on every other planet with an atmosphere except Uranus, more sunlight is deposited on average at the equator than at the poles. Due to its large obliquity, Uranus receives more sunlight at the poles than at the equator over the Uranian year. Differential solar heating in a planetary atmosphere drives a global circulation that acts to reduce the temperature difference between the equator and poles. Theory and experiment predict that the character of the circulation should depend on the rotation rate, radius, and obliquity of the planet, on the depth and radiative time constant of its atmosphere, and perhaps on the strength of the internal heat source of the planet and on other parameters as well.

It is of particular interest in the study of planetary atmospheres to be able to classify their circulation according to some set of governing physical parameters. One way to make progress on this problem is to compare the circulation and meridional heat budget of one planet to another. For example, Jupiter differs from Earth in several

ways: it has no solid surface at the base of its atmosphere; its internal heat source nearly equals the absorbed solar input; it rotates twice as fast; it has a very different chemical composition. How are these differences manifested in the meridional energy balance of the two planets?

On Earth, the poleward heat flux in the atmosphere at mid-latitudes is dominated by the action of baroclinic eddies. The term "eddy" refers to that component of the total wind which represents a deviation from the zonal (east-west) mean wind. In other words, eddies represent those components of the wind field that vary with longitude. In satellite photographs of the Earth, they appear as wavelike features in the cloud patterns at mid-latitudes. These eddies originate from the baroclinic instability of the basic state zonal wind. They draw their energy from the available potential energy associated with the equator-to-pole temperature gradient, and in the process they transport warm air upward and poleward, cold air downward and equatorward. Hence, they transport heat not only from the hot equator to the poles but upward as well. In reality, the heat flux due to baroclinic eddies amounts to only one-half the total poleward heat flux at Earth's mid-latitudes. The other half is associated with the oceanic circulation and with the latent heat of water vapor (Palmen and Newton, 1969).

Peter Stone found he could make qualitatively useful estimates of the Earth's equator-to-pole temperature difference, static stability (i.e., vertical gradient of potential temperature), horizontal eddy velocity, and horizontal eddy length scale by using a simple radiative-dynamical model (Stone, 1972). The model is applicable only to rapidly rotating planets. It is assumed that radiative fluxes in the atmosphere are entirely balanced by dynamical heat fluxes due to baroclinic eddies. The baroclinic instabilities that form the eddies are assumed to grow to a size where their meridional velocities are comparable to the zonal velocity difference from top to bottom in the baroclinic atmosphere. The contribution of small-scale convection to the vertical heat transport is ignored.

Despite these simplifications, Stone's model yielded reasonable estimates of the equator-to-pole temperature difference, static stability, and properties of the eddies for the Earth and Mars. He concluded that his model gave a much more realistic description of the thermal and dynamical state of these planets than could be obtained from the traditional assumption of radiative-convective equilibrium. He applied his model to Jupiter as well. To do so, he was forced to make two additional simplifying assumptions. First, he assumed that the flux of heat from the interior is uniformly distributed over the surface of the planet. Second, he assumed that heat-transporting motions are

confined to a depth of a few scale heights in the neighborhood of the cloud tops. He found that, as a consequence of Jupiter's great size and large internal heat source, baroclinic eddies should be relatively ineffective in transporting heat poleward. This implied that the final dynamical state should lie close to the state determined by one-dimensional radiative-convective equilibrium at each latitude. Stone's model predicted the equator-to-pole temperature difference on Jupiter should be 30 K.

This prediction was made before any spacecraft visited Jupiter. Infrared measurements by the Pioneer 10 and 11 spacecraft (Ingersoll et al., 1976) established that the poles were no more than 3 K colder than the equator. Hence, Stone's model fails to predict the equator-to-pole temperature difference on Jupiter by an order of magnitude, indicating that this planet responds to the differential solar heating of its atmosphere in a way different from Earth and Mars.

To explain the small equator-to-pole temperature gradient on Jupiter, Ingersoll (1976) proposed that the internal heat flux is non-uniform with latitude and balances the absorbed sunlight, in the sense that within each band of latitude the visible atmosphere receives as much solar and internal energy as it emits to space. The poleward atmospheric heat transport is then zero. All the poleward heat transport takes place in Jupiter's convective interior.

Turbulent convection maintains the interior in a nearly isentropic state, with every portion of the fluid lying close to the same adiabat. Consequently, temperature variations on constant pressure surfaces are extremely small. Ingersoll and Porco (1978) showed that an equator-to-pole temperature difference at the 1 bar level of only .02 K could depress the internal flux at the equator relative to the poles by an amount sufficient to balance the difference in the solar flux.

For this model to work, the net (emitted infrared minus absorbed solar) irradiance must be positive at all latitudes. This requirement insures that at all latitudes the internal heat flux is directed upward. This is necessary since locally driven free convection can carry heat only upward, never downward. When the infrared flux emitted to space is nearly uniform with latitude, as on Jupiter, the net irradiance can be positive at all latitudes only if the internal luminosity exceeds a certain critical value. Ingersoll and Porco determined the critical internal luminosity for Jupiter is equal to 27% of the absorbed sunlight.

After the Pioneer and Voyager missions to Jupiter, it appeared that the meridional energy balance of planetary atmospheres has to be divided into two regimes. Stone's (1972) radiative-dynamical model makes useful estimates of the thermal state and dynamical regime for the rapidly

rotating terrestrial planets, Earth and Mars. The meridional heat budget of these planets is fairly well described by a balance between radiative fluxes and dynamical heat fluxes due to baroclinic eddies. For Jupiter, Saturn, and Neptune, which all appear to have internal luminosities exceeding their critical value (Hanel et al., 1981; Hanel et al., 1983; Moseley et al., 1985), the model of Ingersoll and Porco (1978) seems more appropriate. For these planets the convective interior short-circuits the atmosphere in transporting heat.

The question arises of how to classify the meridional energy balance of Uranus according to the above scheme. Uranus is, of course, a Jovian planet with a deep atmosphere that merges smoothly with a presumably convective fluid interior. Therefore, Stone's radiative-dynamical model would seem to be inapplicable to Uranus. However, Uranus has a relatively low internal luminosity (Pollack et al., 1986), and the infrared emission to space is nearly uniform with latitude (Hanel et al., 1986). As a result, the annual average of the net irradiance is very likely to be negative in the polar regions. In addition, due to its large obliquity, Uranus experiences large seasonal variations in insolation, especially near the poles. Since the radiative time constant of the atmosphere is longer than a Uranian year (Stone, 1973), the infrared emission remains nearly constant with season. Therefore, during the solstices when

the sun is directly over the summer pole, the net irradiance becomes very negative in the sunlit hemisphere. It is clear that on both a seasonal and annual-average basis, the applicability of Ingersoll and Porco's model to Uranus must break down.

The radiative-convective-dynamical model presented here has been developed for the purpose of modeling the meridional energy balance of Uranus. As its name implies, it draws features from both Stone's radiative-dynamical model and the model of Ingersoll and Porco. As in Stone's calculations, the dynamical heat fluxes are assumed to be due to baroclinic eddies. Small-scale convection is also included, however. The lower boundary condition of the model is based on the work of Ingersoll and Porco: the deep atmosphere and fluid interior are taken to be adiabatic, with the same adiabat applying at all latitudes.

The results presented in the following chapters will show that the meridional energy balance of Uranus is intermediate between the terrestrial and jovian regimes. Both the visible atmosphere and interior of Uranus participate in the meridional heat transport. In Chapter 2, the radiative-convective-dynamical model is described, and the results of a steady-state calculation of the meridional energy balance are presented. In addition, the concept of terrestrial and jovian regimes is introduced in Chapter 2, and a detailed discussion is given of the behavior of the

heat fluxes in each regime. A model for the seasonal meridional energy balance is presented in Chapter 3. Some predictions of the seasonal model are compared in detail with recent data collected by the Voyager 2 spacecraft at Uranus. The overall equator-to-pole temperature contrast predicted by the seasonal model compares favorably with Voyager 2 IRIS observations (Hanel et al., 1986), but smaller-scale structure in the IRIS data is not reproduced. Some of the implications of the Voyager 2 observations at Uranus are discussed in Chapter 4, and some new questions are posed regarding the thermal state and dynamical regime of Uranus' atmosphere.

References

HANEL, R. A., B. J. CONRATH, L. W. HERATH, V. G. KUNDE, AND J. A. PIRRAGLIA (1981). Albedo, internal heat, and energy balance of Jupiter: Preliminary results of the Voyager infrared investigation. J. Geophys. Res. 86, 8705-8712.

HANEL, R. A., B. J. CONRATH, V. G. KUNDE, J. C. PEARL, AND J. A. PIRRAGLIA (1983). Albedo, internal heat, and energy balance of Saturn. Icarus 53, 262-285.

HANEL, R., B. CONRATH, F. M. FLASAR, V. KUNDE, W. MAGUIRE, J. PEARL, J. PIRRAGLIA, R. SAMUELSON, D. CRUIKSHANK, D. GAUTIER, P. GIERASCH, L. HORN, AND P. SCHULTE (1986). Infrared observations of the Uranian system. Science 233, 70-74.

INGERSOLL, A.P. (1976). Pioneer 10 and 11 observations and the dynamics of Jupiter's atmosphere. Icarus 29, 245-253.

INGERSOLL, A. P., G. MUNCH, G. NEUGEBAUER, AND G. S. ORTON (1976). Results of the infrared radiometer experiment on Pioneers 10 and 11. In Jupiter (T. Gehrels, Ed.), pp. 197-205. University of Arizona Press, Tucson.

INGERSOLL, A.P., AND C.C. PORCO (1978). Solar heating and internal heat on Jupiter. Icarus 35, 27-43.

MOSELEY, H., B. CONRATH, AND R.F. SILVERBERG (1985). Atmospheric temperature profiles of Uranus and Neptune. Astrophys. J. 292, L83-L86.

PALMEN, E. AND C. W. NEWTON (1969). Atmospheric Circulation Systems. Academic Press, New York.

POLLACK, J. B., K. RAGES, K. H. BAINES, J. T. BERGSTRALH, D. WENKERT, AND G. E. DANIELSON (1986). Estimates of the bolometric albedos and radiation balance of Uranus and Neptune. Submitted to Icarus.

STONE, P.H. (1972). A simplified radiative-dynamical model for the static stability of rotating atmospheres. J. Atmos. Sci. 29, 405-418.

STONE, P.H. (1973). The dynamics of the atmospheres of the major planets. Space Sci. Rev. 14, 444-459.

Chapter 2

THE STEADY-STATE MODEL

1. Introduction

In this chapter, a steady-state model for the meridional energy balance of the atmosphere of Uranus will be presented. The calculation finds the response of the atmosphere to a steady condition of insolation. At each latitude, the incident solar flux is taken to be equal to the annual average of the seasonally varying sunlight.

The radiative-convective-dynamical model is described in Section 2. A detailed account is given of the numerical technique used for the calculations and of the treatment of the radiative, convective, dynamical, and internal heat fluxes.

The results of the steady-state model are presented in Section 3. In particular, the concept of terrestrial and jovian regimes is introduced. The meridional energy balance is shown to have a distinct character in each regime. The behavior of the internal heat flux in the terrestrial and jovian regimes, and its relation to their thermal structure, is discussed.

Section 4 begins with a summary of the results of this chapter and concludes with the presentation of a scaling

analysis, which indicates that seasonal variations are likely to be important in the meridional energy balance of Uranus. The seasonal meridional energy balance is discussed in Chapter 3. The utility of the steady-state model lies in its time-independent exposition of most of the phenomena to be encountered in the seasonal model. The concept of jovian and terrestrial regimes, for example, carries over to the seasonal model with only slight modification. In addition, the steady-state model provides some indication of what the meridional energy balance might be like on a planet with weak seasonal variations, such as Jupiter.

2. Description of the Model

The steady-state model calculates the zonally averaged equilibrium temperatures and heat fluxes, including the solar and radiative thermal fluxes, the small-scale convective flux, and the dynamical flux due to large-scale eddy motions. This equilibrium state develops from arbitrary initial conditions for fixed values of the annual-average solar heating and potential temperature of the deep atmosphere.

The potential temperature of the deep adiabat is treated as an input parameter. (Recall that potential temperature is constant on an adiabat.) It is assumed in the model that convective currents can maintain the deep atmosphere and

fluid interior in a nearly isentropic state. All fluid particles lie close to the same adiabat, so potential temperature variations in the deep atmosphere and interior of a Jovian planet are extremely small (Ingersoll and Porco, 1978). This assumption is reasonable if Uranus emits more energy than it receives from the sun. The assumption probably breaks down if Uranus' interior is not cooling off. For a given deep adiabat and a given planetary albedo, the model computes the ratio of emitted power to absorbed sunlight. Therefore, in practice, this ratio is varied by varying the input potential temperature of the deep adiabat.

The model numerically integrates the time-dependent heat equation on a pressure-latitude grid until a steady state is achieved. The grid has five pressure levels per pressure scale height between 20 bar and 12 mbar. The uppermost interval extends from 12 mbar to zero pressure. Most of the model calculations have been done with 9° steps in latitude from equator to pole. Some of these calculations were repeated with 4.5° steps, and it was found that the heat fluxes obtained were the same to within 5%, whether the smaller latitude interval or the larger one was used. With this grid the atmosphere of Uranus above the 20 bar pressure level can be viewed as being divided into a series of bins. Each bin can be regarded as a zonal ring of fluid, at a uniform temperature, centered on a particular latitude and pressure level. At each time step, the energy flowing into

and out of each bin is calculated, and the temperature of the bin is increased or decreased accordingly to conserve energy. The time-marching continues until the flux divergence in any bin is $<10^{-6}$ its initial value. The change in the temperature is found using the thermodynamic energy equation (Landau and Lifshitz, 1959; p. 185):

$$\rho T \frac{dS}{dt} = - \text{div } \mathbf{F} \qquad (2.1)$$

where ρ is the mass density, T the temperature, S the entropy/unit mass of the fluid, and **F** is the total heat flux at a given pressure and latitude. In Eq. (2.1), viscous dissipation and heat conduction in the fluid are ignored. The potential temperature can be defined through the equation

$$S = C_p \ln \theta \qquad (2.2)$$

where C_p is the specific heat at constant pressure. If C_p is taken to be independent of temperature and pressure, then the temperature and potential temperature are related at any point in the atmosphere by

$$T = \theta \, (p/p_0)^{\kappa} \qquad (2.3)$$

where p_0 is the reference pressure, taken to be 20 bars, and $\kappa = R/C_p$, where R is the gas constant. It is convenient to combine Eqs. (2.1), (2.2), and (2.3) in order to express the thermodynamic energy equation in terms of the potential temperature:

$$\rho C_p (p/p_0)^{\kappa} \frac{d\theta}{dt} = - \text{div } \mathbf{F} \qquad (2.4)$$

An equivalent form of equation (2.4) is found by integrating it over the mass element represented by one bin of the model while holding θ constant over the bin. This integrated form of the equation is the one actually used in the numerical calculation. It has the advantage of rigorously enforcing energy conservation in the model, since all energy transferred out of one mass element (bin) appears in adjacent elements.

The atmosphere is taken to be composed of a mixture of 87% mole-fraction hydrogen, 10% helium, and 3% methane. The temperature dependence of the specific heat at constant pressure, C_p, has been ignored in the model. Instead, C_p is taken to have a constant value of 3R. This is a rather crude approximation. The actual temperature dependence of the specific heat of H_2 at low temperatures is known to depend on the kinetics of the equilibration process between the ortho and para states of hydrogen (Conrath and Gierasch,

1984). If the rate of conversion between ortho and para hydrogen in Uranus' atmosphere is sufficiently rapid, so that the system can be regarded as being in complete thermodynamic equilibrium at the local temperature, then the specific heat of the atmosphere would be as high as 4.5R at temperatures between 50-100 K. If the conversion between ortho and para H_2 is kinetically inhibited, the specific heat in the same temperature range would be as low as 2.5R. Unfortunately, the kinetics of H_2 ortho-para equilibration are not sufficiently understood to allow a theoretical calculation of the temperature dependence of the specific heat of Uranus' atmosphere. Hence, a temperature-independent value of C_p was chosen to simplify the calculations. The value of 3R used for C_p in the model represents a compromise between the extreme values mentioned above.

The total heat flux appearing on the right side of Eq. (2.4) is the sum of the thermal infrared flux, the solar flux, the convective flux, and the dynamical heat flux due to baroclinic eddies. Only the dynamical heat flux is considered to have a horizontal component. Details of the calculation of each of these fluxes are given below.

Thermal Infrared Flux. Before the thermal infrared radiative flux can be calculated, the atmospheric opacity at infrared wavelengths must be specified. For the low temperatures of Uranus' atmosphere, the thermal emission is

appreciable only in the 0-1500 cm^{-1} spectral region. Within this wavenumber range, the opacity is taken to be due entirely to pressure-induced absorption from H_2-H_2 and H_2-He collisions. This absorption is the dominant source of opacity between 200 cm^{-1} and 800 cm^{-1} on Jupiter and Saturn (Hanel et al., 1979; Hanel et al., 1981). It is expected to be particularly dominant on Uranus because other species, such as ammonia, which are found to contribute to the opacity on Jupiter and Saturn, condense out at the low temperatures characteristic of Uranus' upper troposphere and stratosphere. A semi-empirical fit of the temperature-dependent absorption coefficient for H_2-H_2 collisions is provided by Dore et al. (1983), and for H_2-He collisions by Cohen et al. (1982). The absorption coefficient is affected by the ortho-para hydrogen fraction. Here this fraction is assumed to be determined by thermal equilibrium at the ambient temperature. Some evidence to support this assumption is provided by analysis of the equivalent widths of H_2 (4-0) quadrupole S(0) and S(1) spectral lines (Bergstralh and Baines, 1984).

Given the opacity, the monochromatic infrared fluxes are found at each pressure level using the two-stream approximation to the radiative transfer equation (Chandrasekhar, 1960). Monochromatic fluxes are calculated at equal 10 cm^{-1} wavenumber intervals between 0 and 1500 cm^{-1}. These

monochromatic fluxes are then integrated over wavenumber to obtain the total thermal infrared flux at each pressure level.

Solar Flux. Since seasons are ignored, the latitudinal variation of incident sunlight corresponds to the annual average deposition. The annual-average incident solar flux at latitude λ is proportional to $E(\cos\lambda)$, where E is the complete elliptic integral of the second kind (Wallace, 1983; the derivation is in his Appendix). Wallace (1980) modeled the vertical distribution of the net solar flux in Uranus' visible atmosphere. His model includes absorption by methane, Rayleigh and Raman scattering by hydrogen, some absorption and scattering by a thin haze near 1 bar, and a dense, non-conservative cloud at 3 bars. Subsequent observations at visible and near-infrared wavelengths (Bergstralh and Baines, 1984) suggest that some aspects of this model require modification. For example, Bergstralh and Baines place an opaque cloud near 2 bars and assign different optical properties to the haze. Consequently, the response of the model is found to two different profiles for the solar heating. For each profile, the total solar flux at each level is found by multiplying the incident solar flux by a transmission function. The altitude derivative of the total solar flux is then calculated numerically to produce the solar heating profile. The first model (henceforth designated NC for "no cloud") assumes a smooth

Figure 2-1. Two models for the solar heating used in the calculations. NC = No-cloud model. C = Cloud model.

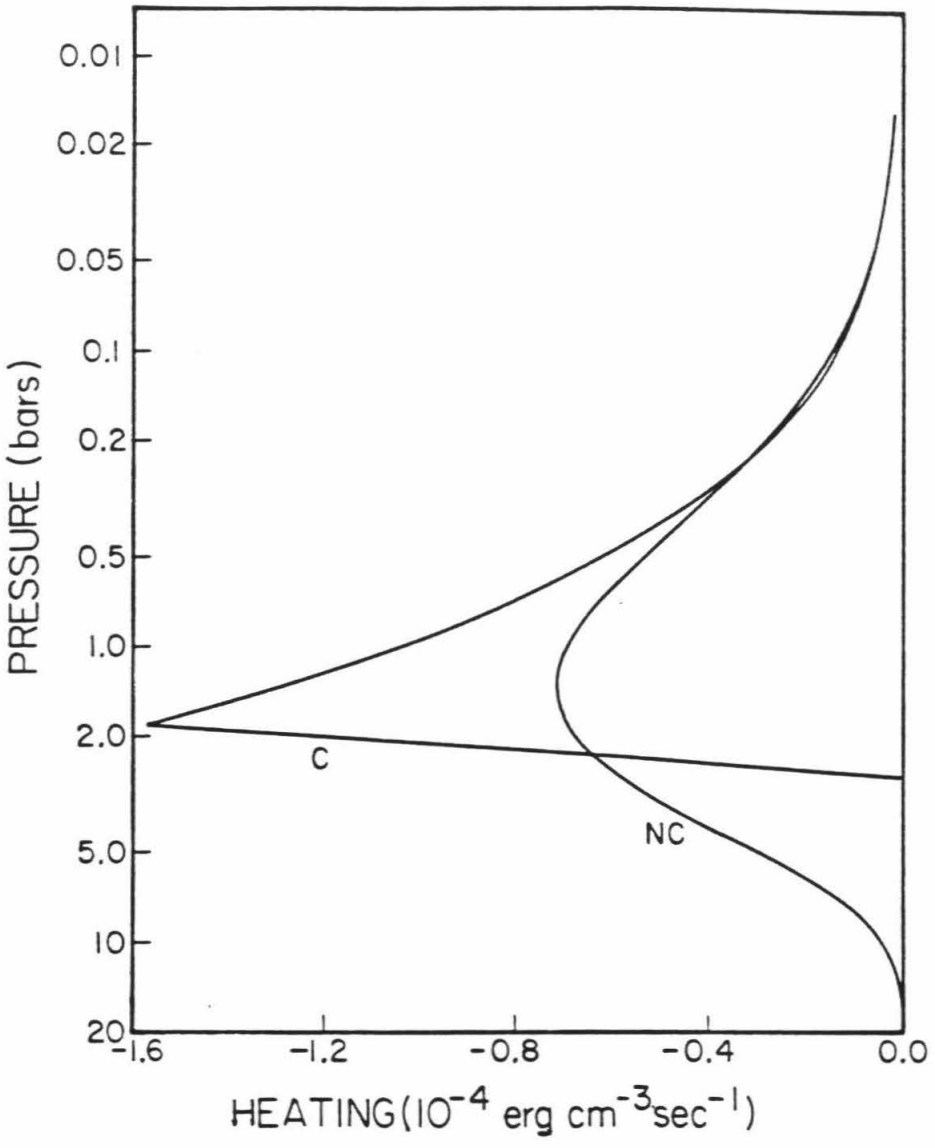
0.01
0.02
0.05
0.1
0.2
0.5
1.0
2.0
5.0
10
20
PRESSURE (bars)
C
NC
-1.6
-1.2
-0.8
-0.4
0.0
HEATING(10^-4 erg cm^-3 sec^-1)

solar deposition unaffected by clouds or aerosol scattering. This model allows the solar flux to penetrate quite deeply into the visible atmosphere. The other model (designated C) is the parameterized fit to Wallace's (1980) solar flux profile with the exception that an opaque, non-conservative, cloud is placed at 1.8 bars. The cloud has the effect of introducing a very sharp peak in the solar heating curve and a steep drop to zero solar heating just below 1.8 bars. The two models for the solar heating are plotted in Figure 2-1.

Dynamical Heat Flux. Dynamical heat fluxes in the model are assumed to occur through the action of large-scale eddies that result from the baroclinic instability of a zonal wind. The calculation of these fluxes is based on a mixing-length theory of sloping convection introduced by Ingersoll and Porco (1978). In this mixing-length formulation, both small-scale convective and large-scale eddy heat fluxes are parameterized in terms of the local gradient of potential temperature:

$$F_v = \frac{p}{\kappa T}\left(\frac{g}{T}\right)^{3/2} \frac{l_V^2}{f^2}\left(\beta|\nabla\theta|\right)^{5/2} \cos^3\frac{\psi}{2} \qquad (2.5a)$$

$$F_H = -F_v \tan\frac{\psi}{2}\,\mathrm{sgn}\left(\frac{\partial\theta}{\partial\phi}\right) \qquad (2.5b)$$

$$\cos \psi = - (\partial\theta/\partial z)/|\nabla\theta| \qquad (2.5c)$$

Here, F_V and F_H are the vertical and horizontal components of the dynamical heat flux, p is the local pressure, T is the temperature, g is the gravitational constant, l_V is a vertical mixing length, f is the local coriolis parameter, $\beta = (p/p_o)^\kappa$, and ϕ is the colatitude. The angle ψ is such that $\pi-\psi$ is the angle between lines of constant potential temperature and the horizontal. Alternatively, $\pi-\psi$ can be regarded as the angle between $\nabla\theta$ and the upward vertical direction.

A number of important features of the theory contained in Eqs. (2.5a)-(2.5c) will now be discussed. When $\psi \approx 0$, $\nabla\theta$ points nearly directly downward in the atmosphere, and the stratification is unstable; i.e., $\partial\theta/\partial z < 0$. (The stratification is unstable in the sense that a parcel displaced upward from its equilibrium position will be buoyant relative to its surroundings and will continue to rise, the opposite being true in a stably stratified environment. This terminology is in standard use in meteorology; e.g., see Holton, 1979, p. 50). Actually, by (2.5c), any value of $\psi < \pi/2$ implies unstable stratification. For unstable stratification, the motions are expected to have the properties of small-scale convection. Note that in Eqs. (2.5a)-(2.5c), for $\psi \approx 0$, $|F_H/F_V| = \tan(\psi/2) << 1$. Therefore, in strongly unstable environments, $F_H << F_V$. The

stratification is stable when $\psi>\pi/2$ ($\partial\theta/\partial z>0$). In the upper tropospheres and stratospheres of the planets, the atmosphere becomes optically thin at infrared wavelengths, and vertical radiative heat transfer at these wavelengths becomes instrumental in producing a fairly strong stable stratification. In addition, due to the rather great disparity between the vertical scale of the atmosphere, typically of the order of one scale height H, and the horizontal scale, which is comparable to the radius a of the planet, the vertical derivative of potential temperature dominates the horizontal derivative, $|\partial\theta/\partial y|/|\partial\theta/\partial z| \leq H/a << 1$. From (2.5c) it then follows that $\pi-\psi \leq H/a << 1$. For this limit, (2.5b) implies $|F_H/F_V| = \tan(\psi/2) >> 1$. Consequently, in a stable environment such as the upper troposphere and stratosphere of Uranus, the horizontal component of the dynamical heat flux is expected to be much greater than the vertical component. This is in fact what is observed for mid-latitude synoptic-scale systems in Earth's atmosphere (Palmen and Newton, 1969; p. 58).

According to the mixing length theory represented by Eqs. (2.5a)-(2.5c), the horizontal dynamical heat transfer in the visible atmosphere of Uranus will be significant only in the stably stratified portions of the atmosphere. To see why this is so, assume instead for the moment that the opposite is true - that the dynamical motions in unstable, convecting regions can fulfill the horizontal heat transport

requirements of the atmosphere. On the annual average, the power that must be transported horizontally on Uranus to make up for the differential solar heating amounts to approximately 10% of the emitted power (assuming a low value for the internal heat source). The maximum vertical component F_V of the convective heat flux in an unstable region cannot greatly exceed the infrared flux emitted to space. Hence, the power being transported vertically through the atmosphere is of order $\sim F_V a^2$, where a is the planetary radius. The horizontal power transported is of order $\sim aDF_H$, where D is the depth of the zone over which F_H is substantial; equating this to 10% of the emitted power implies $F_H D \sim 0.1 F_V a$. In an unstable region, $\psi < \pi/2$. From (2.5b), it follows that $|F_H/F_V| \leq 1$. Therefore, $D \geq 0.1a$, i.e., the depth of the convection zone must be at least 10% of the planetary radius, or ~2600 km, if horizontal heat transport in unstable regions is to be comparable to 10% of the emitted power. This depth is much greater than the ~200 km depth of the visible atmosphere. It can be concluded from this argument that if significant horizontal heat transport is occurring in the visible atmosphere, it must do so at levels where the stratification is stable. If significant horizontal heat transport occurs in convective regions, it must occur at depths greater than ~10% of the

planetary radius. Of course, these conclusions are subject to the validity of the flux parameterization in Eqs. (2.5a)-(2.5c).

Convection. In Ingersoll and Porco's mixing-length formulation, Eqs. (2.5a)-(2.5c) are meant to apply for $0 \leq \psi \leq \pi$. In the numerical calculations done here, the dynamical fluxes are explicitly evaluated only for $\pi/2 \leq \psi \leq \pi$, that is, only in stably stratified regions. If $\psi<\pi/2$, corresponding to unstable stratification, the dynamical heat fluxes are not evaluated. Instead, after each time step of the model, a convective adjustment is performed on any layers that have developed a superadiabatic temperature gradient as a result of heating or cooling during the just-completed time step. The adjustment consists of replacing the superadiabatic gradient with a dry adiabat in a manner that conserves the original enthalpy of the layer. In the actual computations, an iterative procedure is required to insure that no unstable layers develop as a result of the adjustment process itself. Typically, 20 iterations were found to be enough. This treatment of small-scale convection is very similar to the conventional treatment for thin-atmosphere planets (e.g., Manabe and Wetherald, 1967). There is one important difference, however, which originates from the fact that the calculations are being done for a planet with a deep atmosphere and fluid interior. This difference involves the special convective adjustment

performed on any unstable layers that are in direct contact with the convective interior. In the context of the model, such layers correspond to those whose lower boundary coincides with the lower boundary of the model. In the convective adjustment of these layers, no effort is made to conserve the enthalpy, because the resulting new adiabat of these layers cannot be made cooler than the interior adiabat (as it would have to be if enthalpy were conserved). Instead, it is assumed that these layers can freely extract from the deep atmosphere whatever heat is necessary to maintain them on the interior adiabat.

Internal Flux. The internal heat flux is calculated by considering the energy budget of an atmospheric column. In steady-state, the total power entering the column must equal the power leaving it. The difference between the thermal radiative plus horizontal power leaving the column and the solar plus horizontal power entering the column is the internal power. Once the internal power is known, the average internal flux incident at the bottom of the column is calculated.

3. Results of the Steady-State Model

Figure 2-2 shows the synthetic spectrum produced by the model when the temperature profile of Moseley et al. (1985) is used for the thermal structure. This temperature profile was obtained by Moseley et al. by direct inversion of their spectral data. The agreement between the model synthetic spectrum and theirs, using the same composition and temperature profile, is within 2% of the brightness temperature at wavenumbers where the two spectra can be directly compared. This comparison serves as a check on the radiative transfer calculation used for the model.

Runs of the radiative-convective-dynamical model were made for the two cases of solar heating shown in Figure 2-1. For each of these cases, the value of E, which is the ratio of total emitted power to absorbed solar power, was varied from a value near 1.0 to about 1.5. Plots showing the meridional dependence of the emitted thermal flux Em, absorbed solar flux A, and internal flux I for each run appear in Figures 2-3(a-e) and 2-4(a-e). In equilibrium, the combination (Em-A-I) gives the vertically integrated heating by the horizontal dynamical flux.

Figures 2-3 and 2-4 show that for low values of E the internal flux I is nearly uniform with respect to latitude. The dynamical heating (Em-A-I) balances the absorbed solar heating A in the sense that their sum is nearly uniform. In

Figure 2-2. Solid line - synthetic spectrum produced by the model using the thermal structure of Moseley et al. (1985). Dotted line -- synthetic spectrum produced by Moseley et al. The two synthetic spectra agree to within 2% of the brightness temperature between 100 cm^{-1} and 400 cm^{-1}. The data points represent the observations of several workers, and were taken directly from Orton et al. (1984), their Figure 2. The sources and internal errors of the data can be obtained from that figure.

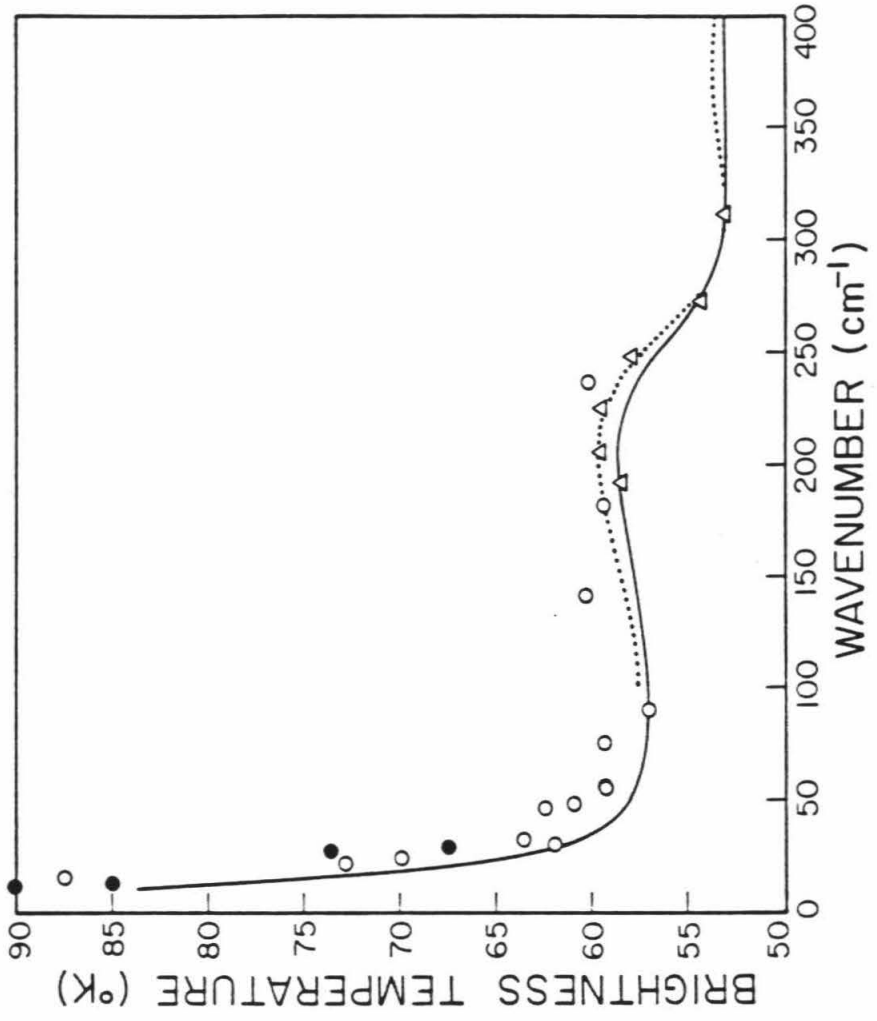
BRIGHTNESS TEMPERATURE (°K)
90
85
80
75
70
65
60
55
50
0
50
100
150
200
250
300
350
400
WAVENUMBER (cm⁻¹)

this case the equatorward heat transfer required by the distribution of absorbed sunlight takes place in the visible atmosphere. This is the terrestrial regime. As E increases the internal heat flux and the dynamical heating exchange roles. For high values of E, the dynamical heating (Em-A-I) is nearly zero. The internal flux I balances the absorbed solar flux A and is equal to the net (emitted minus absorbed) radiative flux at each latitude. In this case the equatorward heat transfer takes place in the interior. This is the jovian regime. For intermediate values of E the two regimes co-exist but at different latitudes. From the poles down to some critical latitude the behavior of the fluxes resembles that of the terrestrial regime. Equatorward of this latitude the behavior resembles the jovian regime. The terrestrial regime retreats to the poles as E increases and finally disappears altogether at large E. Coexistence of the two regimes indicates that both the visible atmosphere and interior participate in the meridional heat transport.

Figures 2-5a,b and 2-6a,b show contours of potential temperature between 20 bar and 670 mbar. As seen in the figures, the atmosphere is generally characterized by two regions with stable stratification. The upper stable region, at pressures less than 1 bar, is the usual radiative zone in which the atmosphere is optically thin to thermal infrared radiation. The lower stable region is more unusual. It occurs between 3 and 10 bars in the NC model

Figure 2-3a. The emitted infrared flux, absorbed solar flux, and internal heat flux vs. sine-latitude for the NC solar heating model. The case shown is for E=1.07. The absorbed solar flux is the same in Figures 2-3a through 2-3e, but the total emitted power increases with increasing E. The emitted power was varied by changing the (assumed constant) potential temperature of the planet's interior. The fluxes are plotted in units of 0.66 W/m^2, which corresponds to an effective temperature of 58.3 K. The dotted curve is the difference between the emitted infrared flux and the sum of the absorbed solar plus internal heat fluxes, and is equal to the convergence of the horizontal heat flux associated with baroclinic eddies.

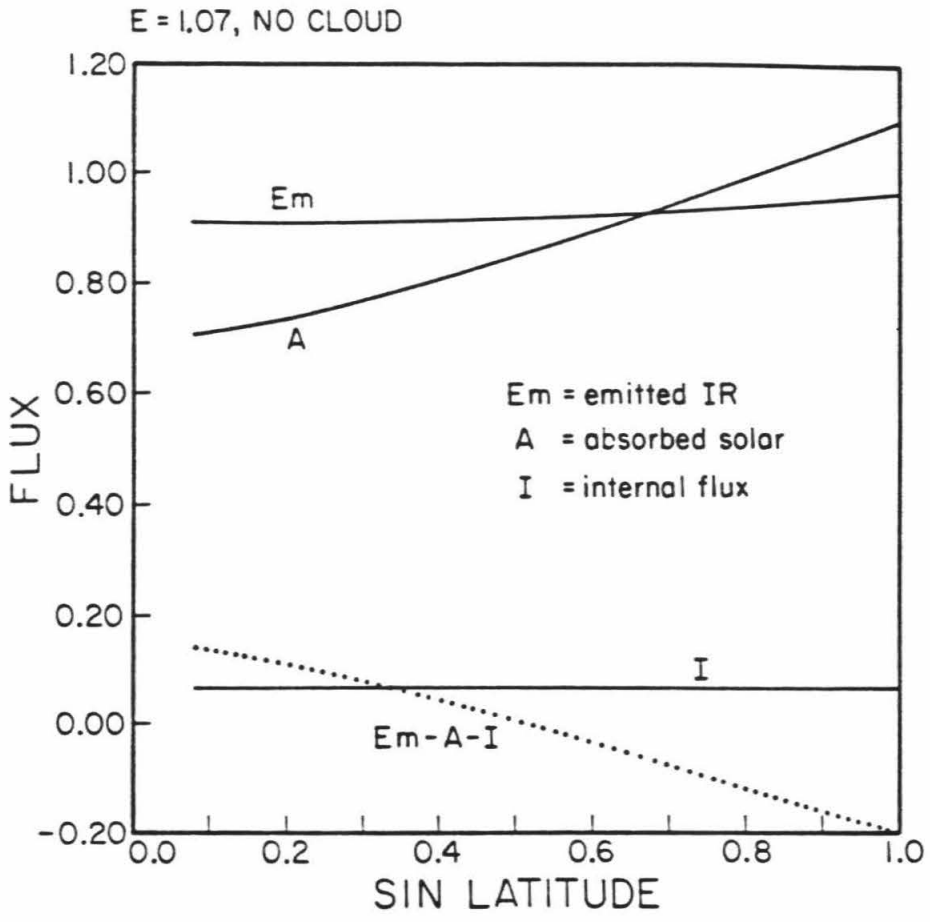
E = 1.07, NO CLOUD
1.20
1.00
0.80
0.60
0.40
0.20
0.00
-0.20
FLUX
Em
A
Em = emitted IR
A = absorbed solar
I = internal flux
I
Em-A-I
0.0
0.2
0.4
0.6
0.8
1.0
SIN LATITUDE

Figure 2-3b. The same as in Figure 2-3a but for E=1.14.

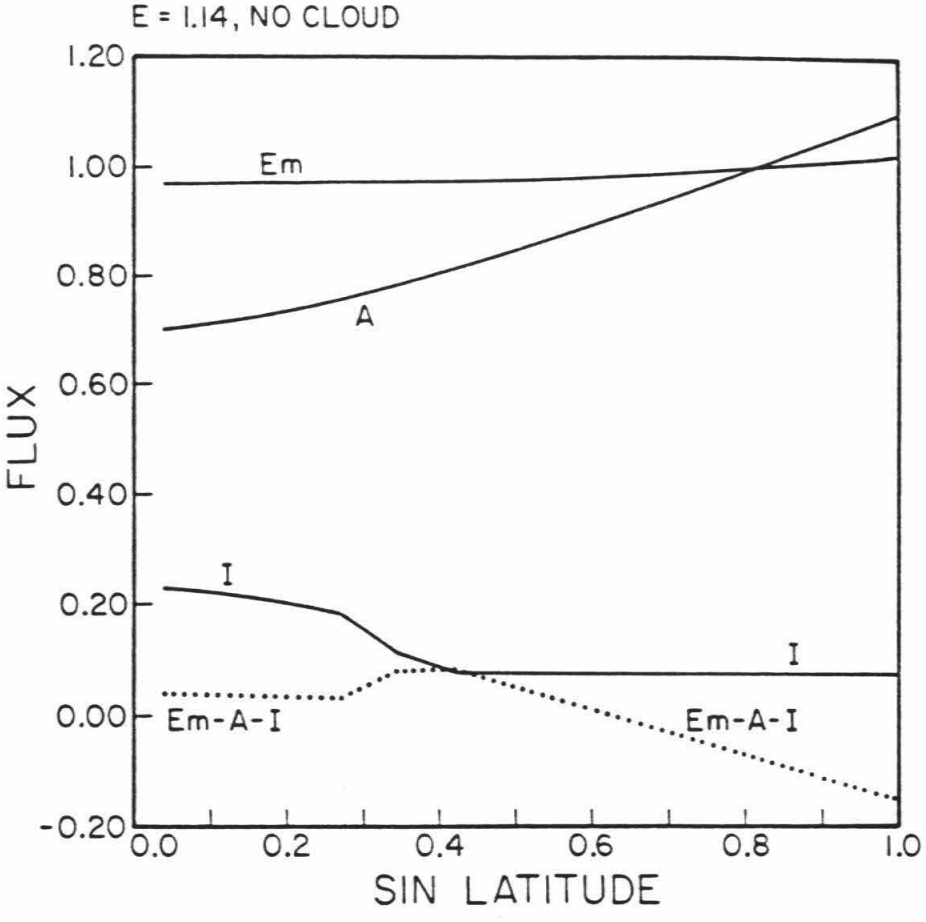
E = 1.14, NO CLOUD
1.20
1.00
0.80
0.60
0.40
0.20
0.00
-0.20
FLUX
Em
A
I
I
Em-A-I
Em-A-I
0.0
0.2
0.4
0.6
0.8
1.0
SIN LATITUDE

Figure 2-3c. The same as in Figure 2-3a but for E=1.22.

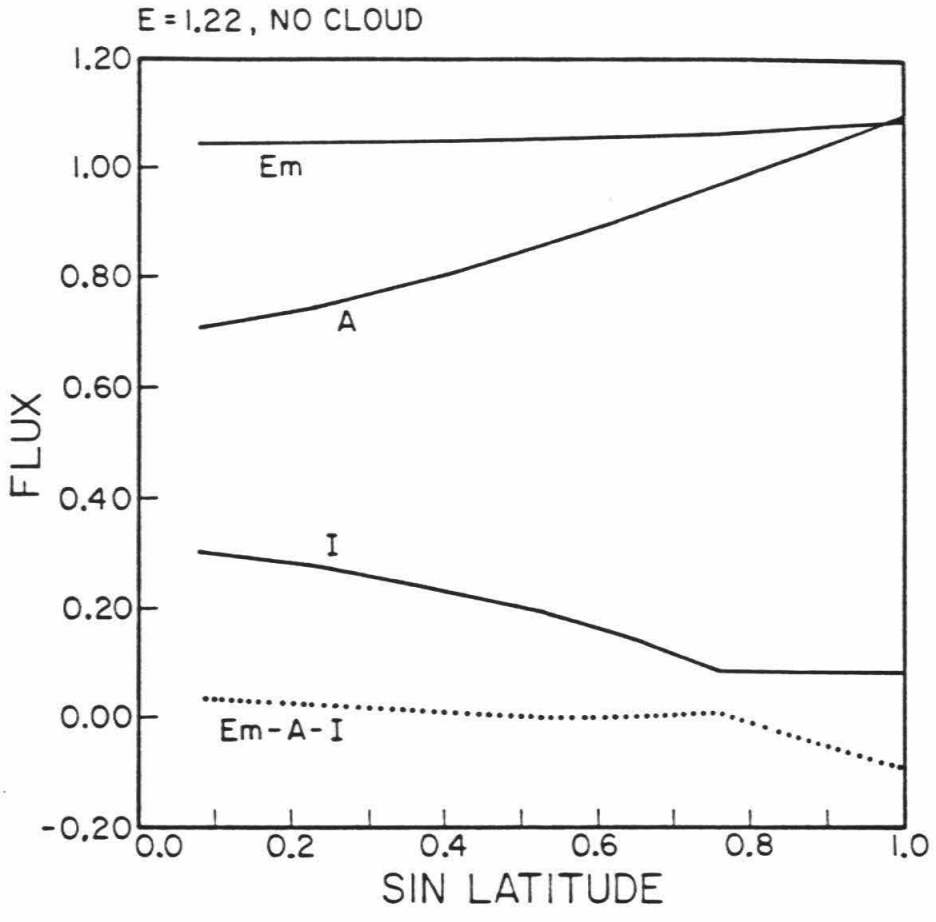
E = 1.22 , NO CLOUD
1.20
1.00
0.80
0.60
0.40
0.20
0.00
-0.20
FLUX
Em
A
I
Em-A-I
0.0
0.2
0.4
0.6
0.8
1.0
SIN LATITUDE

Figure 2-3d. The same as in Figure 2-3a but for E=1.35.

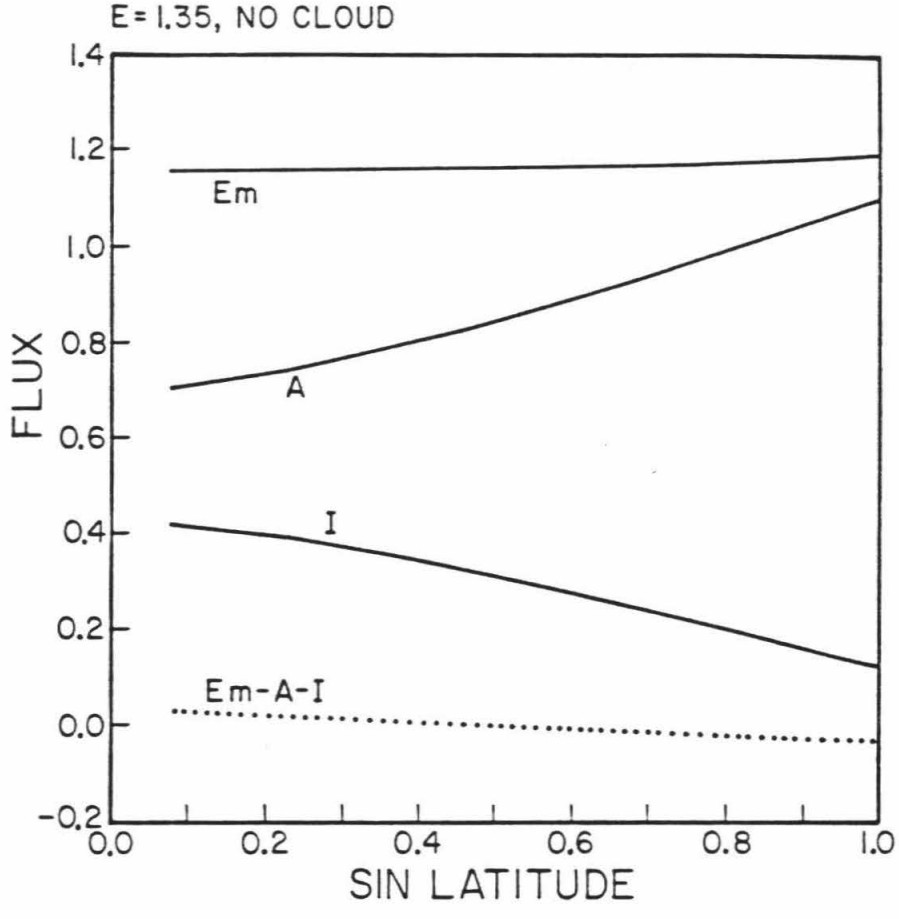
E = 1.35, NO CLOUD
1.4
1.2
1.0
0.8
0.6
0.4
0.2
0.0
-0.2
FLUX
Em
A
I
Em-A-I
0.0
0.2
0.4
0.6
0.8
1.0
SIN LATITUDE

Figure 2-3e. The same as in Figure 2-3a but for E=1.65.

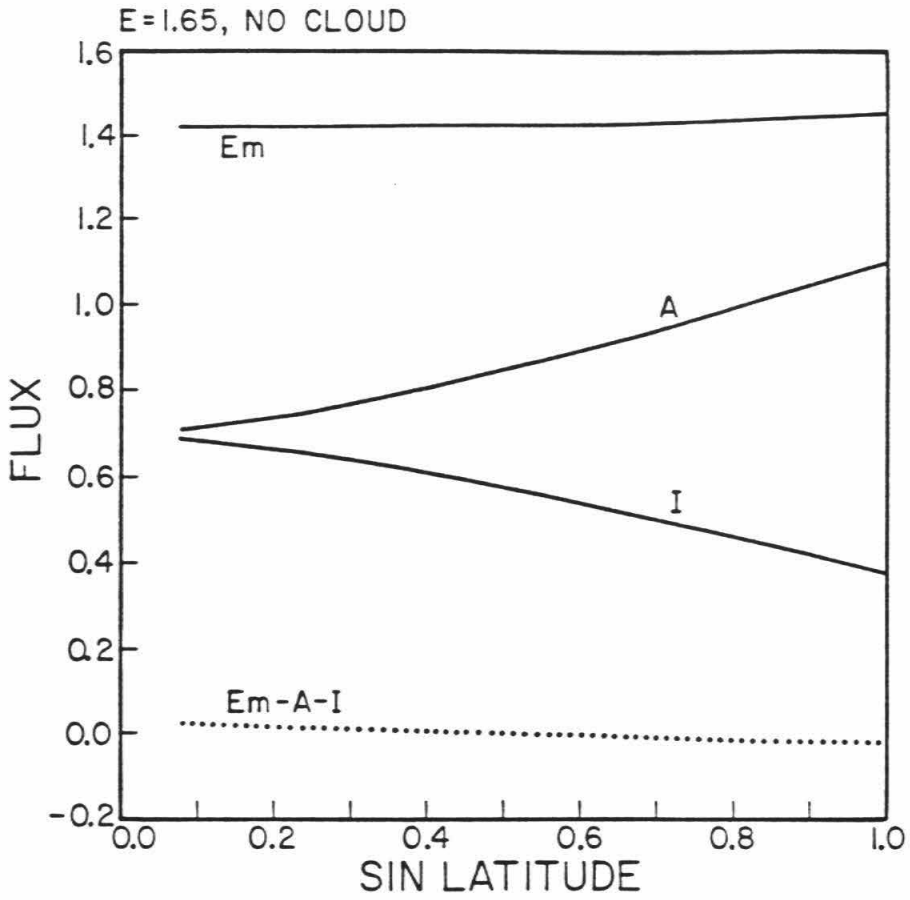
E=1.65, NO CLOUD
1.6
1.4
1.2
1.0
0.8
0.6
0.4
0.2
0.0
-0.2
FLUX
Em
A
I
Em-A-I
0.0
0.2
0.4
0.6
0.8
1.0
SIN LATITUDE

Figure 2-4a. The same as in Figure 2-3a but for the C solar heating model, and E=1.07.

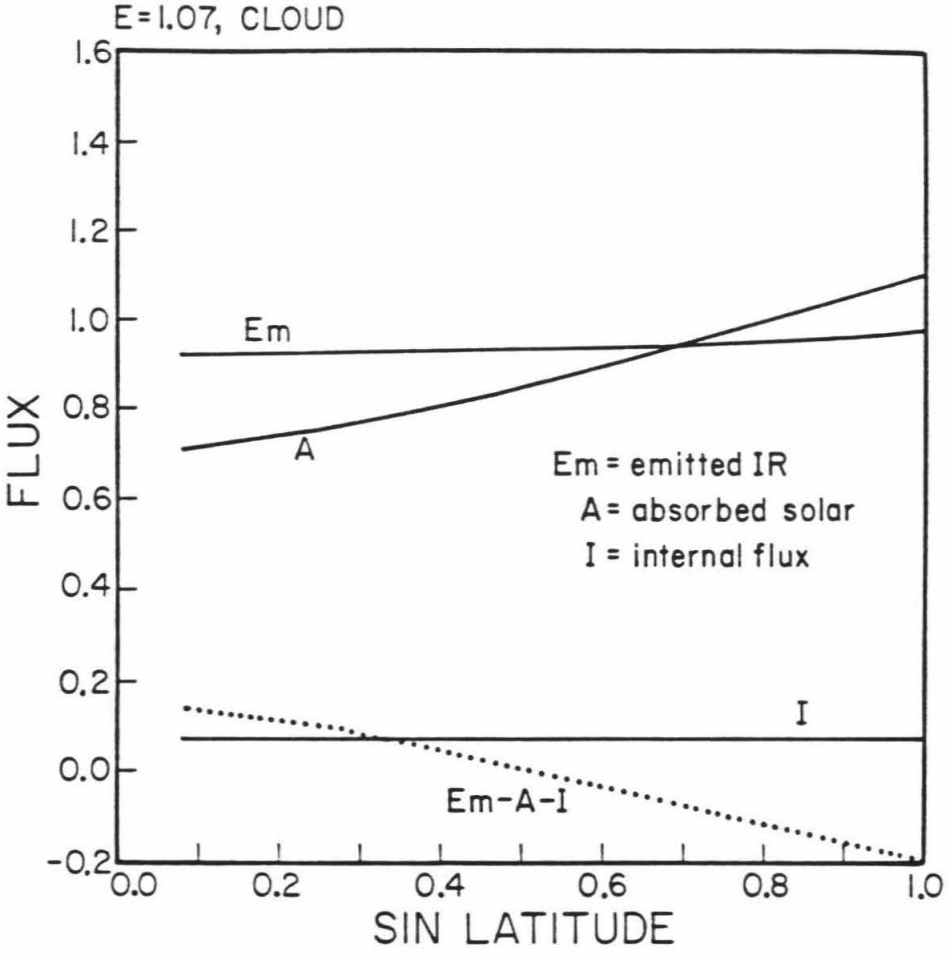
E=1.07, CLOUD
1.6
1.4
1.2
1.0
0.8
0.6
0.4
0.2
0.0
-0.2
FLUX
Em
A
Em = emitted IR
A = absorbed solar
I = internal flux
I
Em-A-I
0.0
0.2
0.4
0.6
0.8
1.0
SIN LATITUDE

Figure 2-4b. The same as in Figure 2-3a but for the C solar heating model, and E=1.16.

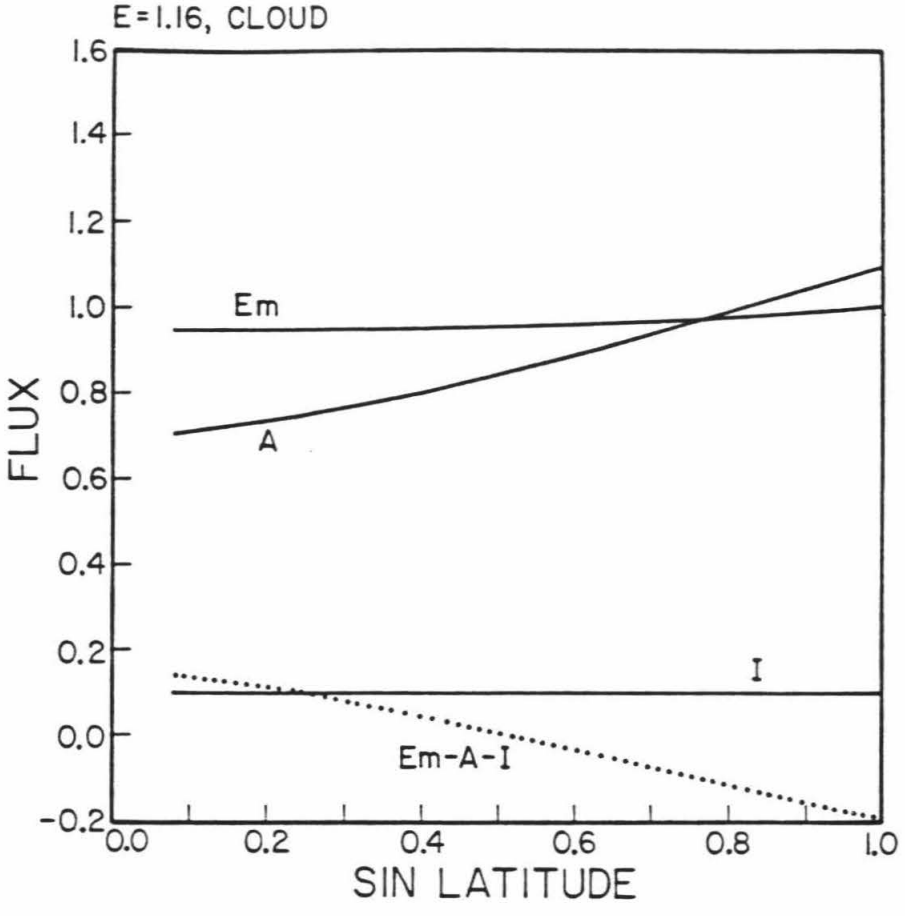
E=1.16, CLOUD
1.6
1.4
1.2
1.0
0.8
0.6
0.4
0.2
0.0
-0.2
FLUX
Em
A
I
Em-A-I
0.0
0.2
0.4
0.6
0.8
1.0
SIN LATITUDE

Figure 2-4c. The same as in Figure 2-3a but for the C solar heating model, and E=1.22.

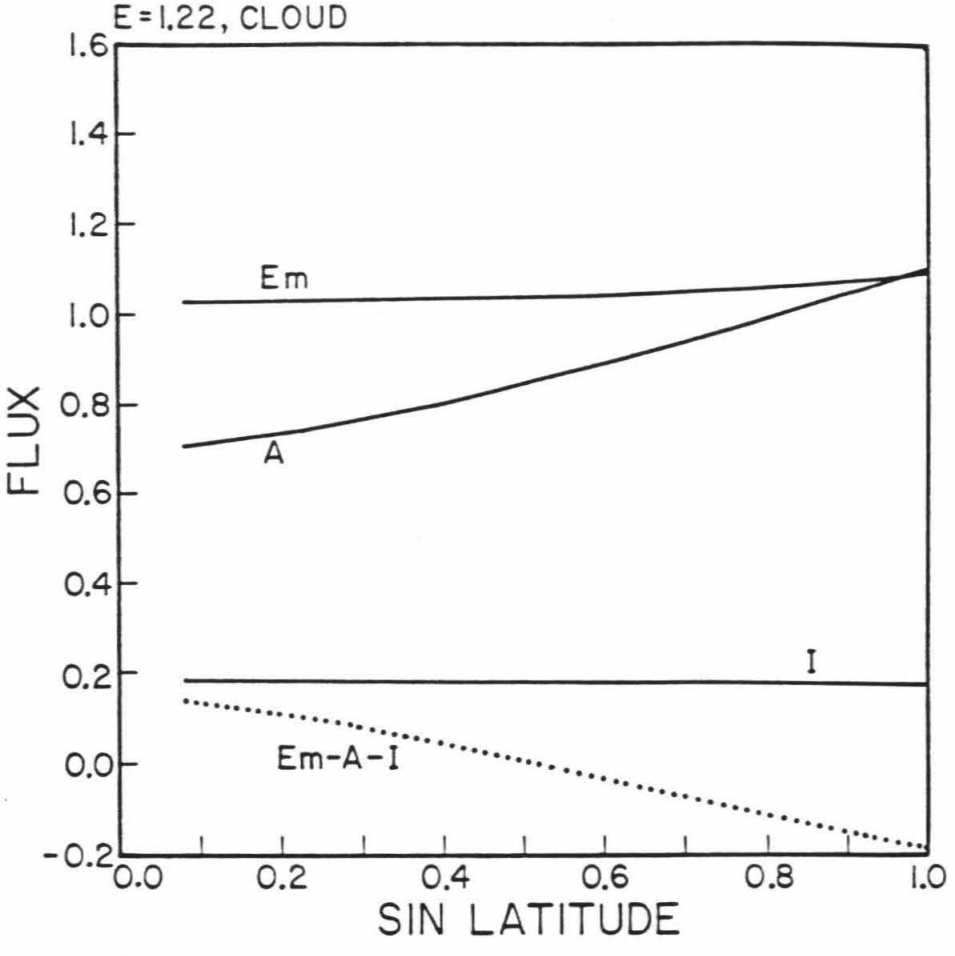
E=1.22, CLOUD
1.6
1.4
1.2
1.0
0.8
0.6
0.4
0.2
0.0
-0.2
FLUX
Em
A
I
Em-A-I
0.0
0.2
0.4
0.6
0.8
1.0
SIN LATITUDE

Figure 2-4d. The same as in Figure 2-3a but for the C solar heating model, and E=1.35.

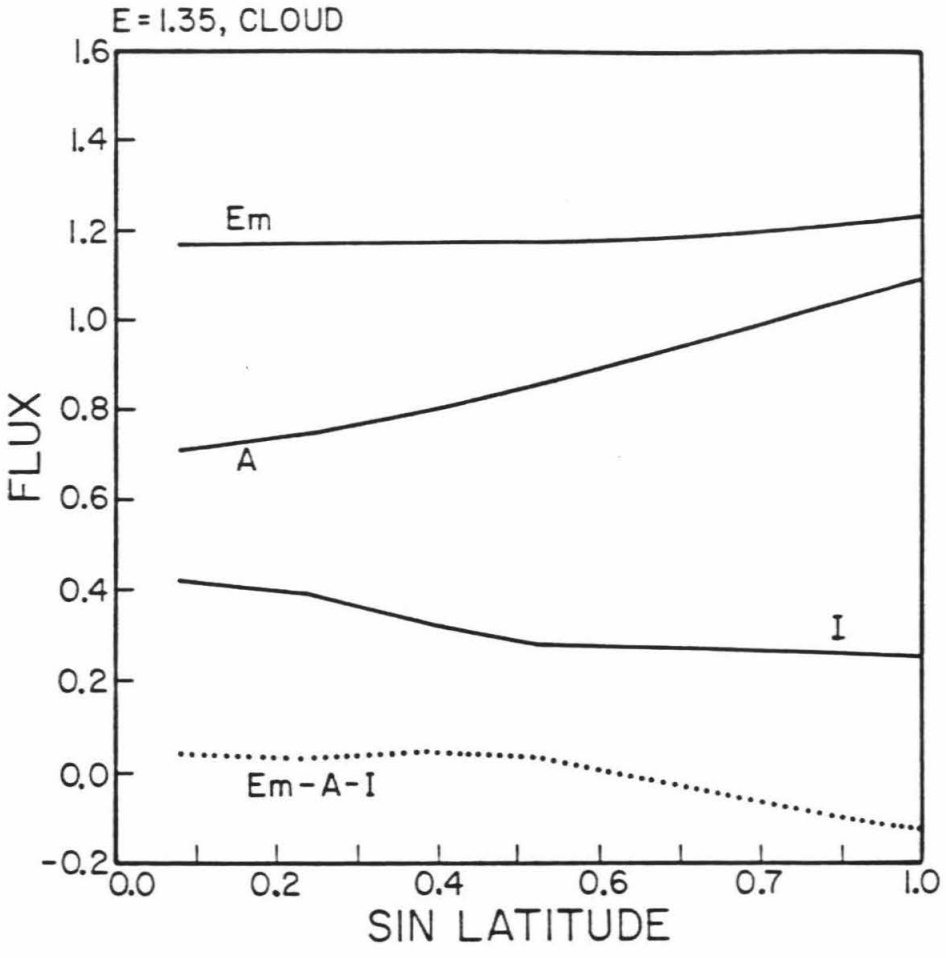
E = 1.35, CLOUD
1.6
1.4
1.2
1.0
0.8
0.6
0.4
0.2
0.0
-0.2
FLUX
Em
A
I
Em-A-I
0.0
0.2
0.4
0.6
0.7
1.0
SIN LATITUDE

Figure 2-4e. The same as in Figure 2-3a but for the C solar heating model, and E=1.62.

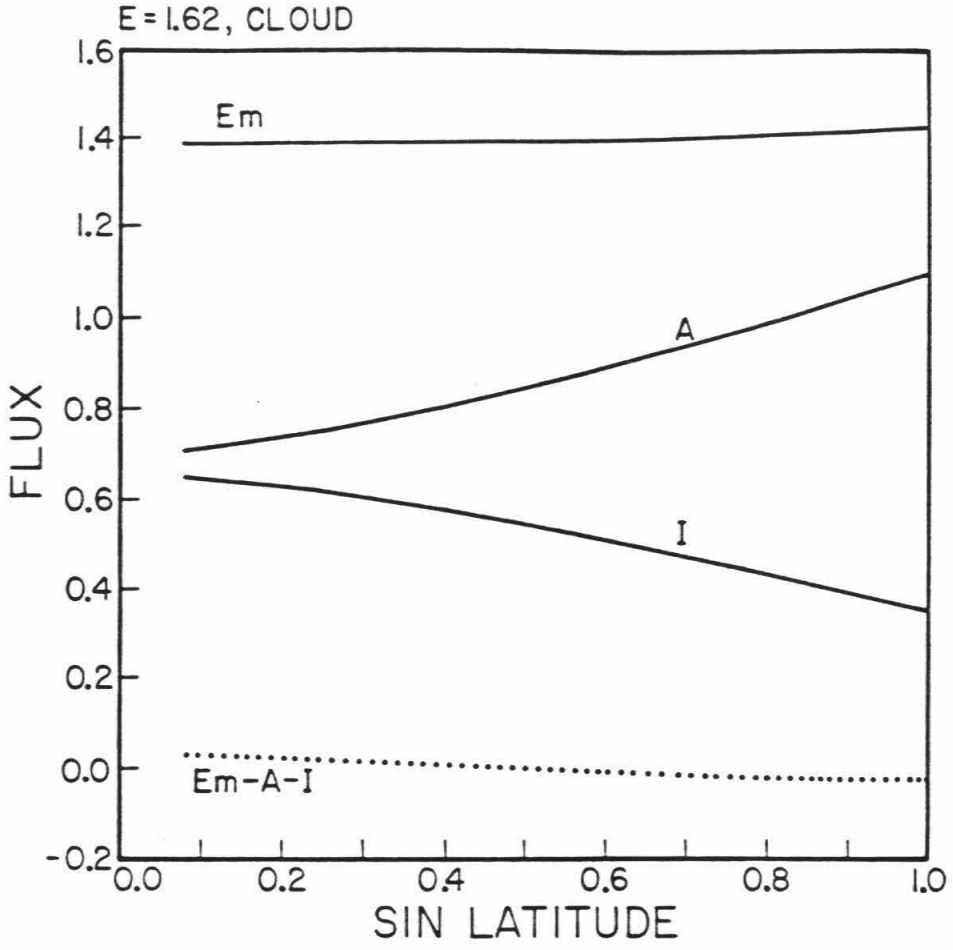
E = 1.62, CLOUD
1.6
1.4
1.2
1.0
0.8
0.6
0.4
0.2
0.0
-0.2
FLUX
Em
A
I
Em-A-I
0.0
0.2
0.4
0.6
0.8
1.0
SIN LATITUDE

Figure 2-5. Potential temperature contours for the NC solar heating model. Contours are labeled in units of the interior potential temperature, θ_0, where θ_0 is measured from a reference pressure of 20 bars. At a pressure of 1 bar, a temperature difference of 1.0 K corresponds to a difference between contours of $2.17/\theta_0$. For example, in Figure 2-5a, a temperature difference of 1 K at 1 bar corresponds to a difference between contours of 0.0136. (a) E = 1.07, θ_0 = 198.4 K. (b) E = 1.22, θ_0 = 207.9 K.

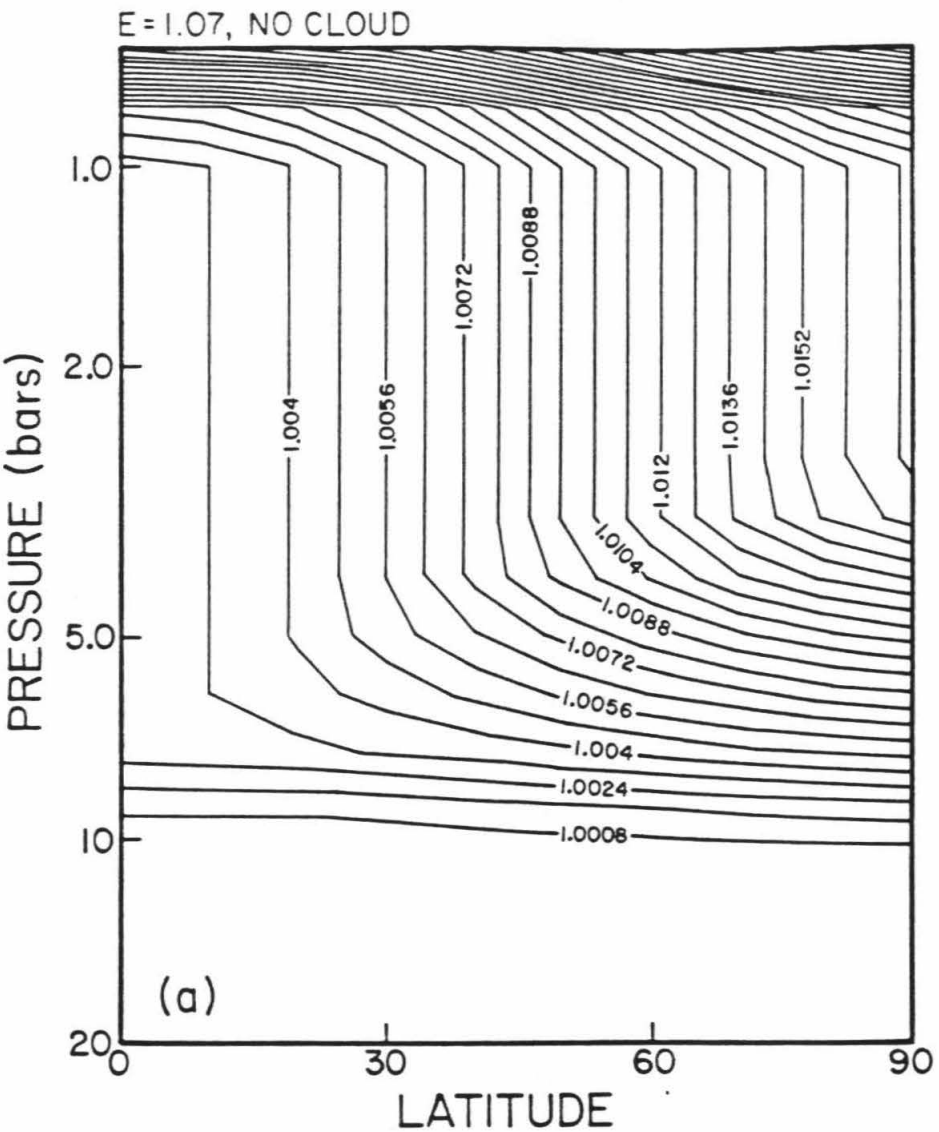
E = 1.07, NO CLOUD
PRESSURE (bars)
1.0
2.0
5.0
10
20
0
30
60
90
LATITUDE
(a)
1.004
1.0056
1.0072
1.0088
1.012
1.0136
1.0152
1.0104
1.0088
1.0072
1.0056
1.004
1.0024
1.0008

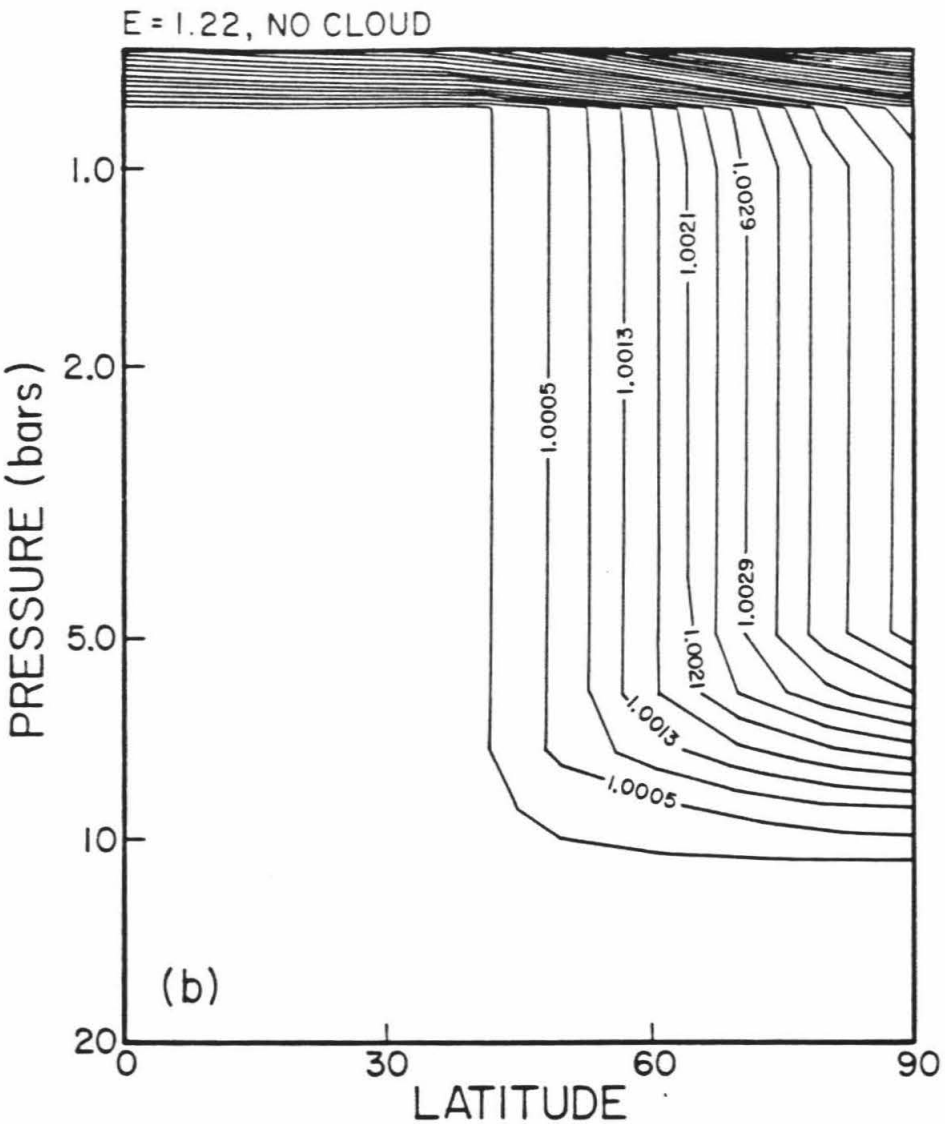
E = 1.22, NO CLOUD
1.0
2.0
5.0
10
20
PRESSURE (bars)
1.0005
1.0013
1.0021
1.0029
1.0029
1.0021
1.0013
1.0005
(b)
0
30
60
90
LATITUDE

Figure 2-6. The same as in Figure 2-5 but for the C solar heating model. (a) E = 1.22, θ_0 = 198.4 K. (b) E = 1.40, θ_0 = 215.0 K.

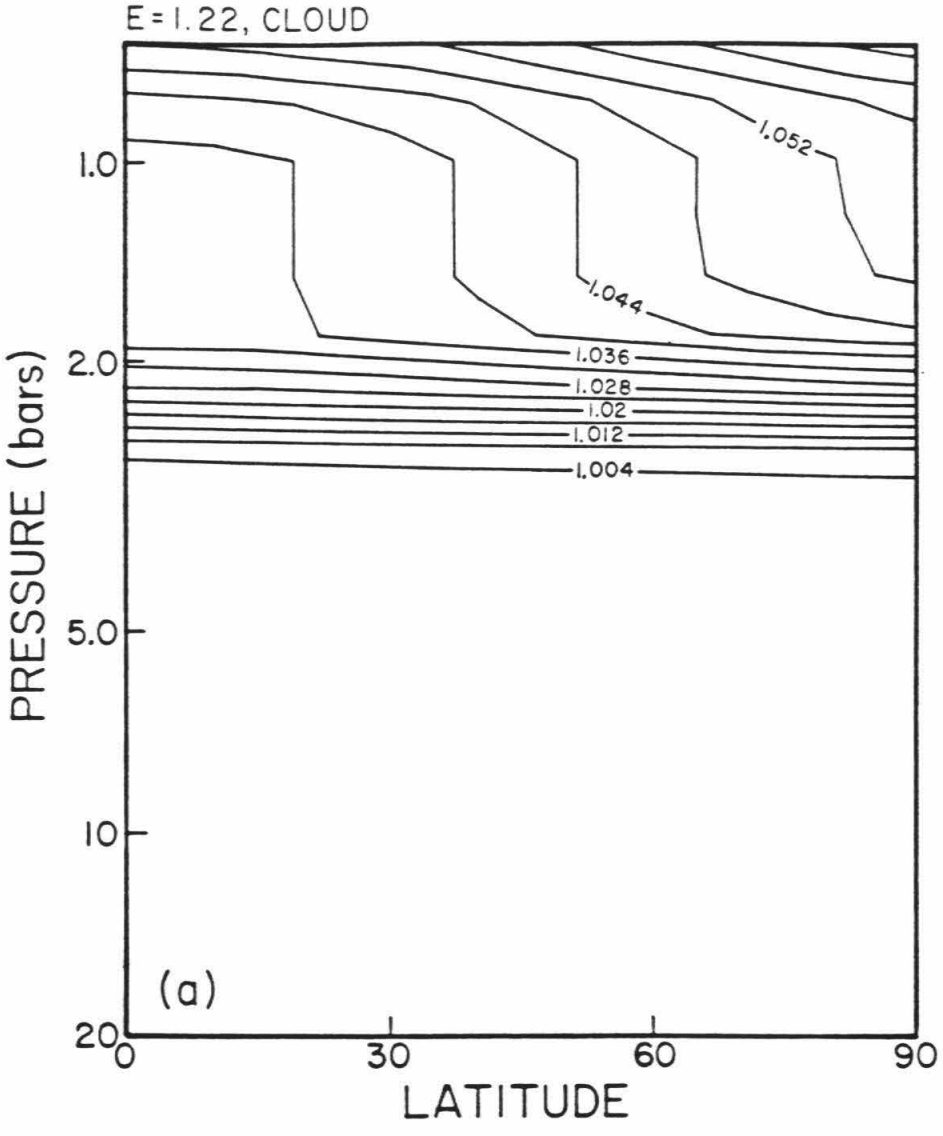
E = 1.22, CLOUD
1.052
1.044
1.036
1.028
1.02
1.012
1.004
1.0
2.0
5.0
10
20
PRESSURE (bars)
(a)
0
30
60
90
LATITUDE

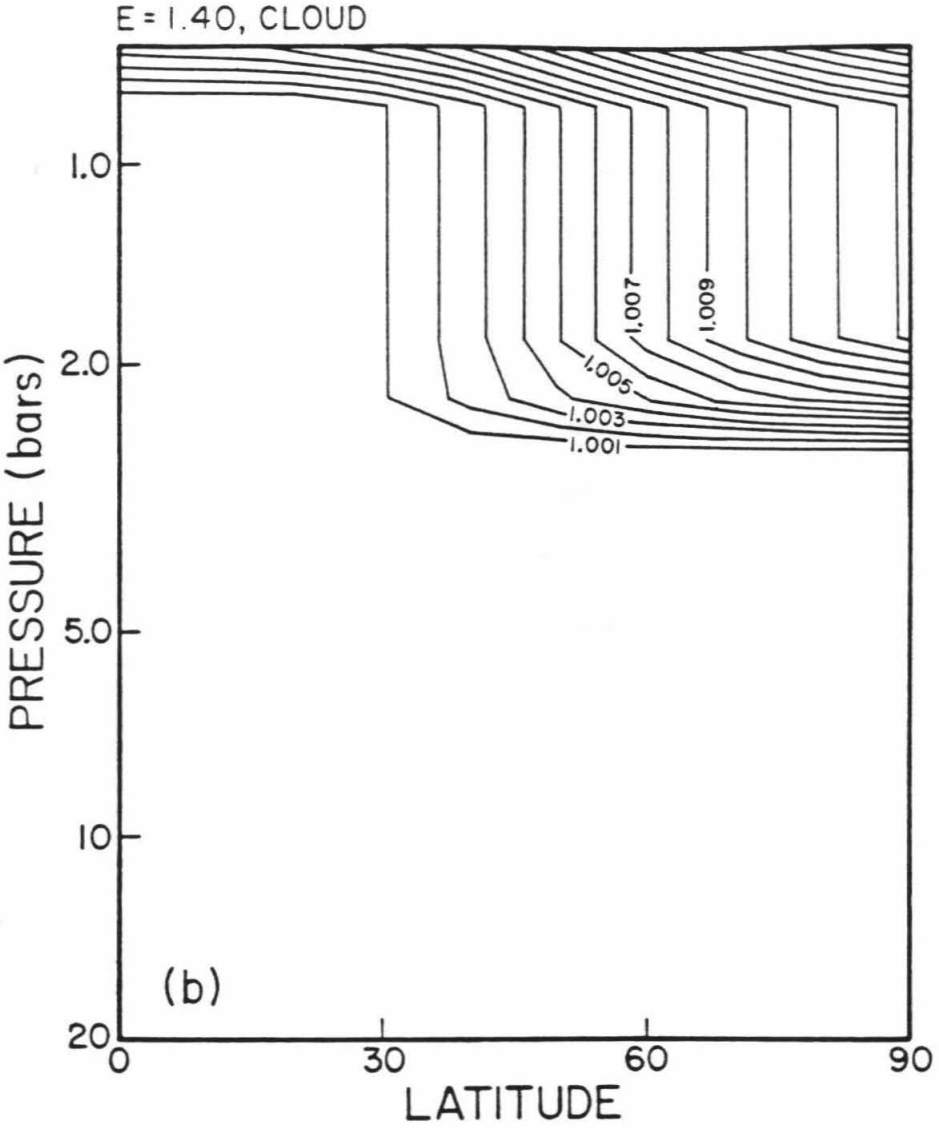
E = 1.40, CLOUD
1.0
2.0
5.0
10
20
PRESSURE (bars)
1.007
1.009
1.005
1.003
1.001
(b)
0
30
60
90
LATITUDE

and between 1.5 and 3 bars in the C model, just below the altitude of maximum solar heating (Fig. 2-1). It is found only in the terrestrial regime, poleward of the critical latitude (Figs. 2-3 and 2-4). For small E the deep stable layer occurs at all latitudes. As E increases, it retreats poleward and disappears when the critical latitude reaches the pole.

Consider now how the solutions change as the altitude of the solar heating increases. Comparison of Figures 2-5b and 2-6a reveals that the deep stable layer is more extensive (extends down to lower latitudes) when the solar heating is shallow (C model) than when the solar heating is deep (NC model). This fact is also seen in Figures 2-3 and 2-4, which show that for the same E, the critical latitude is lower for the C model than for the NC model. Equivalently, the value of E above which the deep stable layer no longer exists is higher for the C model than for the NC model. For model NC (Fig. 2-3), the complete transition to the jovian regime (variations in solar heating balanced by the internal heat flux at all latitudes) occurs at a value of E close to the critical value, which is 1.27 for Uranus. For the C model (Fig. 2-4), however, the complete transition occurs at a value of E close to 1.4 or 1.5.

The behavior of the internal heat flux can be related to the thermal structure of the terrestrial and jovian regimes with the aid of the discussion following Eqs. (2.5a)-(2.5c)

in the preceding section. There it was shown that the horizontal power transport in convective regions is substantial only at great depths. Certainly, above the 20 bar level, horizontal heat transfer in convective regions is negligible. In steady-state, the divergence of the total heat flux, $\nabla \cdot \mathbf{F}$, equals zero. This, together with the fact that the horizontal heat transport can be ignored in convective regions above 20 bar, implies

$$F_{IR}(p,\lambda) - S(p,\lambda) + F_C(p,\lambda) \approx I(\lambda) \qquad (2.6)$$

in the convective regions. Here, F_{IR} is the thermal infrared flux, S is the solar flux (defined positive in the downward direction), F_C is the vertical convective heat flux, and I is the internal flux. The infrared flux F_{IR} is nearly independent of latitude, since horizontal temperature contrasts on Uranus are quite small. It is a monotonically increasing function of altitude, however, that varies from ~60 erg cm^{-2} s^{-1} at the 10 bar level to ~650 erg cm^{-2} s^{-1} at the 500 mbar level (these numbers apply to the E = 1.22 "NC" case depicted in Figs. 2-3c and 2-5b).

Now refer to Fig. 2-5b. The terrestrial regime occurs poleward of ~40°. In the convective region below the deep stable layer in this regime, i.e., below ~10 bar, Eq. (2.6) implies $F_{IR}(p) + F_C(p,\lambda) \approx I(\lambda)$ since S is negligible at

these depths. At the base of the deep stable layer, $F_C(p_s) = 0$, where $p_s \approx 10$ bar is the pressure at the base of the stable layer. Therefore, $I(\lambda) \approx F_{IR}(p_s) \approx 60$ erg cm^{-2} s^{-1} in the terrestrial regime. As can be seen in Fig. 2-5b, p_s is nearly independent of latitude in the terrestrial regime, and so it follows that $I(\lambda)$ is also nearly independent of latitude in this regime. In the jovian regime, equatorward of 40°, there is no deep stable layer. The atmosphere is convective all the way up to the 800 mbar level. However, $F_C(p_s) = 0$, where p_s is now the pressure at the radiative-convective boundary at ~800 mbar in this regime. By Eq. (2.6), it follows that $I(\lambda) \approx F_{IR}(p_s) - S(p_s,\lambda) \approx 200$ erg cm^{-2} s^{-1} at the equator. Once again, it is evident from Fig. 2-5b that p_s in the jovian regime is very nearly independent of latitude. Since both p_s and F_{IR} are nearly independent of latitude, it is clear that the variation of the internal flux I with latitude in the jovian regime must compensate for the variation of the sunlight S with latitude, in the sense that their sum, which is $F_{IR}(p_s,\lambda)$, is nearly constant in latitude. The relationship between the internal flux and the thermal structure of each regime is seen to hold for both solar heating models and over a wide range of E.

In both solar heating models the equator-to-pole difference in effective temperature is 1 K for low E and decreases to 0.5 K for $E \approx 1.5$. The observed equator-to-

pole difference is likely to be larger than this due to the seasonal variation.

The typical velocity and length scale of the baroclinic eddies can be estimated using formulas presented by Stone (Stone, 1972, Eq. 2.7:, Stone, 1973, Table I). Since most of the dynamical heat transport occurs in the lowest scale height of the upper stable region, the thermal structure of these levels will be used to characterize the eddies. The typical velocity of the eddies is assumed to be of the same order as the zonal thermal wind difference across one scale height. Taking the equator-to-pole temperature difference to be 1 K, the typical eddy velocity is found to be ~1 m/s. From Fig. 2-5a, it may be deduced that $\partial\theta/\partial z \approx 2.7\times10^{-6}$ K cm^{-1} at ~800 mbar. This translates into a Brunt-Vaisala frequency N (Holton, 1979; p. 50) of 3.4×10^{-3} s^{-1}. For comparison, N for the Earth's troposhere is ~10^{-2} s^{-1}. The horizontal scale of the eddies is ~NH/f. Using the above value for N and 30 km for H gives a scale length of 930 km.

4. Conclusions

It has been found that the extra annual average sunlight at the Uranian poles produces a subadiabatic layer in the deep atmosphere that extends down from the poles to some critical latitude. The position of this latitude depends on the magnitude of the internal heat source. For a small internal heat source, the critical latitude is at or near the equator. As the internal heat source is increased, the critical latitude moves poleward until, for a sufficiently large internal heat source, the deep subadiabatic layer disappears entirely.

The presence or absence of the deep subadiabatic layer determines whether that part of the planet is in the terrestrial regime or the jovian regime. In the former case the internal flux is uniform with respect to latitude, and the horizontal dynamical heating balances the latitudinal variation in absorbed solar flux. In the latter case the horizontal dynamical heating is near zero, and the internal flux is equal to the net (emitted minus absorbed) radiative flux at each latitude.

The present results shed new light on the conditions that must be met before the entire planet is in the jovian regime. Ingersoll and Porco (1978) assumed that a sufficient condition is that E be greater than the critical value, which for Uranus is 1.27. The latter is computed

simply by requiring that the emitted flux (assumed constant with respect to latitude) be greater than the absorbed solar flux at each latitude. The NC model, in which the sunlight is deposited well below the infrared radiative zone, seems to enter the jovian regime as E increases past the critical value. However, the C model, in which sunlight is deposited close to the radiative zone, does not enter the jovian regime until E is 1.4 or 1.5. Apparently, deposition of sunlight at relatively high altitudes favors the terrestrial regime, even when the value of E is moderately supercritical.

Although the present results are for Uranus only, the radiative-convective-dynamical model should be applicable to Jupiter, Saturn, and Neptune as well. These planets are all known to have relatively large internal heat sources. Consequently, according to the results of the preceding section, it might be anticipated that their meridional energy balance will be dominated by the jovian regime. The altitude dependence of the solar heating could at least partially alter this conclusion, however, and therefore runs of the radiative-convective-dynamical model should be made for these planets as well.

In this chapter, a steady-state model for the meridional energy balance of Uranus' atmosphere has been presented. It is natural to ask whether the steady-state calculation should be considered at all relevant to the actual situation

for Uranus. Due to its large obliquity, Uranus experiences the largest percentage seasonal variation of its insolation of any planet in the solar system. Might this seasonal variation in insolation force the meridional energy balance to vary seasonally as well? In fact, an estimate of the cooling time scale of the deep stable layer argues that the meridional energy balance should vary seasonally. During the long winter nights on Uranus, the deep stable layer must undergo some degree of cooling. If the amount of cooling is sufficiently great, the deep stable layer could disappear entirely. The results of the previous section show that if this were to happen at some latitude, the meridional energy balance there would make a transition from terrestrial to jovian behavior. Hence, the steady-state model can be relevant only if the cooling time scale of the deep stable layer is much longer than a Uranian year. Associated with the stable stratification of this layer is an enthalpy/unit area, which is slightly in excess of what the enthalpy/unit area would be if temperatures in the layer were on the deep adiabat. This enthalpy excess corresponds to the amount that must be removed by cooling before the deep stable layer will disappear. It is given approximately by

$$\delta H \sim \frac{p}{(\kappa+1)g} C_p \left(\frac{p}{p_0}\right)^{\kappa} \delta\theta \qquad (2.7)$$

where δH is the enthalpy excess, p is the pressure at the base of the stable layer, and $\delta\theta = \theta - \theta_0$ is the mean potential temperature in excess over the potential temperature of the interior θ_0. The cooling time scale is given by the excess enthalpy divided by the difference of the fluxes entering the base and leaving the top of the stable layer. This difference is of the same order as the emission to space F_1 during the winter night, where $F_1 \approx 650$ erg cm^{-2} s^{-1}. Taking p to be ~10 bar, and $\delta\theta$ to be ~1.2 K (as implied by Fig. 2-5a), the cooling time scale τ is found to be

$$\tau \sim \frac{p}{(\kappa+1)g} C_p \left(\frac{p}{p_0}\right)^{\kappa} \frac{\delta\theta}{F_1} \sim 45 \text{ years} \qquad (2.8)$$

Hence, τ is only ~1/2 a Uranian year (the orbital period of Uranus is 84 years), implying that a seasonal description of the meridional energy balance would be more appropriate. A seasonal model for the meridional energy balance is the subject of the next chapter.

References

BERGSTRALH, J.T., AND K.H. BAINES (1984). Properties of the upper tropospheres of Uranus and Neptune derived from observations at ''visible'' to near-infrared wavelengths. In Uranus and Neptune (J.T. Bergstralh, Ed.), pp. 179-212. NASA Conference Publication 2330.

CHANDRASEKHAR, S. (1960). Radiative Transfer. Dover, New York.

COHEN, E.R., L. FROMMHOLD, AND G. BIRNBAUM (1982). Analysis of the far infrared H_2-He spectrum. J. Chem. Phys. **77**, 4933-4941.

CONRATH, B., AND P.J. GIERASCH (1984). Global variation of the para hydrogen fraction in Jupiter's atmosphere and implications for dynamics on the outer planets. Icarus **57**, 184-204.

DORE, P., L. NENCINI, AND G. BIRNBAUM (1983). Far infrared absorption in normal H_2 from 77 to 298 K. J. Quant. Spectrosc. Radiat. Transfer **30**, 245-253.

HANEL, R., B. CONRATH, M. FLASAR, V. KUNDE, P. LOWMAN, W. MAGUIRE, J. PEARL, J. PIRRAGLIA, R. SAMUELSON, D. GAUTIER, P. GIERASCH, S. KUMAR, AND C. PONNAMPERUMA (1979). Infrared observations of the Jovian system from Voyager 1. Science **204**, 972-976.

HANEL, R., B. CONRATH, M. FLASAR, V. KUNDE, W. MAGUIRE, J. PEARL, J. PIRRAGLIA, R. SAMUELSON, L. HERATH, M. ALLISON, D. CRUIKSHANK, D. GAUTIER, P. GIERASCH, L. HORN, R. KOPPANY, AND C. PONNAMPERUMA (1981). Infrared observations of the Saturnian system from Voyager 1. Science **212**, 192-200.

HOLTON, J. R. (1979). An Introduction to Dynamic Meteorology. Academic Press, New York.

INGERSOLL, A.P., AND C.C. PORCO (1978). Solar heating and internal heat on Jupiter. Icarus **35**, 27-43.

LANDAU, L. D., AND E. M. LIFSHITZ (1959). Fluid Mechanics. Pergamon Press, Oxford.

MANABE, S., AND R.T. WETHERALD (1967). Thermal equilibrium of the atmosphere with a given distribution of relative humidity. J. Atmos. Sci. **24**, 241-259.

MOSELEY, H., B. CONRATH, AND R.F. SILVERBERG (1985). Atmospheric temperature profiles of Uranus and Neptune. Astrophys. J. **292**, L83-L86.

PALMEN, E. AND C. W. NEWTON (1969). Atmospheric Circulation Systems. Academic Press, New York.

STONE, P.H. (1972). A simplified radiative-dynamical model for the static stability of rotating atmospheres. J. Atmos. Sci. **29**, 405-418.

STONE, P.H. (1973). The dynamics of the atmospheres of the major planets. Space Sci. Rev. **14**, 444-459.

WALLACE, L. (1980). The structure of the Uranus atmosphere. Icarus **43**, 231- 259.

WALLACE, L. (1983). The seasonal variation of the thermal structure of the atmosphere of Uranus. Icarus **54**, 110-132.

Chapter 3

SEASONAL MERIDIONAL ENERGY BALANCE AND THERMAL STRUCTURE OF THE ATMOSPHERE OF URANUS: A RADIATIVE-CONVECTIVE-DYNAMICAL MODEL

by

James Friedson and Andrew P. Ingersoll

Division of Geological and Planetary Sciences
California Institute of Technology
Pasadena, California 91125

Submitted to Icarus
June, 1986

Contribution number 4257 of the Division of Geological and Planetary Sciences, California Institute of Technology, Pasadena, California 91125.

Abstract

The seasonal meridional energy balance and thermal structure of the atmosphere of Uranus is investigated using a two-dimensional radiative-convective-dynamical model. Diurnal-average temperatures and heat fluxes are calculated as a function of pressure, latitude, and season. In addition to treating radiation and small-scale convection in a manner typical of conventional radiative-convective models, the dynamical heat fluxes due to large-scale baroclinic eddies are included and parameterized using a mixing length formulation (Stone, 1972; Ingersoll and Porco, 1978). The atmosphere is assumed to be bounded below by an adiabatic, fluid interior with a single value of potential temperature at all latitudes. The internal heat flux is found to vary with latitude and season. The total internal power and the global enthalpy storage rate are seen to oscillate in phase with a period of 1/2 Uranian year. On an annual-average basis, equatorward heat transport can take place in both the atmosphere and convective interior. For a weak internal heat source, the meridional transport takes place predominantly in the atmosphere. If the internal heat source is larger, a greater share of the transport is taken up by the interior. For a value of the internal heat near the current upper limit for Uranus (~27% of the absorbed sunlight), about 1/3 of the equatorward heat transport at

mid-latitudes occurs in the interior. For a given internal heat source, placing the peak of the solar heating at high altitudes or depositing the solar energy into a narrow altitude range favors heat transport by the atmosphere over the interior. Deep penetration of sunlight favors transport by the interior. For the time corresponding to the Voyager 2 Uranus encounter, the effective temperature at the south (sunlit) pole is calculated to be ~1.5 K higher than that at the equator. Horizontal contrasts of the mean 450-900 mbar temperature are found to be $\lesssim$1.5 K, in fair agreement with Voyager 2 IRIS results (Hanel et al., 1986), but the model fails to reproduce the local minimum in this temperature seen at -30°S. Nevertheless, it is concluded that meridional heat transport in the atmosphere is efficient in keeping seasonal horizontal temperature contrasts below those predicted by radiative-convective models (Wallace, 1983).

1. Introduction

In this paper we investigate the seasonal meridional energy balance and thermal structure of the atmosphere of Uranus. We are interested not only in specific questions related to Uranus, but also in the more general problem of how the flow of internal heat on a planet with such a large obliquity and low internal heat source differs from the flow on Jupiter and Saturn. Thus, we have included in the study cases in which the internal heat source clearly exceeds the current upper limit for Uranus (Pollack et. al., 1986), in an attempt to better understand the interaction of the internal heat with the solar-heated atmosphere of jovian planets.

The idea that the internal heat and fluid interior of a Jovian planet could participate in the meridional heat transfer was first suggested by Ingersoll (1976), and was later treated in more detail by Ingersoll and Porco (1978). In the latter paper, it was shown for Jupiter that the internal heat can balance the absorbed sunlight at each latitude, provided E, the ratio of total emitted power to absorbed sunlight, exceeds a critical value of 1.27. This proviso arises from the requirement in their model that the net (emitted infrared minus absorbed solar) irradiance be positive at all latitudes. Poleward heat transfer can then

take place in the interior at all latitudes instead of in the atmosphere.

Current estimates (Pollack et al., 1986; Hanel et al., 1986) of the bond albedo and effective temperature of Uranus put the upper limit of E at 1.27. The critical value of E for Uranus is, coincidentally, also equal to 1.27. Therefore, should its internal heat source be sufficiently weak, Uranus may be subcritical with respect to the annual-average insolation. If so, then the net irradiance leaving the atmosphere must be negative in the polar regions. It is clear that where the net irradiance is negative, the visible atmosphere must be responsible for at least part of the meridional heat transport. It has been hypothesized (Ingersoll, 1984) that, if Uranus is subcritical, it may be divided into two distinct regions. In the polar regions, where the net irradiance is negative, the visible atmosphere would transport the heat. At those latitudes where the net irradiance becomes positive, the internal heat might balance the absorbed sunlight, with the heat transfer taken up by the interior. This hypothesis, however, makes no attempt to consider seasonal variations. The idea that the convective heat flux from the interior could vary seasonally has been proposed by Danielson et al. (1977) and by Briggs and Andrew (1980) and was later discussed by Wallace (1983). The issue of seasonal variations of the

internal flux is of central importance to this investigation.

The radiative-convective-dynamical model computes diurnally averaged temperatures and radiative and dynamical heat fluxes (and performs a convective adjustment, if necessary) as a function of pressure, latitude, and time in the atmosphere of Uranus above the 40 bar level. The dynamical heat fluxes due to baroclinic eddies in stable portions of the atmosphere are calculated in terms of a mixing length formulation for sloping convection (Stone, 1972; Ingersoll and Porco, 1978). Since the model includes horizontal as well as vertical heat fluxes, it enables us to make a theoretical study of the meridional energy balance. In this sense, it is like a seasonal climate model for Uranus.

In implementing this model, two assumptions are made concerning convection. First, it is assumed that the small departures of the potential temperature from adiabaticity in convecting regions (including the convective interior) are much smaller than potential temperature variations in stable regions and can be ignored. As shown by Ingersoll and Porco (1978), some departures from adiabaticity do occur in the deep atmosphere and interior, but they are extremely small compared to the ~1 K variations calculated here for the 1 bar level. The temperature in convecting regions, therefore, follows an adiabat exactly. From this assumption

we infer that the interior can supply the internal heat fluxes we calculate without significantly altering the lower boundary condition, which is that the potential temperature at the 40 bar level is constant with respect to latitude and season. Thus, Ingersoll and Porco's work and the present work complement each other. The former solves for the (small) potential temperature differences in the interior, given a certain latitudinal distribution of internal flux at the surface. The present work solves for the seasonal latitudinal distribution of internal flux at the base of the atmosphere, given a certain latitudinal distribution of absorbed sunlight and a (nearly) adiabatic interior. The fact that the internal potential temperature differences are so much smaller than those in the atmosphere allows the two problems to be treated separately.

A second assumption made for the model is that the convective time scale is short compared to the radiative and dynamical time scales. This assumption allows a convective adjustment (Manabe and Wetherald, 1967) to be made in the convective regions and removes the need to explicitly calculate the convective flux. Direct numerical calculation of the convective flux from mixing length theory is difficult in practice because of the great disparity between the convective and radiative time scales on Uranus (Wallace, 1983).

A description of the radiative-convective-dynamical model and some details concerning the computational method are offered in the next section. In Section 3, we discuss the seasonal meridional energy balance as a function of the parameter E, which is defined as the ratio of the annually averaged thermal infrared power emitted by Uranus to the absorbed solar power. E-1 is thus the annual-average internal power expressed in units of the absorbed solar power. The effect on the results of Section 3 of the assumed vertical profile of solar heating is discussed in Section 4. Section 5 presents the effective temperatures and 450-900 mbar temperatures produced by the model for the time at which Voyager 2 encountered Uranus. Section 6 offers a summary and some conclusions regarding this work.

2. Method of Computation

In this section, we will discuss the radiative-convective-dynamical model, describe the computational method, and introduce the four solar heating profiles that will be used for this study.

The model calculates the diurnal-average temperature and heat fluxes as a function of pressure, latitude, and season, by numerical time-marching of the thermodynamic energy equation

$$\rho C_P (p/p_0)^{R/C_P} \frac{d\theta}{dt} = - \nabla \cdot F \qquad (3.1)$$

Here ρ is the mass density, C_P the specific heat at constant pressure, p the pressure, p_0 the reference pressure for potential temperature (taken to be 36.4 bar), R the gas constant, θ the potential temperature, and F the total heat flux. The calculation extends from the north pole to the south pole, and from a base pressure of 40 bar to zero pressure. The grid is divided into 20 equally spaced intervals of latitude, and there are 5 grid points per pressure scale height in the vertical (amounting to a total of 40 vertical divisions). Some of the calculations were repeated with twice the number of latitude intervals, and it was found that the heat fluxes on the more finely divided

grid agreed to within 5% of those on the coarse grid at points where a direct comparison could be made.

The system is started from an arbitrary initial state and has a fixed potential temperature θ_0, constant in latitude, at the lower boundary. θ_0 represents the potential temperature of the convective interior and changes only on a time scale much longer than the time scales of interest here (Ingersoll and Porco, 1978). It can therefore be treated as an input parameter. For a given value of θ_0 and a given planetary bond albedo, the model computes the total emitted power and hence E, the ratio of the annual-average emitted power to absorbed sunlight. This ratio is varied by varying θ_0; the bond albedo is held fixed.

The system is stepped forward in time until various test parameters (such as the emitted flux at the north pole and equator, or the 500 mbar temperature at the equator, etc.) show a steady seasonal oscillation. The criteria to determine this are that the difference between the values of the test parameter evaluated one oscillation period apart be much less ($\leq 10^{-3}$) than the amplitude of the seasonal oscillation and much less than initial changes in the parameter. An example of the convergence of the system to a steady seasonal oscillation is shown in Figure 3-1. The time step is chosen so that there are 1000 to 2000 time steps per Uranian year. The model is always integrated

Figure 3-1. Emitted flux at the north pole, in units of .655 Wm^{-2}, vs. time in Uranian years, showing a typical criterion used to check convergence of the time-marching to a steady seasonal oscillation. The decay time of the initial transient, about 2 Uranian years, is a measure of the radiative time constant of the atmosphere. The results presented in this paper were produced from models run out to at least 16 Uranian years.

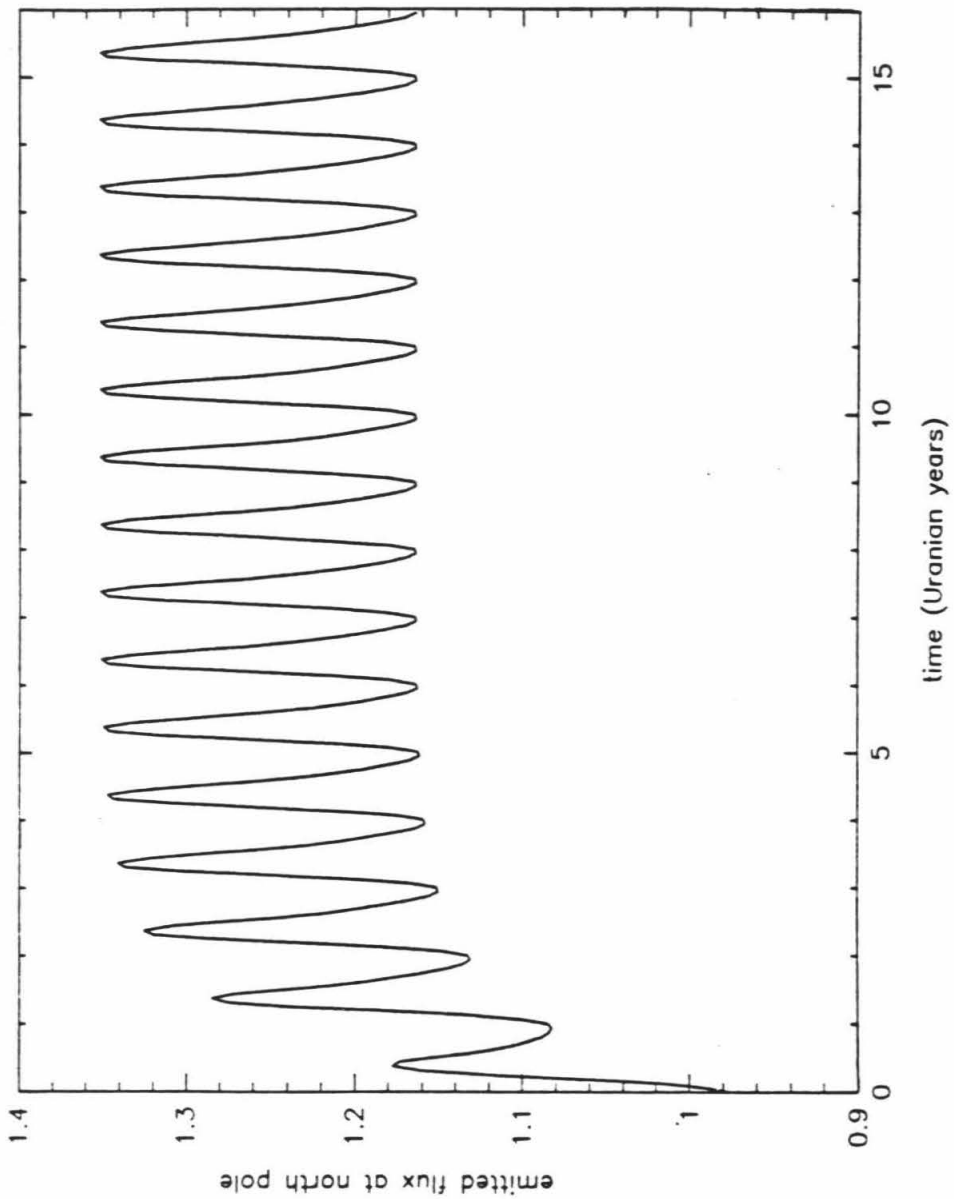
emitted flux at north pole
1.4
1.3
1.2
1.1
1
0.9
0
5
10
15
time (Uranian years)

forward in time at least 16 Uranian years before we examine the seasonal behavior.

The calculation at each time step proceeds by using the current potential temperature distribution to evaluate the thermal infrared and dynamical heat fluxes. These fluxes are added to the solar flux. The total flux distribution is then used to march the potential temperature distribution forward one time step. A convective adjustment (described in more detail below) is made to any layers that have become convectively unstable. The resulting potential temperature distribution then becomes the input for the next time step.

The atmosphere is taken to be composed of a mixture of 90% mole-fraction hydrogen, and 10% helium. In the model, the specific heat at constant pressure, C_p, has a constant value of 3R. In the real Uranian atmosphere, the specific heat will vary with temperature in a way determined by the thermodynamic behavior of ortho-para hydrogen (Trafton, 1967:, Conrath and Gierasch, 1984). The true value of the dry adiabatic lapse rate depends on the local value of C_p. The value of C_p chosen for the model is meant to be a compromise between the thermal equilibrium and frozen equilibrium values at temperatures greater than 80 K, which are the temperatures characteristic of Uranus' adiabatic region.

The atmospheric opacity at infrared wavelengths is taken to be entirely due to pressure-induced absorption from H_2-H_2

and H_2-He collisions. The ortho and para hydrogen fractions are assumed to be determined by equilibrium at the ambient temperature. The temperature-dependent absorption coefficient for H_2-H_2 has been adopted from Dore et al. (1983) and for H_2-He by Cohen et al. (1982). Thermal emission in the atmosphere of Uranus is appreciable only in the 0-1500 cm^{-1} spectral region; monochromatic fluxes in this range are integrated to obtain the total thermal flux. The two-stream approximation (Chandrasekhar, 1960) to the radiative transfer equation is used to find the net infrared irradiance at each pressure level.

The dynamical heat flux due to large-scale eddies is parameterized in terms of the local gradient of potential temperature:

$$F_V = \frac{p}{\kappa T} \left(\frac{g}{T} \right)^{3/2} \frac{l_V^2}{f^2} \left(\beta |\nabla\theta| \right)^{5/2} \cos^3 \frac{\psi}{2} \qquad (3.2a)$$

$$F_H = - F_V \tan \frac{\psi}{2} \operatorname{sgn} \left(\frac{\partial\theta}{\partial\phi} \right) \qquad (3.2b)$$

$$\cos \psi = - \left(\partial\theta/\partial z \right) / |\nabla\theta| \qquad (3.2c)$$

where F_v and F_H are the vertical and horizontal dynamical heat fluxes, p is the local pressure, T is the temperature, g is the gravitational constant, l_v is the vertical mixing length, f the local coriolis parameter, $\beta = (p/p_o)^\kappa$, and ϕ is the colatitude. The mixing-length diffusivity goes to infinity at the equator, since it is proportional to $1/f^2$, and f vanishes at the equator. This divergence of the diffusivity forces the choice of an impractically small numerical time step to insure the stability of our computational scheme. To avoid this difficulty, we have set the coriolis parameter at latitudes lower than 18° equal to its value at ±18° latitude. The angle ψ is such that $\pi - \psi$ is the local angle between the lines of constant potential temperature and the horizontal.

The above formulation was introduced by Ingersoll and Porco (1978) for the case where the planetary rotation affects the dynamics. The one difference is that the vertical derivative of potential temperature in their Eq. (24) has been replaced by the magnitude of the total gradient in Eq. (3.2a). This substitution allows a more realistic estimate of the heat flux under neutrally stable conditions with a meridional temperature gradient. Both formulations have the virtue of reducing to the parameterization given by Stone (1972) in the limit of strong stable stratification, $\cos(\psi/2) \approx 1/2|\partial\theta/\partial y|/|\partial\theta/\partial z| << 1$, provided the vertical mixing length, l_v, is chosen to

be equal to the local scale height. In all the model runs described in this paper, the stratification was found to be in the strong limit wherever the dynamical fluxes were appreciable. Consequently, the dynamical fluxes generally had the same values as would have been obtained if we had applied Stone's (1972) parameterization directly.

Stone's parameterization of the dynamical flux is found by calculating correlations between eddy velocities and eddy potential temperatures from baroclinic stability theory and by assuming the amplitudes of the growing disturbances are limited by nonlinear effects. The model for the stability of a thermal wind which he uses is that of Eady (1949). Since Eady's model does not include ß-effects (i.e., effects associated with the latitudinal variation of the coriolis parameter), these effects are absent from Stone's (1972) parameterization, and are absent from the formulation of Ingersoll and Porco (1978) as well. The potential importance of ß-effects to his parameterization is discussed by Stone (1974). Generally, these effects will significantly modify Stone's original parameterization when the local baroclinicity b', as defined in Stone (1974), eq. 5.5, is much greater than unity. In our results, b' is generally less than unity, but it does exceed unity at low latitudes. Ignoring the ß-effect where it is important can lead to an overestimate of the efficiency with which baroclinic eddies transport heat (Held, 1978). Hence, it is

possible that the model overestimates the ability of baroclinic eddies to transport heat at low latitudes ($\lambda<30°$).

It is appropriate to inquire here whether baroclinic eddies should be properly considered the dominant mode of meridional heat transport in the atmosphere of Uranus. As pointed out by Stone (1976), if the static stability is sufficiently high, a symmetric Hadley circulation might take over as the principal heat transport mechanism. This could occur if the scale of the baroclinic eddies exceeds the planetary scale, if dissipative effects are strong, or if the vertical shear of the zonal wind is sufficiently small. In our results, we find the typical scale of a baroclinic eddy (assumed equal to the local radius of deformation NH/f, where N is the Brunt-Vaiasala frequency and H is the pressure scale height) to be ~1600 km at 30° latitude. Hence, the scale of the eddies is much less than the planetary scale (~26000 km) in our model, except near the equator. The stability of a zonal wind on a fluid planet has been studied by Conrath et al. (1981). They find that Eady ($\beta=0$) modes are strongly suppressed by the presence of a deep, adiabatic, fluid interior. Prograde (eastward) jets are found to be stable to Charney ($\beta\neq0$) instability modes, but retrograde jets are unstable to these modes for any value of the vertical shear of the zonal wind. The onset of instability and character of the unstable modes depend on

both the horizontal and vertical shears of the zonal wind. The point we wish to make here is that the stability of zonal flows on Jovian planets is a complicated issue, and therefore one should exercise caution before attempting to characterize the flow regime by using a simple set of criteria based on the wind shear. At any rate, it is certainly possible that a Hadley circulation may be the dominant mode of heat transport on Uranus, especially at low latitudes. Unfortunately, our present understanding of the circulation regimes of Jovian planets is insufficient at this time to settle the issue.

The treatment of small-scale convection differs in one important respect from the conventional treatment for thin-atmosphere planets. As is commonly done in conventional radiative-convective models (e.g., Manabe and Wetherald, 1967), a convective adjustment is made at each time step wherever the stratification is unstable. This adjustment keeps the temperature gradient on a dry adiabat while conserving the enthalpy of the unstable layer. An exception occurs, however, for the unstable layer in contact with the convective deep atmosphere. No effort is made to conserve the enthalpy of this layer. Instead, it is assumed that such a layer can freely extract the heat from the deep atmosphere that is required to maintain it on the deep adiabat.

The internal heat flux is calculated by considering the energy budget of an atmospheric column. The difference between the thermal radiative plus horizontal dynamical power leaving the column, the solar plus horizontal power entering the column, and the enthalpy storage rate, equals the internal power.

The parameterization used for the solar flux is

$$S(\lambda,p,L_S) = S_0(\lambda,L_S)\ Tr(p) \qquad (3.3)$$

where $S_0(\lambda,L_S)$ is the diurnal-average net (absorbed) solar flux incident at latitude λ and orbital phase L_S (where L_S=0 at vernal equinox), and Tr(p) is the transmission of sunlight to pressure level p. $S_0(\lambda,L_S)$ is evaluated numerically for Uranus' obliquity of 98°. The eccentricity of Uranus' orbit is taken to be zero. The bolometric bond albedo is taken to have the value 0.35 (Pollack et. al.,1986), independent of latitude.

It is possible to vary the parameter E , the ratio of emitted power to absorbed solar power, by varying the albedo while holding the interior potential temperature θ_0 fixed. Varying the albedo changes the amount of absorbed sunlight; varying θ_0 changes the amount of internal heat, and therefore the emitted power. In this study, we have elected to vary E by changing θ_0 while holding the albedo fixed.

Since the vertical transmission of solar energy in the atmosphere of Uranus is still poorly constrained by current data, we have elected to find the general response of the system to four different models for the transmission of sunlight. Between them, they differ in the altitude at which the solar heating reaches its maximum or in the vertical extent over which most of the sunlight is deposited. The four models used for the solar heating are shown in Figure 3-2. The figure shows Q_p vs. pressure, where

$$Q_p = \partial\ Tr(p)/\partial\ \ln\ p \qquad (3.4)$$

is proportional to the solar heating. The transmission profiles for models M (for "medium altitude"), H (for "high-altitude"), and L (for "low-altitude") have been chosen to follow

$$Tr(p) = \exp(-p/p_{max}) \qquad (3.5)$$

The parameter p_{max} is the pressure level at which the solar heating has its maximum. P_{max} = 1.8 bar for model M, 0.9 bar for model H, and 3.6 bar for model L. The shape of the solar heating profile Q_p for these three models is the same, but the peak for each occurs at p_{max}. Model C (for "cloud") places the solar heating peak at the same level as model M,

Figure 3-2. The four models used for the vertical profile of solar heating in this study. Q_p measures the rate of change of solar transmission with log pressure. Models M, H, and L have the same shape but differ in the pressure level p_{max} where the solar heating peaks. P_{max}=1.8 bar for model M; p_{max}=0.9 bar for model H; p_{max}=3.6 bar for model L. Model C places the peak of solar heating at the same level as model M but concentrates the heating into a narrower extent of altitude.

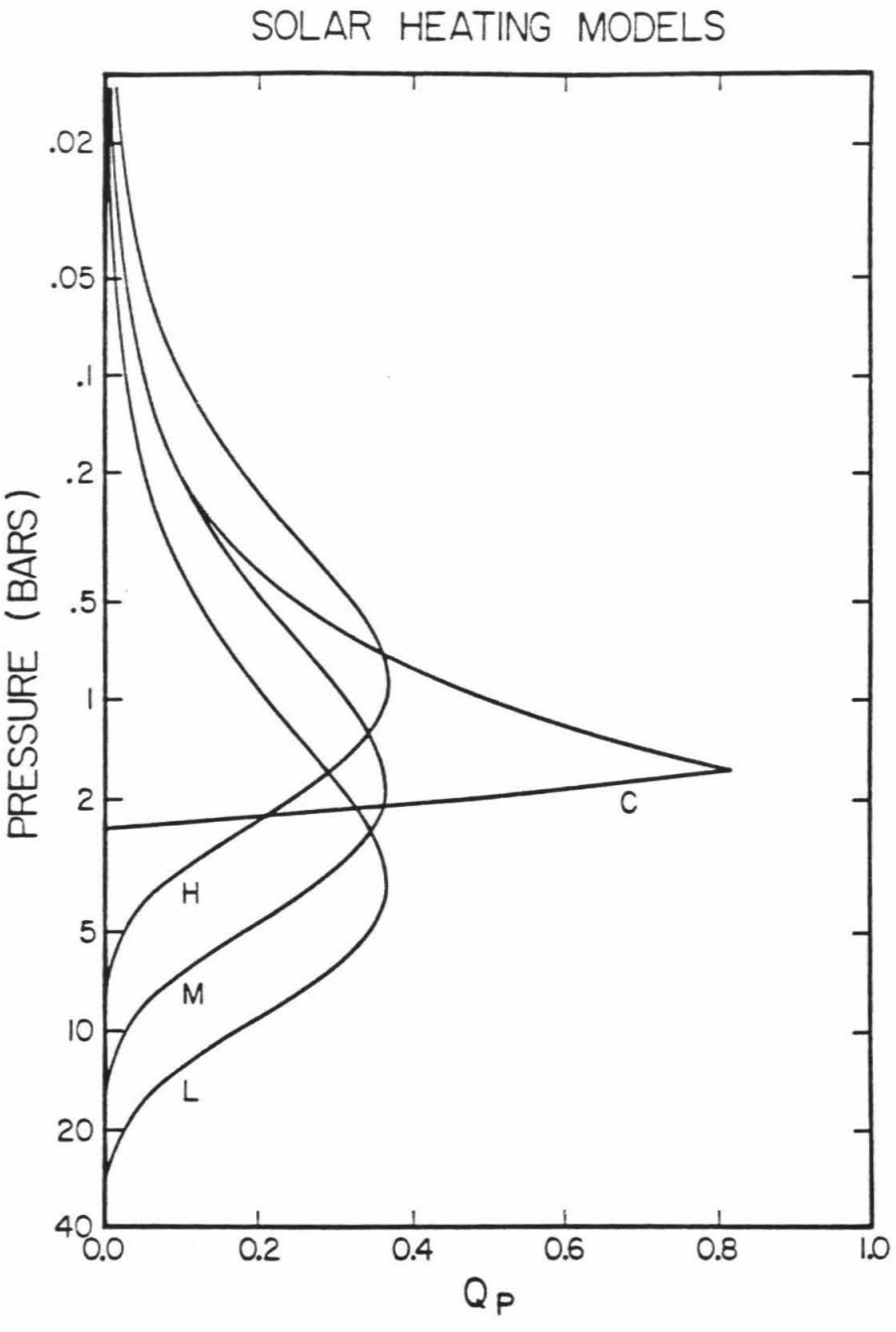
SOLAR HEATING MODELS
PRESSURE (BARS)
.02
.05
.1
.2
.5
1
2
5
10
20
40
0.0
0.2
0.4
0.6
0.8
1.0
Q_P
C
H
M
L

i.e., 1.8 bar, but the heating is concentrated into a narrower altitude range, and no heating whatsoever occurs below 2 bar. This model is meant to cover the case of an opaque, non-conservative cloud at ~1.8 bar (Wallace, 1980).

Of course, one cannot expect these simple models to represent in any quantitatively accurate form the true solar transmission in the atmosphere of Uranus. For instance, the true transmission profile may show a dependence on latitude and season in addition to pressure or may have a much more complicated dependence on pressure than is represented by Eq. (3.5). Rather, these simple models have been designed to give us a qualitative understanding of how various features of the solar heating profile affect the meridional energy balance. The calculations merit being repeated when the solar heating profile is more constrained by observations. The sensitivity of the meridional energy balance to the solar heating profile is discussed in Section 4.

3. Seasonal Meridional Energy Balance

In this section, we discuss the seasonal meridional energy balance for several values of E. The solar heating is assumed to follow profile M (Fig. 3-2).

The meridional energy balance is investigated by dividing the atmosphere above the 40 bar level into adjacent columns, each 9° wide in latitude, and calculating the energy budget for each column. In each column energy must be conserved:

$$\frac{dH}{dt}(L_S,\lambda) = S(L_S,\lambda) + I(L_S,\lambda) - F(L_S,\lambda) + Q_D(L_S,\lambda) \quad (3.6)$$

Here, H is the total (vertically integrated) enthalpy per unit area (Wallace and Hobbs, 1977; p.65); S is the absorbed solar flux; I is the internal flux; F is the thermal infrared flux emitted to space; Q_D is the vertically integrated convergence, per unit area, of the dynamical heat flux; L_S is the orbital phase, where L_S=0 corresponds to vernal equinox; λ is the latitude. Each of the terms in Eq. (3.6) is plotted as a function of latitude and season, for values of E ranging from E=1.10 to E=4.85, in Figures 3-3 through 3-6. Each panel corresponds to a different part of the Uranian year, given by the value of L_S. Only one-half of a Uranian year is shown. Since we have taken the orbital

Figure 3-3. The meridional energy balance as a function of latitude and season, for E=1.10. Each panel corresponds to a particular orbital phase L_S, where L_S=0 corresponds to vernal equinox. F= thermal infrared irradiance emitted to space; S= absorbed solar flux; I= internal flux; H= rate of enthalpy storage per unit area; Q= dynamical heating per unit area. Q is offset downward 2 units for clarity. All these quantities are expressed in units of .655 Wm^{-2}.

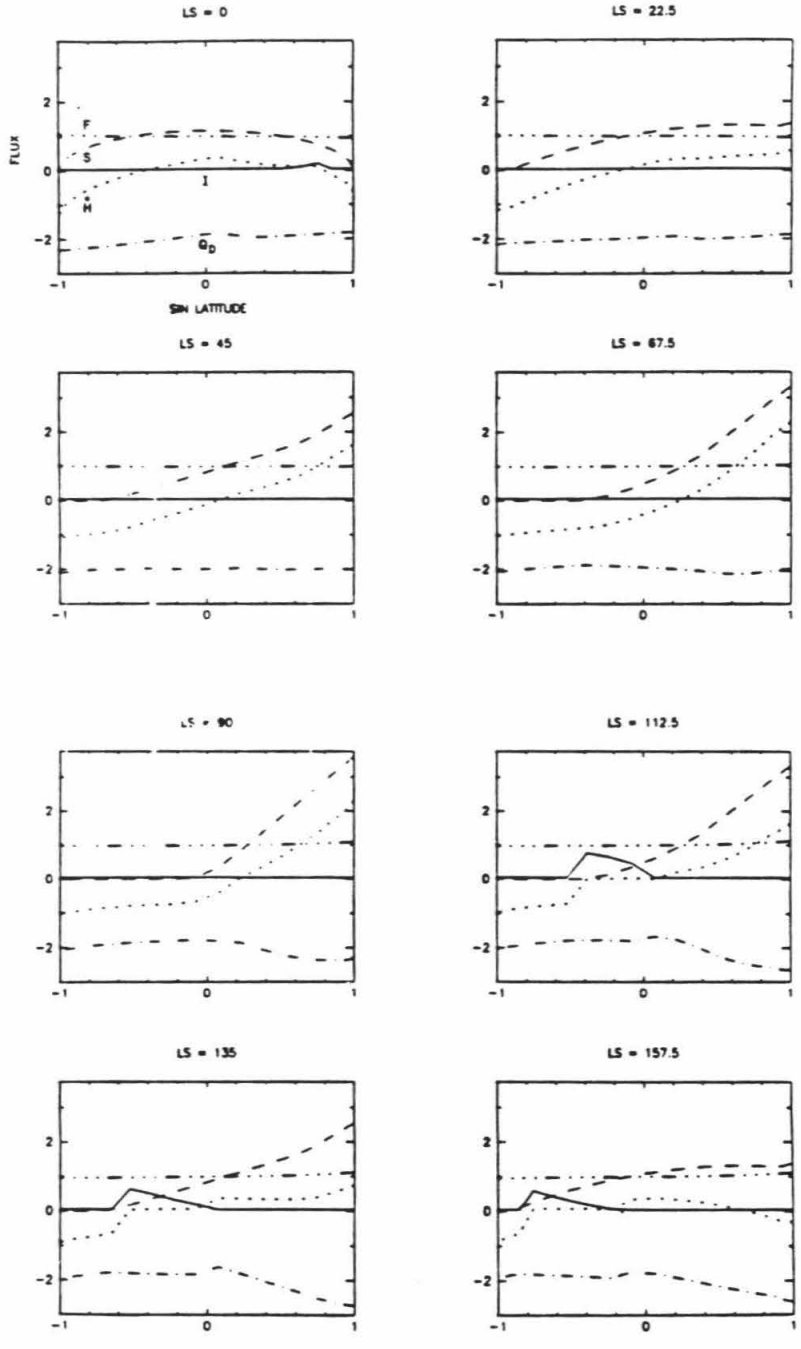
LS = 0
LS = 22.5
LS = 45
LS = 67.5
LS = 90
LS = 112.5
LS = 135
LS = 157.5
FLUX
SIN LATITUDE
F
S
I
M
Q_D

Figure 3-4. Same as Fig. 3-3 except E=1.23.

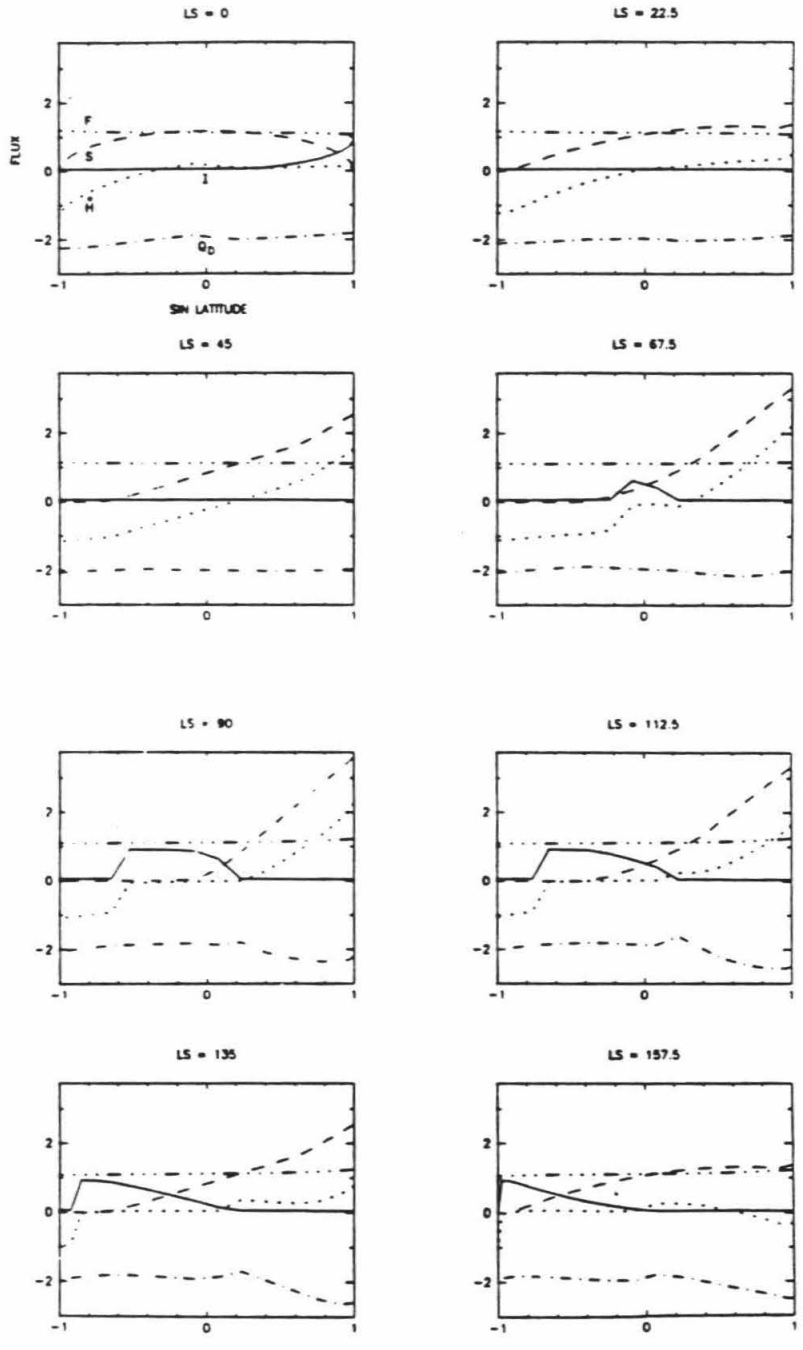
LS = 0
LS = 22.5
LS = 45
LS = 67.5
LS = 90
LS = 112.5
LS = 135
LS = 157.5
FLUX
SIN LATITUDE
F
S
I
M
Q_D

Figure 3-5. Same as Fig. 3-3 except E=1.33.

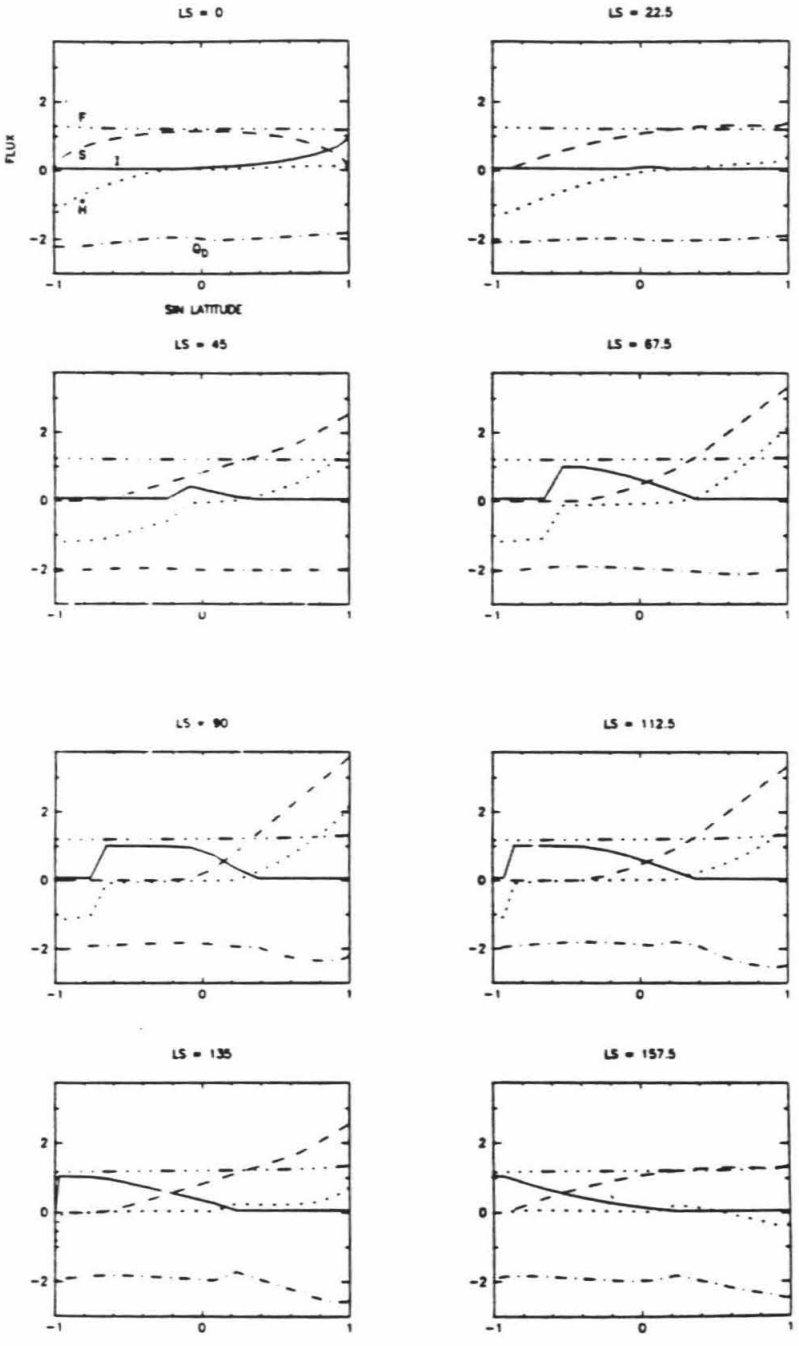
LS = 0
LS = 22.5
LS = 45
LS = 67.5
LS = 90
LS = 112.5
LS = 135
LS = 157.5
FLUX
SIN LATITUDE
F
S
I
H
Q_D

Figure 3-6. Same as Fig. 3-3 except E=4.85.

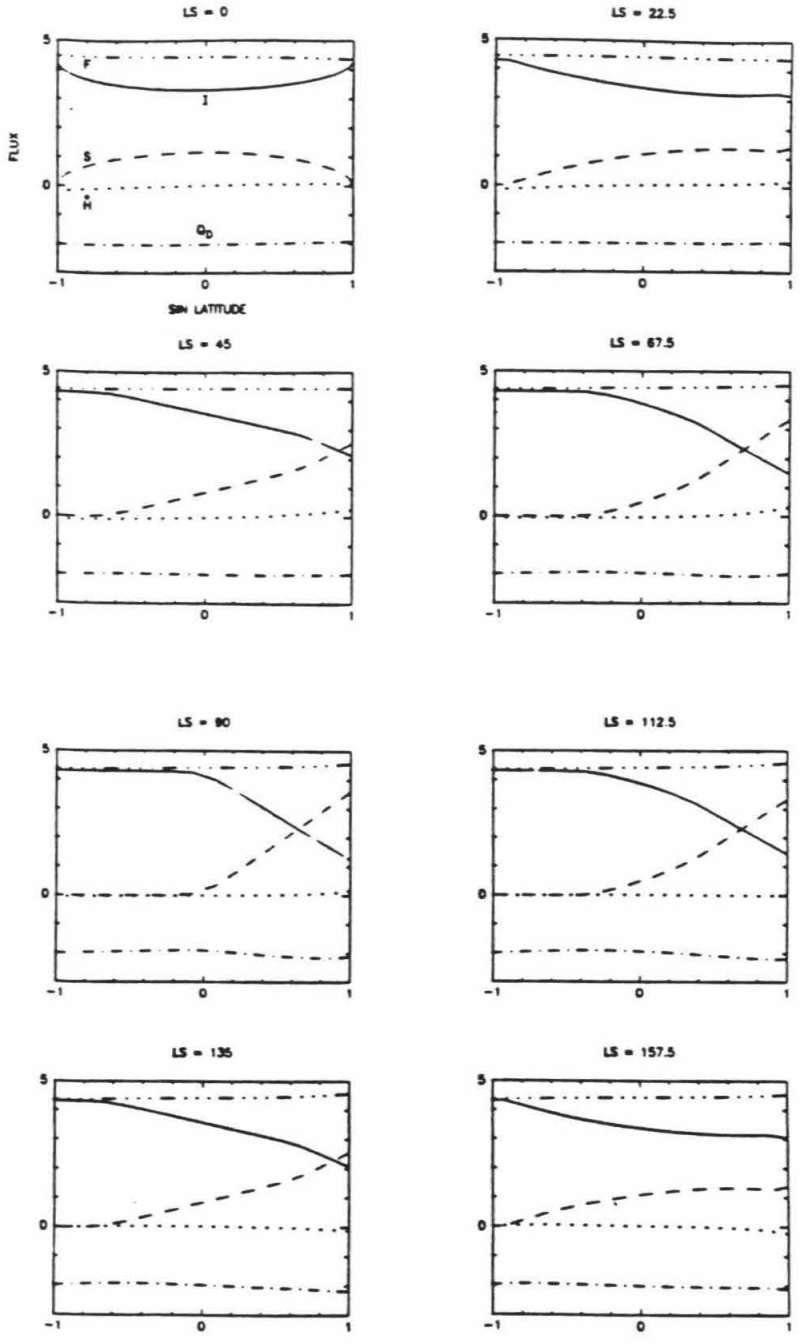
LS = 0
LS = 22.5
LS = 45
LS = 67.5
LS = 90
LS = 112.5
LS = 135
LS = 157.5
FLUX
SIN LATITUDE
F
I
S
H*
Q_D
5
0
-1
0
1

eccentricity of Uranus to be zero, the behavior at, e.g., the north pole over the second half of the year is the same as the behavior at the south pole over the first half of the year, and so on. It can be seen from an examination of Figures 3-3 through 3-6 that the internal flux varies with latitude and season. At some times during the year, the planet divides into two types of regime. In one regime, the internal flux is uniform with latitude, and its magnitude remains fairly low relative to the thermal emission. We will refer to this as the terrestrial regime. Note that the terrestrial regime does not appear for the very high E case shown in Fig. 3-6. In the other regime, the magnitude of the internal flux becomes variable with latitude and is often several times larger than the internal flux in the terrestrial regime. This is the jovian regime. As can be seen in Figs. 3-3 and 3-4, there may be periods during a Uranian year, particularly for low E, when only the terrestrial regime is present.

The seasonal formation and persistence of the jovian regime depends on the value of E. It always appears first near the equator, then extends itself into the winter hemisphere. At low E, its greatest poleward extent only reaches mid-latitudes. At high E, it can extend all the way to the winter pole. The jovian regime appears just after winter solstice in the dark hemisphere, for low E, and persists until vernal equinox. For higher E, it can appear

sooner, before winter solstice, and last further into the spring.

The nature of the meridional energy balance is found to be different in the terrestrial and jovian regimes. Inspection of Figs. 3-3 through 3-5 shows that the enthalpy storage rate dH/dt is substantial in the terrestrial regime but small in the jovian regime. In the terrestrial regime, dH/dt in Eq. (3.6) is to first order balanced by the difference S-F of the absorbed sunlight and thermal emission, although there is a seasonally variable contribution from the dynamical heating, Q_D, as well. Q_D reaches its peak magnitude and is negative in a given hemisphere during late summer, ~1/8 orbital period after the summer solstice. The internal heat flux I is uniform with latitude in the terrestrial regime. In the jovian regime, however, I to first order equals F-S, although there is still a small contribution to the thermal balance from Q_D. The enthalpy storage rate dH/dt becomes small, however. The enthalpy storage rate and internal flux seem to exchange roles in the two regimes. In the terrestrial regime, I is small and dH/dt is comparable to the other terms in Eq. (3.6). In the jovian regime, dH/dt becomes small and I is comparable in size to the other terms.

The thermal structure is found to have different characteristics associated with the two regimes. Figure 3-7 shows contours of potential temperature plotted on a

meridional cross section in pressure and latitude, for the case E=1.33. At orbital phase L_S=0 (upper left panel), the entire northern hemisphere is in the jovian regime, while the southern hemisphere is in the terrestrial regime (cf. Fig. 3-5, L_S=0). In the jovian regime, there is only one radiative-convective boundary, occurring at ~450 mbar. This boundary is the usual one associated with the interface between a convection zone and a radiative zone, where the atmosphere becomes optically thin to thermal infrared radiation. In the terrestrial regime, there are two radiative-convective boundaries. The uppermost one, occurring at ~450 mbar, owes its existence to the atmosphere's becoming optically thin to infrared radiation above 450 mbar, and is thus entirely analogous to the single radiative-convective boundary in the jovian regime. The lower radiative-convective boundary in the terrestrial regime is more unusual. It forms at a very deep level in the atmosphere, at 13.4 bar in the case shown in Fig. 3-7. At this depth, the gas is optically thick in the infrared. The stable stratification associated with this boundary forms as a result of solar heating at higher altitudes. Consequently, the lower radiative-convective boundary is situated below the altitude of peak solar heating, which for model M is itself situated well below the 450 mbar level. The lower radiative-convective boundary in the terrestrial regime is therefore found to occur much deeper in the

Figure 3-7. Contours of potential temperature θ shown on a meridional cross section of the atmosphere taken between 40 bar and 365 mbar. The lines actually correspond to contours of $\delta\theta/\theta_0-1$, where $\delta\theta=\theta-\theta_0$, and θ_0= potential temperature of the adiabatic interior. The dashed contour corresponds to a value of 10^{-5}. The other contours are equally spaced by increments of 3×10^{-3}. For this case, θ_0=262 K, corresponding to E=1.33.

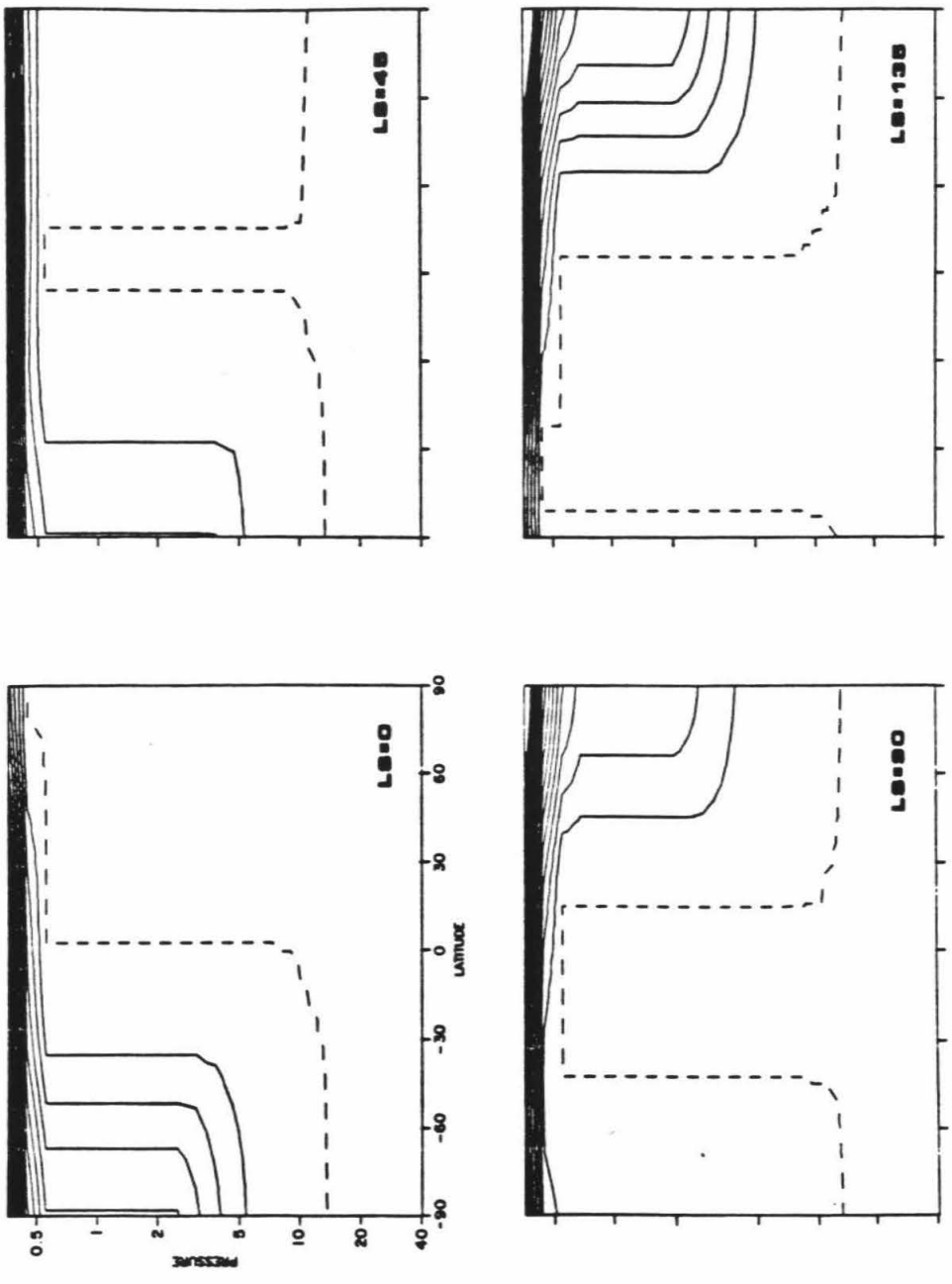
Ls=0
Ls=45
Ls=90
Ls=135
LATITUDE
PRESSURE
90
60
30
0
-30
-60
-90
0.5
1
2
5
10
20
40

atmosphere than the radiative-convective boundary in the jovian regime.

As seen in Fig. 3-7, the jovian and terrestrial regimes change their positions and extent with season. By the time L_S=135, the terrestrial regime has moved over to dominate the northern hemisphere while the jovian regime has moved to the southern hemisphere.

Both the vertical and horizontal components of the dynamical heat flux are relatively small in the deep stable layer of the terrestrial regime. The vertical component is found to be typically $F_V \sim 5 \times 10^{-4}$ Wm^{-2}, much less than the $\sim .04$ Wm^{-2} of infrared flux transported vertically through the layer. A typical value for the horizontal component of the dynamical heat flux in the deep stable layer is ~ 1 Wm^{-2}, much less than the ~ 30 Wm^{-2} horizontal heat flux typical of the upper stable region where the atmosphere is optically thin in the infrared. Thus, when we speak of meridional heat transport by the atmosphere, it is to be understood that this transport occurs predominantly in the upper stable region.

It can be deduced from Figs. 3-3 through 3-5 that the total internal power varies seasonally over a Uranian year. This is presented more clearly in Figure 3-8, where the emitted thermal power, absorbed solar power, internal power, and global enthalpy storage rate are plotted against orbital phase L_S for three different values of E. Each of these

Figure 3-8. The emitted thermal power EM, absorbed solar power A, internal power I, and global enthalpy storage rate DH, plotted against orbital phase L_S. EM and A are virtually constant over an orbital period. I and DH oscillate in phase with a period of 1/2 Uranian year. The power is expressed in units of 2.7×10^{15} W.

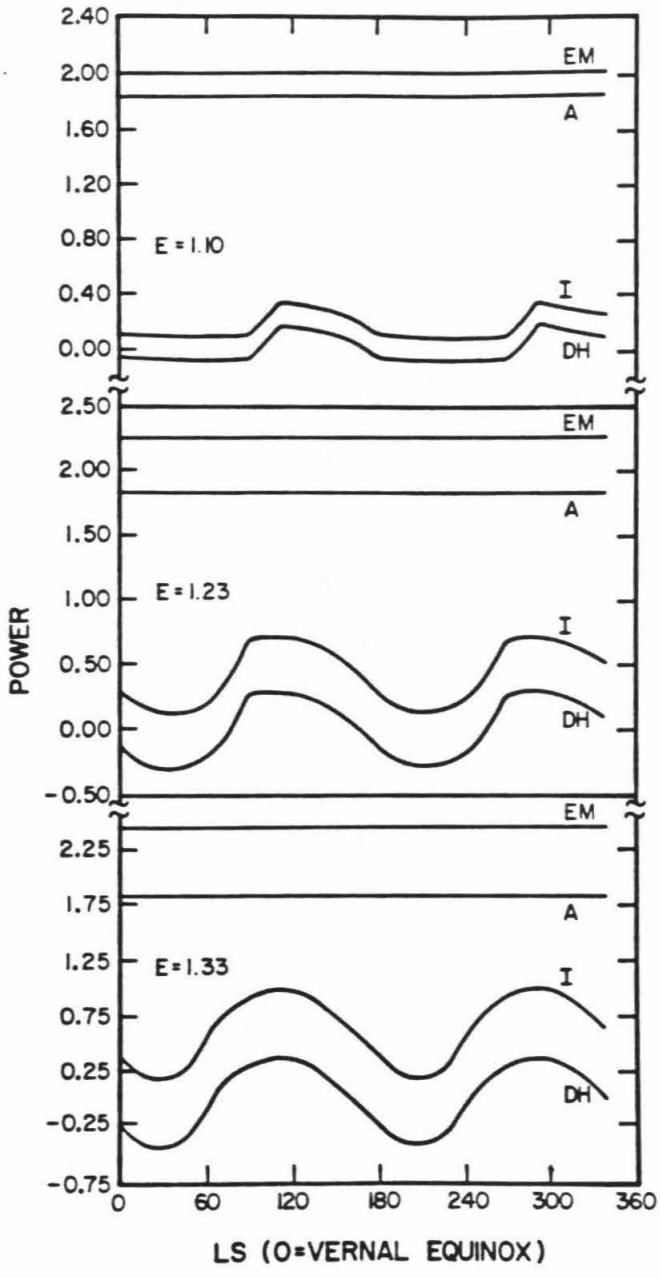
2.40
2.00
1.60
1.20
0.80
0.40
0.00
EM
A
E = 1.10
I
DH
2.50
2.00
1.50
1.00
0.50
0.00
-0.50
EM
A
E = 1.23
I
DH
2.25
1.75
1.25
0.75
0.25
-0.25
-0.75
EM
A
E = 1.33
I
DH
POWER
0
60
120
180
240
300
360
LS (0=VERNAL EQUINOX)

powers is simply the surface integral, taken over the entire planet, of the corresponding flux appearing in Eq. (3.6). (The surface integral of Q_D is, of course, identically zero). The emitted thermal power and absorbed sunlight remain constant over the year. The internal power and global enthalpy storage rate oscillate in phase with a period of 1/2 Uranian year. Thus, there are episodes twice a year when the internal power is high and heats the atmosphere. This excess heat is lost, through thermal emission, during the periods when the internal power is low.

Annual averages of the emitted infrared, absorbed solar, and internal heat fluxes, and of the dynamical heating Q_D, are plotted against latitude in Figure 3-9. For low values of E, the annual average internal flux is approximately uniform in latitude (i.e., the differences between the internal flux and its global mean value, in units of flux, are small compared to the differences between the solar flux and its global mean). The dynamical heating Q_D approximately balances the absorbed sunlight in the sense that their sum is nearly uniform. Hence, at low E, the annual-average equatorward heat transport takes place in the atmosphere.

As E increases, the internal heat takes on a progressively more important role in the heat transfer. For E=1.33, the annual-average internal heat flux is larger at the equator than at the poles by 0.13 Wm^{-2} (~16% of the

Figure 3-9. The annually averaged emitted infrared ($\overline{F}$), absorbed solar ($\overline{S}$), and internal ($\overline{I}$) fluxes, and the annually averaged dynamical heating ($\overline{Q}$), vs. sine latitude, for four values of E. The units of flux are .655 Wm^{-2}.

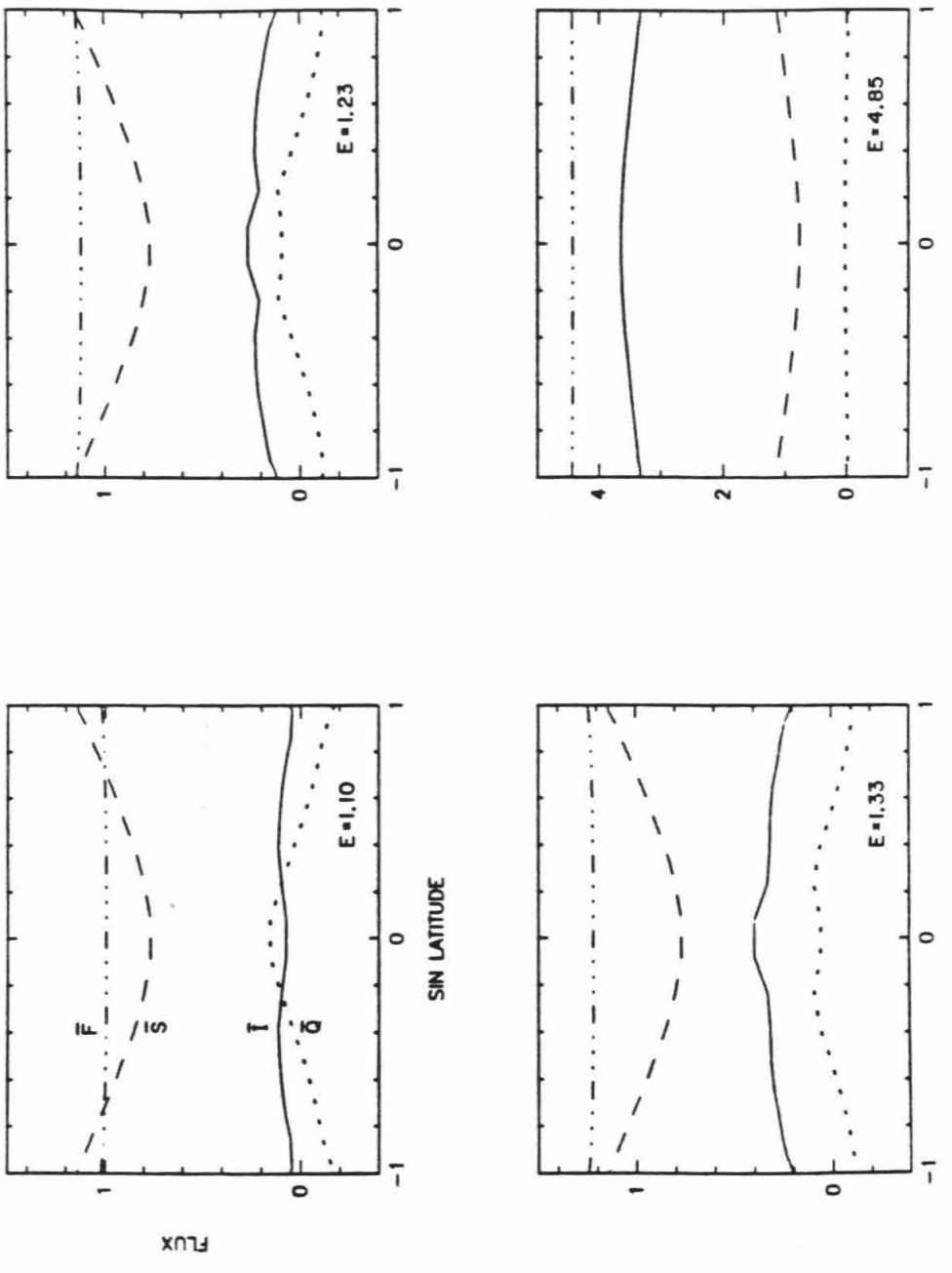
E=1.10
E=1.23
E=1.33
E=4.85
$\bar{F}$
$\bar{S}$
$\bar{I}$
$\bar{Q}$
FLUX
SIN LATITUDE

emitted flux). Such a meridional variation of the annual-average internal flux implies some meridional heat transport in the convective interior. If it is assumed that the release of energy in the interior is isotropic, then a simple relation can be found between the horizontal power of the internal heat flow at latitude λ, $P_I(\lambda)$, and the annual-average internal flux at the base of the atmosphere at latitude λ:

$$\frac{dP_I}{d\sin\lambda} = T(\lambda) - \frac{1}{2}\int_{-1}^{1} d\sin\lambda'\ T(\lambda') \qquad (3.7)$$

$T(\lambda)$ is the annual-average internal flux at the base of the atmosphere at λ as plotted in Fig. 3-9. The integral in Eq. (3.7) is simply the global mean value of $T(\lambda)$. We have plotted $P_I(\lambda)$ and $P_A(\lambda)$, the meridional power carried by the atmosphere, for four values of E, in Figure 3-10.

It can be seen in Fig. 3-10 that at low E, $P_A(\lambda)$ dominates $P_I(\lambda)$. The meridional heat transport then occurs principally in the atmosphere. When E is as high as 1.33, $P_I(\lambda)$ becomes comparable to $P_A(\lambda)$. The interior then shares the burden of heat transport equally with the visible atmosphere. At very high E, $P_I(\lambda)$ dominates $P_A(\lambda)$, and the meridional heat transport occurs mainly in the interior.

Figure 3-10. The meridional power carried by the atmosphere, $P_A(\lambda)$, and by the interior, $P_I(\lambda)$, vs. sine latitude for four cases of E. The value of E is shown in the lower right corner of each panel. The power is expressed in units of 2.7×10^{15} W. The solid line corresponds to $P_A(\lambda)$, the dashed line to $P_I(\lambda)$.

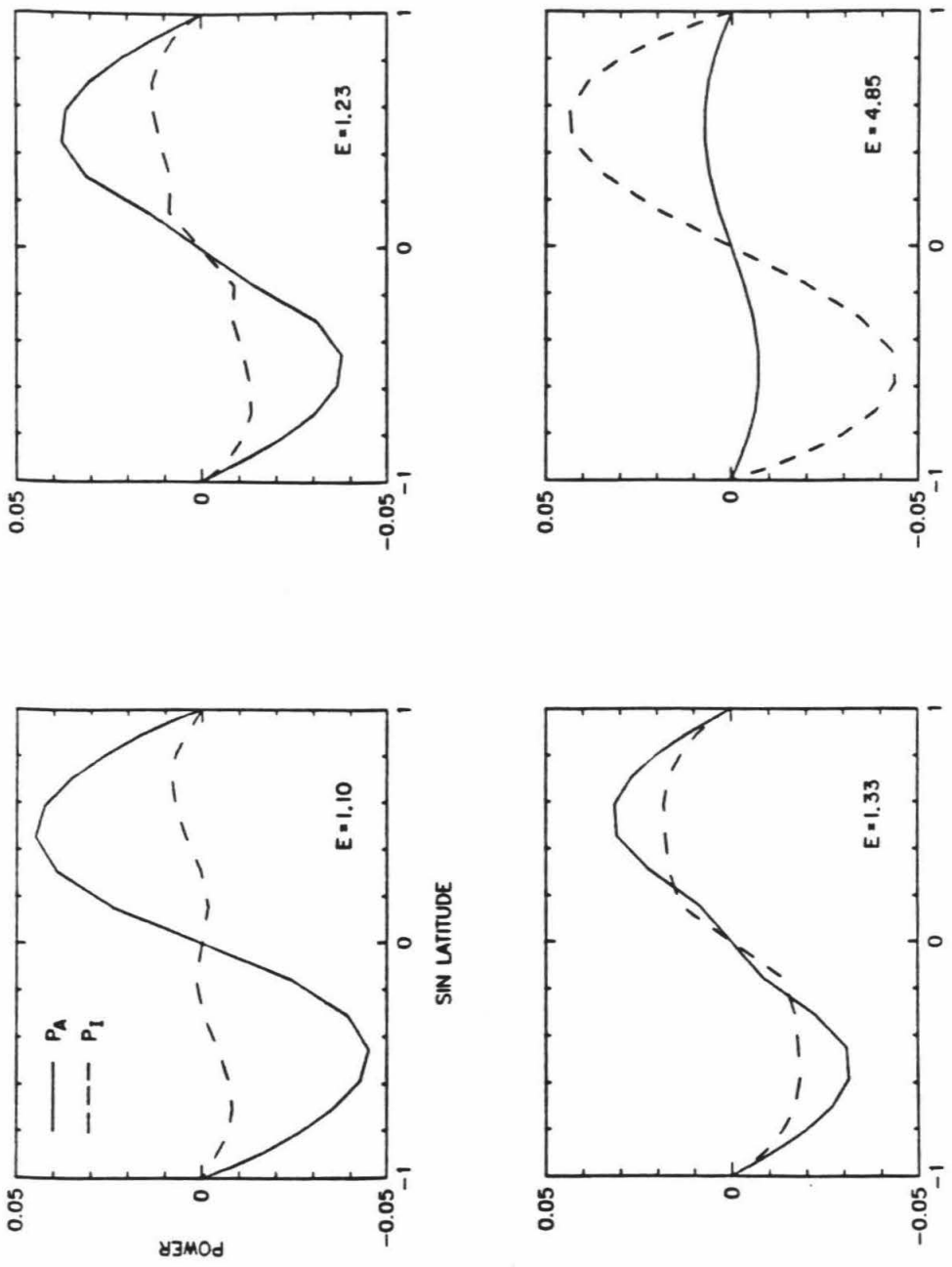
E = 1.23
E = 4.85
E = 1.10
E = 1.33
P_A
P_I
POWER
SIN LATITUDE
0.05
0
−0.05
−1
0
1

4. Effect of the Solar Heating Profile on the Meridional Energy Balance

In the last section, the meridional energy balance was discussed for various values of the parameter E, using solar heating model M to describe the vertical deposition of sunlight. In this section, we present and compare the results of model runs where profiles H, L, or C were adopted for the solar heating. All the results presented in this section correspond to E=1.37.

The general qualitative description of the seasonal meridional energy balance given in the previous section for model M is still valid when models H, L, or C are used for the solar heating. For each of these models, the jovian and terrestrial regimes appear with the same characteristic behavior of the heat fluxes and thermal structure that was described in Section 3. In particular, the seasonal meridional energy balance for models H, L, or C is quite similar to that of model M (shown in Fig. 3-5 for the case E=1.33), differing from M only in quantitative detail. The source of these quantitative differences must be related to differences in the thermal structure produced by the distinct solar heating profiles. In fact, the solar heating profile can have a strong effect on the altitude level at which the lower radiative-convective boundary forms in the terrestrial regime.

Model runs using profiles H and L can be compared to demonstrate the effect of depositing the sunlight high or low in the atmosphere. As discussed in Section 2, profiles H and L have the same shape, but in H the solar heating peaks at 0.9 bar, while in L it peaks at 3.6 bar.

As mentioned above, the depth at which the deep stable layer forms in the terrestrial regime is found to be sensitive to the altitude of peak solar heating. In model L, the base of this layer occurs at 24.4 bar, in model H, at only 4.9 bar. The effect of this on the annual average meridional energy balance is shown in the upper left and right panels of Figure 3-11. For high-altitude solar heating (model H, upper left panel), the meridional variation of the (annual-average) internal flux is much weaker than the variation in the dynamical heating. The opposite is true, however, if the sunlight is deposited fairly deeply (model L, upper right panel). We conclude that, in general, for a given E and given shape of the solar heating profile, high-altitude solar deposition favors meridional transport in the atmosphere, on an annual average basis, while deep solar penetration favors transport in the convective interior. This conclusion is substantiated in Figure 3-12a, which shows the annual-average power transported in the atmosphere and interior as a function of latitude for models H and L.

Figure 3-11. Annual-average meridional energy balance for E=1.37 and various solar heating models. $\bar{F}$, $\bar{S}$, $\bar{I}$, and $\bar{Q}$ are as defined in Fig. 9. The solar heating profile belonging to each panel is labeled in the lower right corner of the panel. Flux is measured in units of .655 Wm^{-2}.

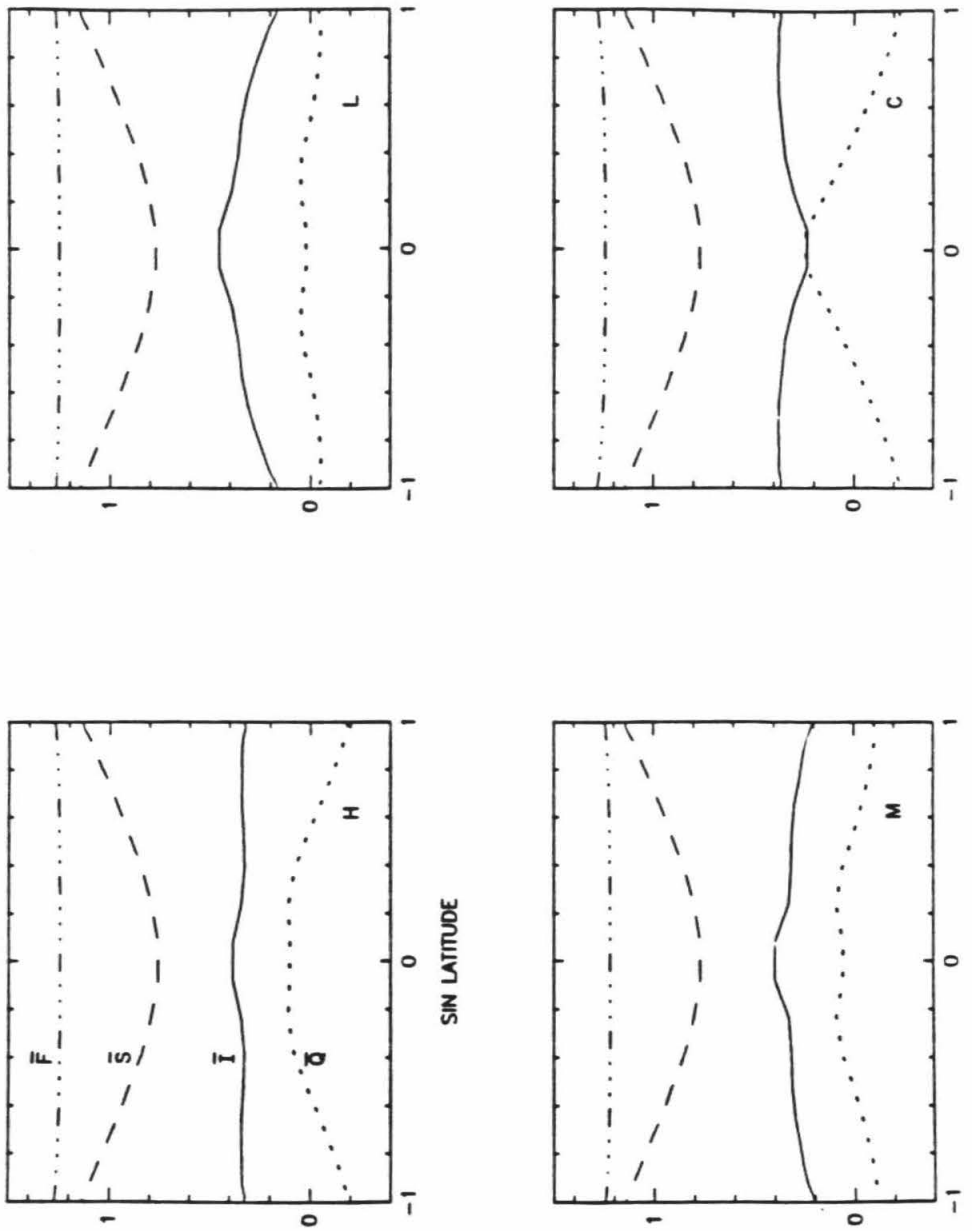
F
S
I
Q
H
L
C
M
FLUX
SIN LATITUDE
1
0
−1

Figure 3-12. (a) Annual-average power transported in the atmosphere and interior as a function of latitude for solar heating models H and L. Solid lines correspond to P_A, dashed lines to P_I. (b) Same as in (a), but for solar heating models M and C. Note the scale for power is not the same in (a) and (b). Power is expressed in units of 2.7×10^{15} W.

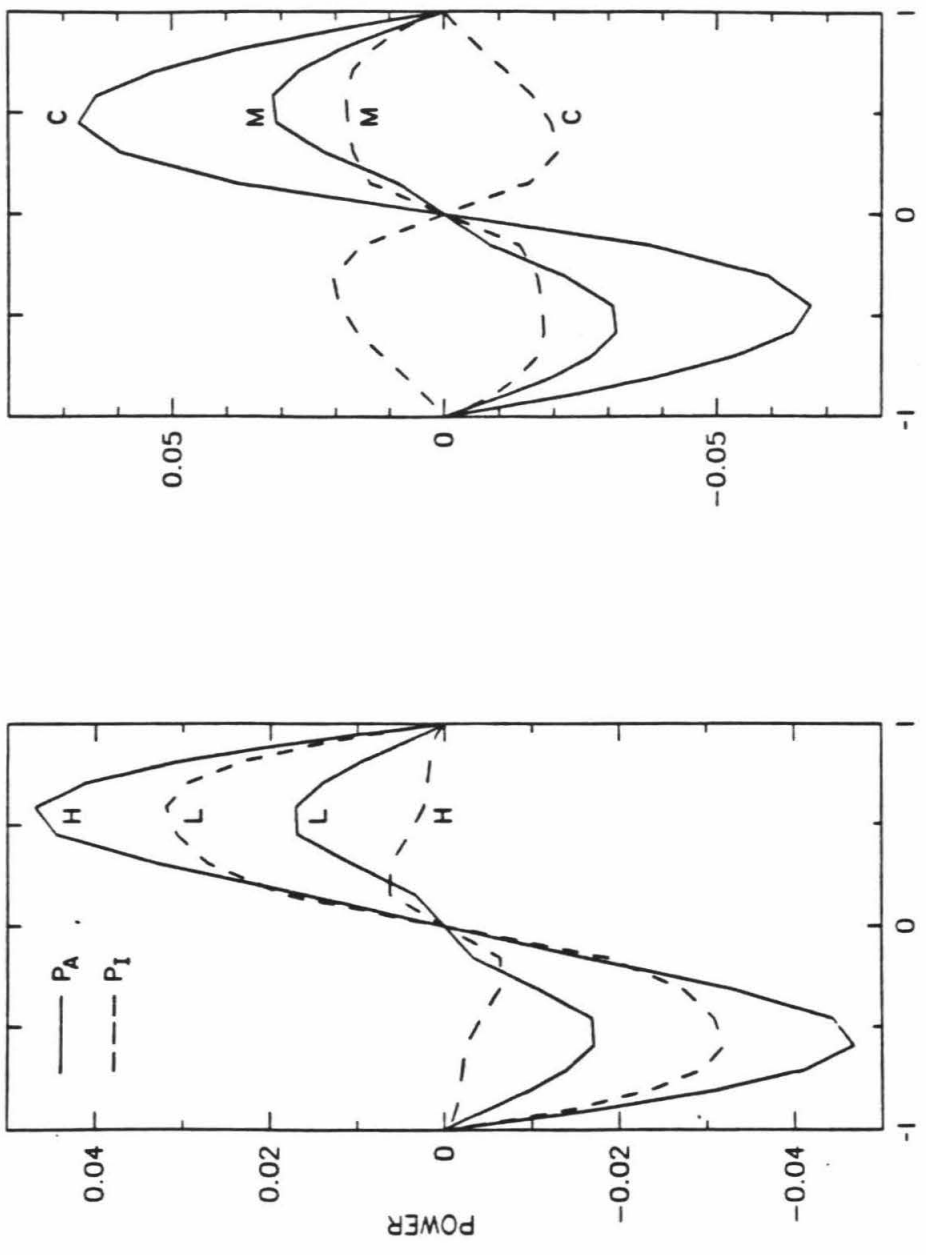
0.04
0.02
0
−0.02
−0.04
POWER
P_A
P_I
H
L
L
H
-1
0
1
SIN LATITUDE
0.05
0
−0.05
C
M
M
C
-1
0
1

Model C places the peak of the solar heating at the same level as model M, but the heating is concentrated into a narrower range of altitude (Fig. 3-2). The effect on the annual-average meridional energy balance is shown in the lower left and right panels of Fig. 3-11, where the results for profiles M and C, respectively, are compared. The dynamical heating in case C is more prominent than in case M, and the internal flux for C is lowest at the equator and highest at mid-latitudes. The results for model C, in fact, have characteristics similar to the E=1.10 case for solar heating model M (see Fig. 3-9). In Fig. 3-12b is shown the annual-average meridional power transported by the atmosphere and interior for models M and C, for E=1.37. It will be noticed that for C the heat transport in the interior is poleward, in the opposite direction from the heat transport in the atmosphere. Poleward transport of heat in the interior is found to occur as well at low latitudes for the E=1.10 case of solar heating model M (see Fig. 3-10). We conclude that concentrating the solar heating into a narrower range of altitude favors meridional transport by the atmosphere over the interior, and it can even cause the transport of heat in the interior to be poleward.

It should be mentioned here that the relationship between the value of E and the interior potential temperature for a given model depends on the profile assumed

for the solar heating. For example, for runs having the same value of E, E=1.37, θ_0=253.9 for profile H, while θ_0=269.4 for profile L. This fact is of secondary importance to the meridional energy balance, but it is relevant to understanding the detailed thermal structure of the atmosphere.

5. Seasonal Thermal Structure

In addition to the meridional energy balance, the model also calculates the seasonal thermal structure of Uranus' atmosphere. The effective temperature predicted for the north pole, equator, and south pole, for E=1.10, are plotted against the orbital phase L_S in Figure 3-13. Solar heating model M was assumed for the vertical deposition of sunlight. For E=1.10, the peak-to-peak amplitude of the seasonal effective temperature variation at the poles is ~2.5 K. This amplitude decreases steadily toward low latitudes to a value of only ~0.2 K at the equator. The size of the seasonal variations shows a slight decrease when E is increased. For E=1.33, the amplitude has decreased at the poles to 2.3 K, while for E=4.85, it is 1.2 K. (The current upper limit on E is $E \leqslant 1.27$ [Pollack et. al., 1986]. We have offered the seasonal amplitudes for higher values of E only to illustrate their relative insensitivity to E.)

Figure 3-13. Effective temperature vs. orbital phase L_S for north pole (N), south pole (S), and equator (E), for the case E=1.10. Solar heating model M was assumed. The amplitude of the seasonal variation decreases slowly with increasing E. "VE" marks the orbital phase appropiate to the Voyager 2 encounter with Uranus.

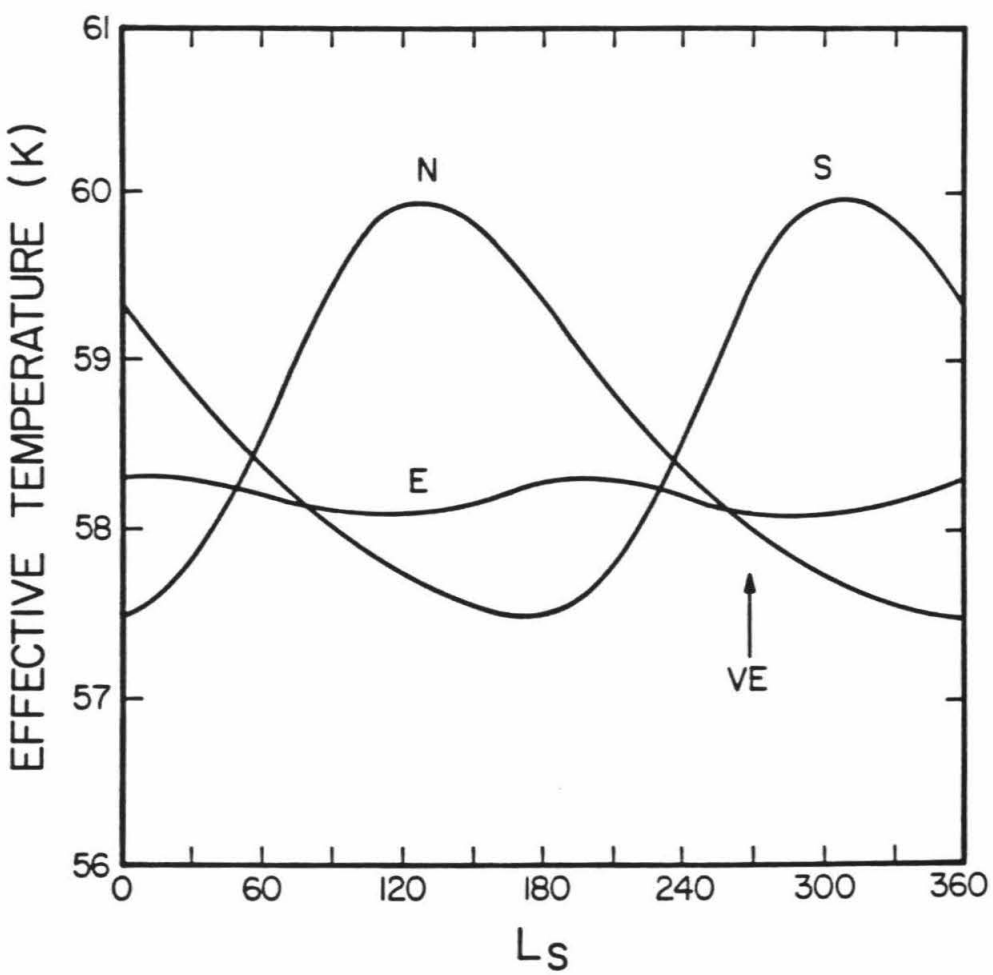
EFFECTIVE TEMPERATURE (K)
61
60
59
58
57
56
N
S
E
VE
0
60
120
180
240
300
360
Ls

At the time of the Voyager 2 encounter with Uranus, the southern hemisphere was very near summer solstice. This time corresponds to L_S=270. Fig. 3-13 shows that our model predicts the effective temperature at this time should be ~1.5 K higher at the south (sunlit) pole than at the equator, and the effective temperature at the equator should be only ~0.1 K higher than at the north pole. In contrast, Wallace's (1983) seasonal model predicted that at summer solstice the effective temperatures at the poles would be the same to within ~1 K, but both would be warmer by ~6 K than the equator. The difference between Wallace (1983) and the present results lies in our inclusion of meridional heat transport. This serves to keep temperature contrasts below ~2.5 K in the Uranian atmosphere.

In Figure 3-14 is shown the 225 cm^{-1} brightness temperature vs. latitude obtained by the Voyager 2 IRIS experiment (Hanel et. al., 1986), together with two synthetic curves, corresponding to E=1.10 and E=1.23, produced using solar heating model M. All of these curves correspond to an orbital phase L_S=270. The 225 cm^{-1} brightness temperature corresponds essentially to a weighted mean of the 450-900 mbar temperatures in the Uranus atmosphere. The synthetic curves reproduce the correct overall size of the ~2 K temperature contrasts seen in the data, but they clearly fail to yield the sharp minima seen at mid-latitudes. Both of the synthetic curves show a

Figure 3-14. The 225 cm^{-1} brightness temperature vs. latitude obtained by Hanel et. al. (1986) (thin line), and two synthetic curves produced by the model (heavy lines). The lower synthetic curve corresponds to E=1.10, the upper one to E=1.23. All three curves correspond to orbital phase L_S=270.

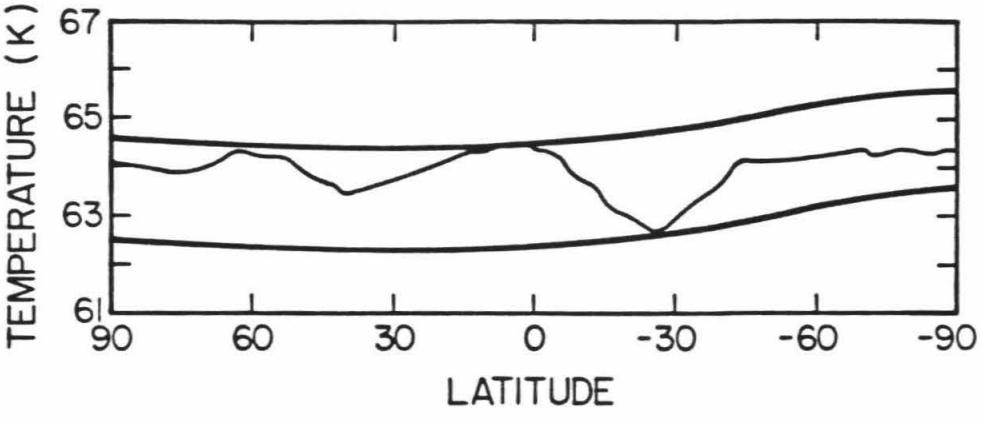
TEMPERATURE (K)
67
65
63
61
90
60
30
0
-30
-60
-90
LATITUDE

shallow minimum in the temperature at ~45 in the dark hemisphere, but these minima are not nearly as sharp as that inferred from the IRIS observations. In both synthetic curves, the south pole is warmer than the equator by 1.2 K, and the north pole is warmer than the equator by 0.2 K.

Model temperature profiles of the north and south poles, for L_S=270, are presented in Figure 3-15, along with the temperature retrievals produced by Hanel et al. (1986). Below 200 mbar, the E=1.10 case is seen to yield temperatures slightly too cool, and the E=1.23 case temperatures slightly too warm, relative to Hanel et al. It will be recalled, however, that E is varied here by varying the internal potential temperature θ_0 while holding the albedo at a fixed value of 0.35. This procedure leads to some ambiguity in the relationship between the parameter E and a given temperature profile. For instance, the temperature profile for the case E=1.23 shown in Fig. 3-15 could be brought into better agreement with the Hanel et al. profile, if θ_0 were decreased and the albedo increased in a manner that keeps E fixed. A lower value of θ_0 would imply cooler temperatures and thus better agreement with the Hanel et al. result. Due to this ambiguity, it is not useful here to compare in detail the temperature difference between our model profiles and the Hanel et al. profile. Instead, the purpose of Fig. 3-15 is to offer a comparison

between the shapes of the profiles, and to compare north pole-south pole temperature differences in the model to north-south differences in the Hanel et al. temperature retrievals. These latter two features of the model temperature profiles are fairly insensitive to E, and thus unambiguous comparisons can be made between the model profiles and the data. The model temperature differences between north and south poles are larger than the differences inferred from the data. It is interesting to note as well that the model temperature profile for the south pole does not have the deep temperature minimum at 80 mbar, which appears in the temperature retrieval of Hanel et al.

Figure 3-15. Model temperature profiles for north and south poles (heavy solid lines), together with the north (dotted line) and south (thin solid line) polar temperature retrievals of Hanel et al. (1986). Solar heating model M has been assumed for the model. The model temperature profiles in (a) correspond to E=1.10, and to E=1.23 in (b).

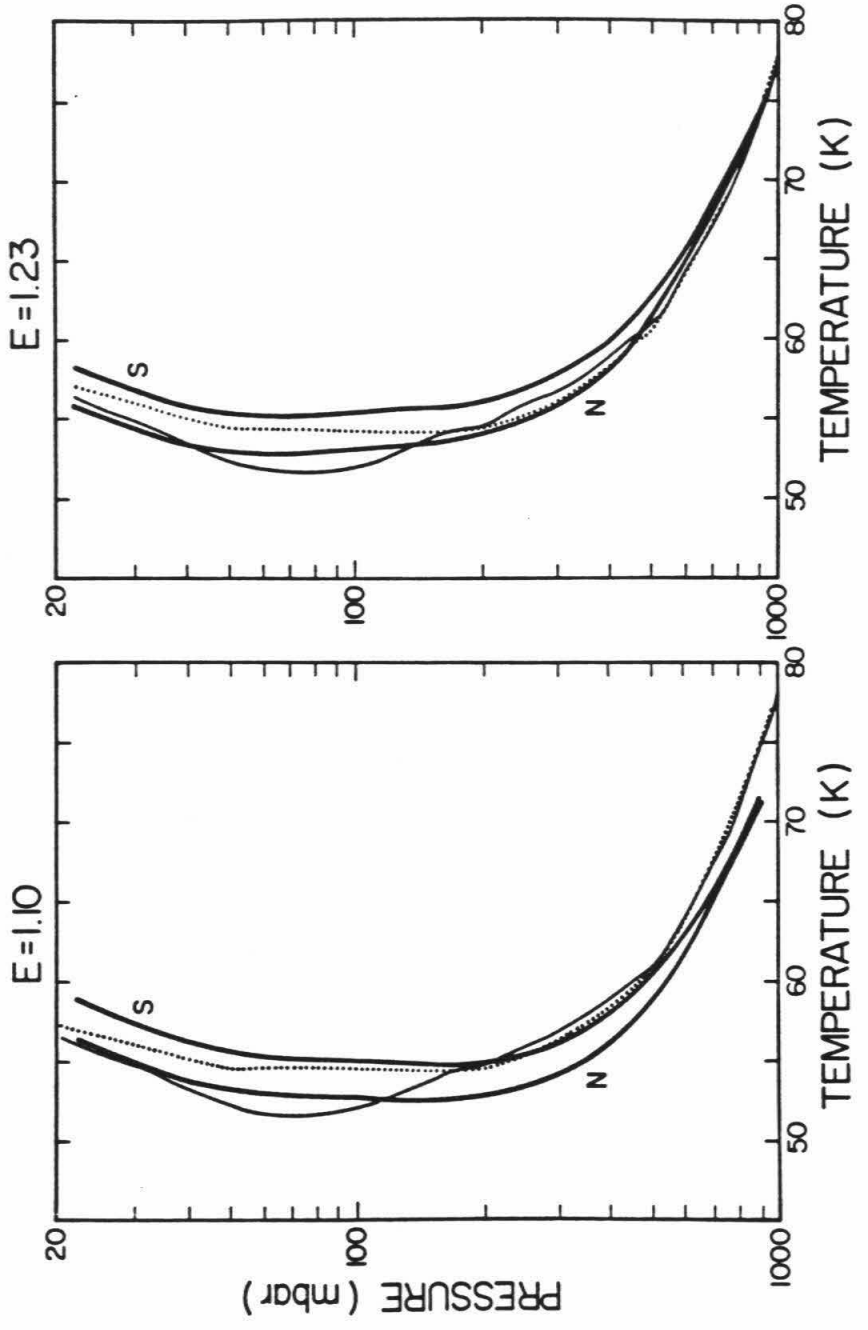
E=1.10
E=1.23
S
N
S
N
PRESSURE (mbar)
20
100
1000
50
60
70
80
TEMPERATURE (K)
TEMPERATURE (K)

6. Summary and Conclusions

We have investigated the seasonal meridional energy balance of the atmosphere of Uranus using a radiative-convective-dynamical model. The thermal balance has been studied for a wide range of internal heat source (i.e., for a wide range of E), and for four different models for the transmission of sunlight. Cases where the value of E exceeds the current upper limit of 1.27 (Pollack et al., 1986) have been included to better illustrate the behavior of the internal heat on Uranus and how it differs from that on the other Jovian planets.

On a seasonal basis, the meridional energy balance exhibits a bimodal nature. Energy conservation is satisfied in different ways in each of two regimes. In the terrestrial regime, meridional variations in the net (infrared minus solar) irradiance leaving the atmosphere are balanced by corresponding changes in the sum of the enthalpy storage rate and dynamical heating. The internal flux remains constant with latitude. In the jovian regime, the meridional variation of the net irradiance is balanced for the most part by corresponding changes in the internal flux. The enthalpy storage rate becomes quite small in the jovian regime.

Since the internal flux is generally much larger in the jovian regime than in the terrestrial regime, features

associated with unstable convective activity might be more prevalent at those latitudes which are in the jovian regime at the time of observation. The solstices are the worst time to look for evidence of a jovian regime on Uranus, since at these times it would be predominantly in the dark hemisphere. The best time is at or just before an equinox, when both hemispheres are sunlit and the two regimes are expected to be situated in separate hemispheres (see Figs. 3-3 through 3-5, L_S=0). It should be emphasized, however, that there is no clear reason to assume that the terrestrial or jovian regime could be detected by its visual appearance.

On an annual-average basis, Uranus receives excess heat at its poles and emits excess heat at the equator. As a requirement of energy conservation, there must be a net equatorward transport of heat in the atmosphere, interior, or both. In this study, it is found that, for a weak internal heat source ($E \lesssim 1.10$), the meridional heat transport occurs predominantly in the atmosphere. For a very strong internal heat source (E~4.85, far higher than the current upper limit on E), the heat would be transported almost entirely by the convective interior. For a moderate internal heat source lying between these extremes, the burden of heat transfer is shared by the atmosphere and interior, the amount shared by each depending on the value of E.

The amount of heat transported by the atmosphere or interior also depends on the vertical profile of solar heating. For a given value of E, depositing the solar energy at high altitudes and/or over a narrow range of altitude favors transport by the atmosphere. Deep penetration of sunlight favors transport by the interior.

As stated previously, the current upper limit on E for Uranus is $E \leq 1.27$. The results presented in Sections 3 and 4 indicate that most of the meridional heat transport should therefore occur in the atmosphere, although, if E is actually near its upper limit, as much as 1/3 of the heat transport at mid-latitudes could occur in the interior. The heat transport in the interior could be comparable to, or greater than, that in the atmosphere, only if most of the sunlight penetrates to pressure levels greater than ~3 bar.

An interesting, although admittedly speculative, conclusion may be drawn from the above remarks. In an effort to explain the high degree of axisymmetry seen in the global wind patterns of Jupiter and Saturn, Ingersoll (1976) proposed that the internal heat varied with latitude in such a way as to compensate for the latitudinal variation of the incident solar flux, so that the sum of internal and solar heating would be the same at each latitude. This would eliminate the differential heating that would otherwise drive meridional motions, and as a result Jupiter and Saturn would appear axisymmetric. The present results show that

the internal heat on Uranus should not behave in the manner proposed for Jupiter and Saturn, yet Uranus is observed to have a predominantly zonal circulation reminiscent of those planets (Smith et al., 1986). This suggests that meridional heat transfer by atmospheric eddies does not prevent axisymmetric, zonal circulations on the Jovian planets.

The model predicts that dynamical heat transport by the atmosphere should be effective in reducing meridional contrasts in the effective temperature. We find that the effective temperature at the south (sunlit) pole at the time of the Voyager 2 encounter should have been ~1.5 K warmer than at the equator. The equatorial effective temperature should have been ~0.2 K warmer than the effective temperature at the north pole. These temperature differences are well below the ~6 K contrasts predicted using a 1-dimensional radiative-convective model (Wallace, 1983). The present model does not reproduce the cold minimum in the 450-900 mbar temperatures seen at -30°S in the IRIS data. This feature and some other details of the IRIS data could be due to dynamical processes that are inadequately treated by mixing length theory or could possibly be due to latent heat effects (Smith et al., 1986).

The other Jovian planets differ from Uranus in radius, obliquity, radiative time constant, and E. Any or all of

these parameters are potentially important in determining the nature of the meridional energy balance. Examining the character of the energy balance for a broad range of these parameters will be the subject of future work.

Acknowledgements.

This research was supported by NASA grant NAGW 58 and Voyager funds from the Jet Propulsion Laboratory to the California Institute of Technology.

References

BRIGGS, F.H., AND B.H. ANDREW (1980). Microwave radiometry and interferometry of Uranus. Icarus 41, 269-277.

CHANDRASEKHAR, S. (1960). Radiative Transfer. Dover Publications, New York.

COHEN, E.R., L. FROMMHOLD, AND G. BIRNBAUM (1982). Analysis of the far infrared H_2-He spectrum. J. Chem. Phys. 77, 4933-4941.

CONRATH, B. J., P. J. GIERASCH, AND N. NATH (1981). Stability of zonal flows on Jupiter. Icarus 48, 256-282.

CONRATH, B., AND P.J. GIERASCH (1984). Global variation of the para hydrogen fraction in Jupiter's atmosphere and implications for dynamics on the outer planets. Icarus 57, 184-204.

DANIELSON, R. E., W. D. COCHRAN, P. G. WANNIER, AND E. S. LIGHT (1977). A saturation model of the atmosphere of Uranus. Icarus 31, 97-109.

DORE, P., L. NENCINI, AND G. BIRNBAUM (1983). Far infrared absorption in normal H_2 from 77 to 298 K. J. Quant. Spectrosc. Radiat. Transfer 30, 245-253.

EADY, E.T. (1949). Long waves and cyclone waves. Tellus 1, 33-52.

HANEL, R., B. CONRATH, F. M. FLASAR, V. KUNDE, W. MAGUIRE, J. PEARL, J. PIRRAGLIA, R. SAMUELSON, D. CRUIKSHANK, D. GAUTIER, P. GIERASCH, L. HORN, AND P. SCHULTE (1986). Infrared observations of the Uranian system. Science 233, 70-74.

HELD, I. M. (1978). The vertical scale of an unstable baroclinic wave and its importance for eddy heat flux parameterizations. J. Atmos. Sci. 35, 572-576.

INGERSOLL, A.P. (1976). Pioneer 10 and 11 observations and the dynamics of Jupiter's atmosphere. Icarus 29, 245-253.

INGERSOLL, A.P. (1984). Atmospheric dynamics of Uranus and Neptune: Theoretical considerations. In Uranus and Neptune (J.T. Bergstralh, Ed.), pp. 263-269. NASA Conference Publication 2330.

INGERSOLL, A.P., AND C.C. PORCO (1978). Solar heating and internal heat on Jupiter. Icarus 35, 27-43.

MANABE, S., AND R.T. WETHERALD (1967). Thermal equilibrium of the atmosphere with a given distribution of relative humidity. J. Atmos. Sci. 24, 241-259.

POLLACK, J. B., K. RAGES, K. H. BAINES, J. T. BERGSTRALH, D. WENKERT, AND G. E. DANIELSON (1986). Estimates of the bolometric albedos and radiation balance of Uranus and Neptune. Submitted to Icarus

SMITH, B. A., L. A. SODERBLOM, R. BEEBE, D. BLISS, J. M. BOYCE, A. BRAHIC, G. A. BRIGGS, R. H. BROWN, S. A. COLLINS, A. F. COOK II, S. K. CROFT, J. N. CUZZI, G. E. DANIELSON, M. E. DAVIES, T. E. DOWLING, D. GODFREY, C. J. HANSEN, C. HARRIS, G. E. HUNT, A. P. INGERSOLL, T. V. JOHNSON, R. J. KRAUSS, H. MASURSKY, D. MORRISON, T. OWEN, J. PLESCIA, J. B. POLLACK, C. C. PORCO, K. RAGES, C. SAGAN, E. M. SHOEMAKER, L. A. SROMOVSKY, C. STOKER, R. G. STROM, V. E. SUOMI, S. P. SYNNOTT, R. J. TERRILE, P. THOMAS, W. R. THOMPSON, AND J. VEVERKA (1986). Voyager 2 in the Uranian system: Imaging Science results. Science **233**, 43-64.

STONE, P.H. (1972). A simplified radiative-dynamical model for the static stability of rotating atmospheres. J. Atmos. Sci. **29**, 405-418.

STONE, P.H. (1974). The meridional variation of the eddy heat fluxes by baroclinic waves and their parameterization. J. Atmos. Sci. **31**, 444- 456.

STONE, P. H. (1976). The meteorology of the Jovian atmosphere. In Jupiter, (T. Gehrels, Ed.), pp. 586-618. Univ. of Arizona Press, Tucson.

TRAFTON, L. (1967). Model atmospheres of the major planets. Astrophys. J. **147**, 765-781.

WALLACE, J. M. AND P. V. HOBBS (1977). Atmospheric Science. Academic Press, New York.

WALLACE, L. (1980). The structure of the Uranus atmosphere. Icarus 43, 231- 259.

WALLACE, L. (1983). The seasonal variation of the thermal structure of the atmosphere of Uranus. Icarus 54, 110-132.

Chapter 4

QUESTIONS FOR THE FUTURE

In the previous chapters, a two-dimensional radiative-convective-dynamical model has been presented which calculates the seasonal and annual-average thermal behavior of the atmosphere of Uranus. Heat transport in the model can occur through radiative transfer, small-scale convection, or through dynamical heat transfer by baroclinic eddies. Radiative heat transfer and small-scale convection are treated in a manner similar to conventional radiative-convective models for thin-atmosphere planets (Manabe and Wetherald, 1967). Dynamical heat transport by baroclinic eddies is calculated using a mixing-length formulation for sloping convection (Stone, 1972; Ingersoll and Porco, 1978). The deep atmosphere and interior are assumed to be adiabatic, with a single value of potential temperature at all latitudes. Convection is assumed always to carry heat upward, never downward. Possible thermal effects due to the presence of condensible constituents, such as methane, or due to ortho-para hydrogen conversion (Conrath and Gierasch, 1984), have been ignored.

The results of the model under the above assumptions indicate that the internal heat flux varies seasonally. The intense solar heating in the sunlit hemisphere during the

solstices inhibits the internal flux in that hemisphere. The large excess of infrared cooling in the dark hemisphere causes the internal flux to be large during the winter. Meridional heat transport by baroclinic eddies occurs at all times during the year, but it is strongest during the summer. On an annual-average basis, both the atmosphere and interior participate in the meridional heat transport. The ratio of power transported across a given latitude by convection in the interior to that by baroclinic eddies in the atmosphere is predicted by the model and is found to depend on the strength of the internal heat source and on the altitude profile of solar heating. For a given solar heating profile, a weak internal heat source favors heat transport in the atmosphere, on an annual average, while a strong internal heat source promotes heat transport in the interior. The validity of the value predicted for this ratio is subject to the crude treatment of dynamical heat fluxes in the model.

The formulation for the dynamical heat fluxes is based on a linear theory for the baroclinic instability of a zonal thermal wind. Since the theory is linear, it does not put any constraint on the amplitude of growing unstable modes. Instead, it is simply assumed that the exponential growth of these modes is limited by non-linear effects. Stone (1972) assumed that the velocity of the eddies grows until it is of the same magnitude as the zonal thermal wind difference

across one scale height. This assumption has been incorporated into the radiative-convective-dynamical model. It appears to work fairly well for the Earth's atmosphere at mid-latitudes (Stone, 1972) where the eddies have about the same velocity as the zonal thermal wind. It might not be a good assumption, however, for planets with deep atmospheres, where atmospheric motions might conceivably extend over many scale heights. Predicting the amplitude to which baroclinic instabilities can grow in a deep atmosphere remains an important unsolved problem in planetary meteorology.

Using the above assumption concerning the amplitude of baroclinic eddies, the model predicts that the eddies on Uranus should have typical velocities of ~1 m/s and a dominant length scale of ~1600 km. For comparison, by using radiative-dynamical scaling arguments, Stone (1973) predicted eddy velocities of ~1 m/s and an eddy length scale of ~600 km. If appreciable motions in the atmosphere of Uranus are confined to a thin layer of depth of ~1 scale height, and the mean zonal wind at the bottom of the layer is zero, then Stone's assumption implies that the velocity of the eddies should be comparable to the average velocity of the mean zonal wind in the layer. This forms the basis for Stone's (1973) prediction that Uranus' appearance would be dominated by non-axisymmetric features, similar to the swirling cloud patterns seen at middle latitudes on the Earth.

Voyager 2 images of the cloud patterns in the atmosphere of Uranus (Smith et al., 1986) reveal a predominantly zonal circulation, far more reminiscent of Jupiter and Saturn than of the Earth. The eddies which were expected by Stone to lend a non-axisymmetric appearance to the planet are not readily apparent in the images. The radiative-convective-dynamical model predicts that meridional heat transport by eddies in the visible atmosphere should have been occurring in the sunlit hemisphere during the time the observations were made. Hence, the lack of visible eddies in the images could be seen as a failure on the part of the model to predict the correct dynamical mode of heat transport. At least two possible explanations can be offered for the disagreement between the theoretically predicted appearance of Uranus and the appearance seen in the Voyager images.

One possible explanation is that baroclinic eddies with velocities of order 1 m/s are actually present in the visible atmosphere but are completely obscured by the much greater zonal winds measured by the Voyager 2 camera. The minimum zonal wind velocity measured is 40 m/s, and at some latitudes the zonal wind is found to exceed 100 m/s (Smith et al., 1986). If the eddies have velocities of only ~1 m/s, it should not be a surprise that Uranus has an axisymmetric appearance. At first, this argument may seem to violate the original assumption that the velocity of the eddies should be comparable to the mean zonal wind. But

this assumption applies strictly only to the baroclinic component of the zonal wind, i.e., that component which has a non-vanishing vertical shear given by the thermal wind equation. A relatively large barotropic component (i.e., a component with no vertical shear) can be superimposed on the baroclinic component without violating the thermal wind equation. It is possible that the large, $\geq$ 40 m sec^{-1} zonal winds measured by Voyager 2 Imaging Science correspond chiefly to a large barotropic component, while the baroclinic component amounts to no more than a few meters per second. If so, then according to the original assumption the eddy velocity would be ~1 m/s, comparable to the baroclinic component of the zonal wind. The eddies would be somewhat hidden by the much larger barotropic component of the zonal wind. The existence of a dominant barotropic component would imply that the zonal winds extend deep into the atmosphere of Uranus (Smith et al., 1986).

An alternative explanation for the zonal symmetry of Uranus is that baroclinic eddies simply are not present. Theoretical calculations of the stability of zonal flows on Jovian planets (Gierasch et al., 1979; Conrath et al., 1981) indicate that baroclinic instability is strongly suppressed by the presence of a deep atmosphere and fluid interior. If this is the case for Uranus, then some dynamical mechanism other than baroclinic instability must be responsible for maintaining the small horizontal temperature contrasts

measured by the Voyager 2 IRIS experiment (Hanel et al., 1986).

Hanel et al. (1986) find the 400-900 mbar mean temperature to have local minima occurring at 25°S and 40°N latitude. Such a meridional temperature structure, with local minima occurring at mid-latitudes simultaneously in both hemispheres, is not produced by the radiative-convective-dynamical model. Perhaps these cold areas provide an important clue about the mechanism that transports heat in the atmosphere. On the other hand, it is possible that they might be only the signature of a more localized dynamical or dynamical-latent heat effect.

Voyager 2 Radio Science (Tyler et al., 1986) have found a preliminary value of 2% for the methane mixing ratio in the deep atmosphere. The presence of so much methane could have important consequences for the dynamics and for the meridional heat budget. Smith et al. (1986) point out that the latent heat release associated with 2% methane in the atmosphere could produce temperature changes of 6 or 7 K. For comparison, the temperature contrasts measured by IRIS (Hanel et al., 1986) for the region between 400-900 mbar amount to only ~2 K. In addition, Smith et al. argue that the orientation of plume tails in the images and the evidence for positive (eastward) zonal winds relative to the interior both suggest that the eastward zonal velocity at mid-latitudes increases with altitude. They note that the

sense of this vertical shear is opposite that predicted by the thermal wind equation, if meridional density gradients on constant pressure surfaces are due solely to temperature variations in an atmosphere with uniform composition. It is suggested by Smith et al. that the sign of the vertical shear might be explained if the density variations are the result of an atmosphere with a meridionally variable composition (due to, for instance, methane condensation), which might overwhelm the effect of the temperature variations on the density. This suggestion might have some interesting consequences for the dynamics. In particular, it is conceivable that baroclinicity (i.e., variations of density along constant pressure surfaces), induced by a variable composition, could drive a dynamical regime that is distinct from any predicted for atmospheres with uniform composition. Some calculations should be done to understand the properties of baroclinic instabilities in an atmosphere with variable composition.

Meridional inhomogeneity of the ammonia mixing ratio has been invoked in an attempt to explain the seasonal variability of microwave brightness temperatures on Uranus (Briggs and Andrew, 1980). Although some thought has been given to this problem in the context of the radiative-convective-dynamical model, no plausible mechanism has been found that will produce a lateral variation in the ammonia mixing ratio.

Up to this point, a number of unsolved problems concerning the dynamics and the meridional energy balance of the atmosphere of Uranus have been identified: Are baroclinic eddies primarily responsible for transporting heat meridionally in the visible atmosphere? If so, then have the heat fluxes due to these eddies been correctly treated by the model? If baroclinic instability is not the dynamical mechanism that transports heat in the atmosphere, then what is? Why do the minima in the 400-900 mbar mean temperatures occur at mid-latitudes, and why does the equator appear to be as warm as the poles (Hanel et al., 1986)? What role might the condensation of methane play in the dynamics and in the meridional energy balance?

Continuing analysis of the wealth of data collected by Voyager 2 at Uranus combined with theoretical analysis should be instrumental in placing tighter constraints on competing models for Uranus' dynamics and meridional energy balance. The radio occultation data and IRIS data together should yield the vertical temperature structure at several latitudes. Voyager 2 photometry at low and high phase angles (Pollack et al., 1986; Smith et al., 1986) should produce a better estimate for the bolometric bond albedo. IRIS should be able to provide a better number for the power emitted by Uranus at the encounter time. Together these measurements should put tighter limits on the value of the internal heat source of Uranus. Analysis of the effective

temperature at a number of latitudes by IRIS, and of IRIS radiometer measurements of the broad-band visible reflected sunlight, will provide valuable information on the meridional radiation budget. Knowledge of this budget is essential to relating the thermal structure observed at encounter time to the seasonal meridional energy balance. Prospects seem good that at least some of the questions posed in this chapter will eventually be answered through continued application and refinement of the radiative-convective-dynamical model, but only if it is supplemented by progress in our theoretical understanding of the various mechanisms that can transport heat in Jovian atmospheres.

References

BRIGGS, F.H., AND B.H. ANDREW (1980). Microwave radiometry and interferometry of Uranus. Icarus 41, 269-277.

CONRATH, B. J., P. J. GIERASCH, AND N. NATH (1981). Stability of zonal flows on Jupiter. Icarus 48, 256-282.

CONRATH, B., AND P. J. GIERASCH (1984). Global variation of the para hydrogen fraction in Jupiter's atmosphere and implications for dynamics on the outer planets. Icarus 57, 184-204.

GIERASCH, P. J., A. P. INGERSOLL, AND D. POLLARD (1979). Baroclinic instabilities in Jupiter's zonal flow. Icarus 40, 205-212.

HANEL, R., B. CONRATH, F. M. FLASAR, V. KUNDE, W. MAGUIRE, J. PEARL, J. PIRRAGLIA, R. SAMUELSON, D. CRUIKSHANK, D. GAUTIER, P. GIERASCH, L. HORN, AND P. SCHULTE (1986). Infrared observations of the Uranian system. Science 233, 70-74.

INGERSOLL, A. P., AND C. C. PORCO (1978). Solar heating and internal heat on Jupiter. Icarus 35, 27-43.

MANABE, S., AND R.T. WETHERALD (1967). Thermal equilibrium of the atmosphere with a given distribution of relative humidity. J. Atmos. Sci. 24, 241-259.

POLLACK, J. B., K. RAGES, K. H. BAINES, J. T. BERGSTRALH, D. WENKERT, AND G. E. DANIELSON (1986). Estimates of the

bolometric albedos and radiation balance of Uranus and Neptune. Submitted to Icarus

SMITH, B. A., L. A. SODERBLOM, R. BEEBE, D. BLISS, J. M. BOYCE, A. BRAHIC, G. A. BRIGGS, R. H. BROWN, S. A. COLLINS, A. F. COOK II, S. K. CROFT, J. N. CUZZI, G. E. DANIELSON, M. E. DAVIES, T. E. DOWLING, D. GODFREY, C. J. HANSEN, C. HARRIS, G. E. HUNT, A. P. INGERSOLL, T. V. JOHNSON, R. J. KRAUSS, H. MASURSKY, D. MORRISON, T. OWEN, J. PLESCIA, J. B. POLLACK, C. C. PORCO, K. RAGES, C. SAGAN, E. M. SHOEMAKER, L. A. SROMOVSKY, C. STOKER, R. G. STROM, V. E. SUOMI, S. P. SYNNOTT, R. J. TERRILE, P. THOMAS, W. R. THOMPSON, AND J. VEVERKA (1986). Voyager 2 in the Uranian system: Imaging Science results. Science **233**, 43-64.

STONE, P.H. (1972). A simplified radiative-dynamical model for the static stability of rotating atmospheres. J. Atmos. Sci. **29**, 405-418.

STONE, P.H. (1973). The dynamics of the atmospheres of the major planets. Space Sci. Rev. **14**, 444-459.

TYLER, G. L., D. N. SWEETNAM, J. D. ANDERSON, J. K. CAMPBELL, V. R. ESHLEMAN, D. P. HINSON, G. S. LEVY, G. F. LINDAL, E. A. MAROUF, AND R. A. SIMPSON (1986). Radio science observations of the Uranian system with Voyager 2: Properties of the atmosphere, rings, and satellites. Science **233**, 79-84.

PART II. Viscosity of Rock-Ice Mixtures and Applications to the Evolution of Icy Satellites

A.J. Friedson and D.J. Stevenson

Division of Geological and Planetary Sciences
California Institute of Technology
Pasadena, California 91125

Published in Icarus
56, 1-14 (1983)

Contribution number 3868 of the Division of Geological and Planetary Sciences, California Institute of Technology, Pasadena, California 91125.

Abstract

Theory and experiments are used to establish lower and upper bounds on the ratio of actual viscosity to pure ice viscosity for a suspension of rock particles in a water ice matrix. For typical conditions encountered in icy satellites, this ratio is of order ten or possibly larger, depending on unknown factors such as the particle size distribution. It is shown that even this modest increase in viscosity may be enough to have caused a failure of solid state convective self-regulation early in the evolution of a homogeneous, rock- water ice satellite, provided the satellite is large enough and sufficiently silicate rich. The criteria for this failure are satisfied by Ganymede and are marginal for Callisto, if the silicates are hydrated. Failure of self-regulation means that the viscosity is too high for the interior to remain completely solid and eliminate the heat production of long-lived radioisotopes by solid state convection. Partial melting of the ice then occurs. It is further shown that satellites of this size may then undergo runaway differentiation into a rock core and almost pure ice mantle, because the gravitational energy release is sufficient to melt nearly all the ice and the Rayleigh-Taylor instability time scale is short. (Although the high pressure phases of ice melt, the resulting water quickly refreezes at a higher level.) We conjecture that

these results explain the striking surface dissimilarity of Ganymede and Callisto, if these satellites accreted cold and undifferentiated. Ganymede may have gone supercritical (melted and differentiated) because of a failure of self-regulation, whereas Callisto remained undifferentiated to the present day. Like all proposed explanations for the Ganymede-Callisto dichotomy, this conjecture cannot be quantified with confidence, because of inadequate or incomplete observations, theory and experimental data.

1. Introduction

Early work on large icy satellites such as Ganymede and Callisto (Lewis, 1971; Consolmagno and Lewis, 1976) proposed internal structures consisting of a rock core, a liquid water mantle and a thin ice crust. These models arose naturally from a consideration of evolutions in which only a conductive heat transport is allowed in the solid media. Reynolds and Cassen (1979) showed, however, that allowance for the low viscosity of water ice implied a rapid freezing of any liquid water mantle and a subsolidus, convective steady state. Subsequent models of icy satellites (Parmentier and Head, 1979; Thurber et al., 1980; Cassen et al., 1980; Schubert et al., 1981) have all invoked vigorous thermal convection in solid icy interiors. It has been inferred from this work that the radiogenic heating from long-lived radioisotopes (primarily ^{40}K, ^{238}U and ^{232}Th) would be insufficient by itself to cause melting of the ice within a satellite that contains only silicates and water ice. (The argument does not extend to satellites containing more volatile ices such as ammonia.) The essential idea is that the thermal state of the satellite is "self-regulated" (Tozer, 1965) because of the extreme temperature dependence of the ice viscosity, and stabilizes at a subsolidus state for which the ice viscosity is low enough and the convection is vigorous enough that the radiogenic heat can be

eliminated. According to this view, a homogeneously accreted rock-water ice satellite would not differentiate into a rock core and water ice mantle unless either the heating during accretion were enough to melt the ice (Schubert et al., 1981; Lunine and Stevenson, 1982) or the silicate inclusions were large enough (>0.1 km in radius) to settle out from the rock-ice matrix by Stokes flow.

These previous calculations have assumed the rheology of pure water ice. In this work, we consider the rheology of a rock-ice mixture and pose anew the question: Can radiogenic heating by itself cause internal melting and differentiation of a rock-water ice satellite? Our answer to this question is a conditional yes. This is not surprising by itself -- it is always possible to postulate a satellite that is large enough or rich enough in silicates that the ice would melt. Differentiation could then ensue by upward migration of melt water from the matrix and Rayleigh-Taylor instability of the silicate-rich residue (Schubert et al., 1981). The interesting conclusion, however, is that the critical state (delineating bodies that could remain undifferentiated forever from those that must differentiate) may be close to the actual states of Ganymede and Callisto. It is possible the larger, more silicate-rich body (Ganymede) went 'supercritical' (i.e. partially melted and differentiated) whereas the smaller, less silicate-rich body (Callisto) remained subcritical. This conjecture is only meaningful

for a model in which both satellites accreted cold and had initial (post-accretional) states of homogeneous water ice-rock mixtures. Although this is difficult to reconcile with accretional models suggesting melting for Ganymede at least (Schubert et al., 1981; Lanciano et al., 1981; Lunine and Stevenson, 1982), it cannot be excluded because accretional mechanics are poorly understood. As we elaborate below, the conjectured supercriticality of Ganymede and subcriticality of Callisto are a possible way of explaining the striking surface dissimilarities of these bodies.

It must be emphasized that no firm conclusions can be reached here because of quantitative inadequacies in the current understanding of convection, rheology and satellite interiors. The best we can do is revive and substantiate a possibility that many people (including the second author of this paper) had tended to discount: that self-regulation, as originally proposed for the Earth by Tozer, may have failed during the evolution of some icy satellites. Further work, especially experiments, will be needed to determine the importance of the possibilities considered here.

The rheological model for rock-ice mixtures is described in Section 2. The analysis is restricted to a suspension of silicate spheres in an ice matrix and bounds are established for the range of possible viscosity enhancements provided by the silicate spheres. In Section 3, a parameterized thermal convection model is described and used to determine a

criterion for criticality, defined as the heat flow and/or silicate volume fraction for which the satellite temperature profile intercepts the melting curve of water ice. In Section 4, the consequences of achieving this critical state are examined and it is shown that under certain circumstances, a 'runaway' differentiation can occur in which the silicates settle to form a core and extensive melting of water ice takes place, the latent heat being supplied by the gravitational energy of differentiation. A possible application of these results to Ganymede and Callisto is described. It is suggested that if Ganymede started cold but achieved criticality and subsequent runaway differentiation, then this might explain the resurfacing and inferred extensional tectonics. Quantification of this conjecture is difficult, however. Section 5 concludes with a summary of the results and their current limitations.

2. The Relative Viscosity of a Rock-Ice Mixture

Dense suspensions exist in a diversity of natural and industrial environments. Examples include cements, paints, fermentation broths, sewage sludges and animal feeds. The existing data base (briefly summarized by Cheng and Richmond, 1978) shows that these suspensions may behave viscously but can also exhibit a variety of non-viscous responses, loosely characterized as 'granulo-viscous' effects. These include stick-slip phenomena, dilatational effects, liquefaction and flocculation. We shall concentrate here on the viscous response, but we acknowledge that the non-viscous effects (which are poorly understood, in general) may play a role in icy satellites.

The mixture is modeled as a suspension in which the 'fluid' is water ice and the suspended particles are taken to be rigid spheres of silicate. It is initially assumed that the silicate particles are large enough that the surrounding water ice behaves as a viscous or effectively viscous continuum, yet small enough that their settling motion under the action of gravity can be ignored relative to the imposed straining motion of thermal convection. For a given silicate inclusion of diameter d, this implies that $0.1 \text{ cm} \lesssim d \lesssim 10^4$ cm, if the ice grain size is ~0.1 cm. We return at the end of the section to a discussion of these limits and the roles of particles which violate the limits.

A standard result of fluid mechanics is that the viscosity of a suspension is greater than that of the pure solvent. Physically, this effect is a consequence of the disturbance flow created by the presence of the particles immersed in the ambient fluid. The particles act to increase the straining motion of the fluid flow. In a Newtonian fluid, the energy dissipated is proportional to the square of the strain rate. Hence, the dissipation rate is greater in the suspension than in the pure fluid when both systems are subjected to the same stresses. If the suspension is sufficiently homogeneous, so that a single effective viscosity may be defined, then this effective viscosity is necessarily greater than that of the pure fluid. The ratio of the effective viscosity of the suspension to that of the pure fluid is often called the relative viscosity.

The problem of calculating the relative viscosity of a suspension was solved theoretically by Einstein in 1905 for the case of very dilute suspensions (Einstein, 1906). Einstein's solution showed that, for dilute suspensions, the relative viscosity is a function solely of the volume concentration of the particles in the suspension. The results of experiments on suspensions with higher particle volume fractions (Thomas, 1965) indicate that this property of the relative viscosity is retained to arbitrarily high

volume concentrations provided the particles have all the same size. In this case,

$$\eta_r = f(\phi) \qquad (1)$$

where η_r is the relative viscosity and ϕ is the particle volume concentration (i.e. the ratio of volume occupied by the particles to the total volume). Even in this idealized case of a single particle size, there is no adequate theoretical treatment of $f(\phi)$ for all ϕ, and there is rather poor agreement among different experimental investigations. Thomas (1965) was able to substantially reduce the scatter in the relative viscosity data by correcting for non-Newtonian, inertial, and non-homogeneous suspension effects. The empirical formula

$$\eta_r = 1 + 2.5\,\phi + 10.05\,\phi^2 + 0.00273\,e^{16.6\phi} \qquad (2)$$

was found to satisfactorily fit the reduced data. Clearly, it must fail at some critical value ϕ_c, where the suspended spheres "freeze" (i.e. form an interlocking matrix, the rheological properties of which depend on the rheology of the silicates). The value of ϕ_c is about 0.6. For our purposes, η_r is effectively infinite at $\phi > \phi_c$. (This critical value should not be confused with the critical state $\phi = \phi_{max}$ described in the next section.)

It is very unlikely that the silicate particles in an icy satellite are close to a single size. There are at least three different processes that determine the particle size distribution: condensation, coagulation and impact fragmentation. Condensation refers to the initial nucleation and diffusive growth of silicate particles from a gas phase, and might be expected to yield 0.1-1 μ particles. Coagulation refers to the sticking of condensates during sedimentation to a nebula mid-plane (Safronov, 1972) and might be expected to yield ~1 cm sized particles. Most or all memory of these lengthscales may be obliterated if the silicates are then assembled into bodies which are large enough that they undergo annealing, metamorphism or melting because of pressure and/or temperature. Impact fragmentation may be the most important size determining process. Experiments and observations (Hartmann, 1969; Fujiwara et al., 1977) suggest $n(m) \sim m^{-\alpha}$ with $0.6 \leq \alpha \leq 1.2$, where n(m) is the total number of fragments with mass greater than or equal to m. For a likely intermediate value of $\alpha = 1$, the cumulative mass ~ log m and has the property that each logarithmic interval of the mass or size distribution contributes equally to ϕ. In this case, a very broad size distribution is applicable to icy satellites.

Experiments (Eilers, 1941; Farris, 1968; Chong et al., 1971) indicate that the relative viscosity for a suspension containing a diversity of particle sizes is always less than

a suspension with the same volume concentration ϕ but a single particle size. Moshev (1979) suggests a simple generalized formula

$$\eta_r = \left(1 + \frac{0.75\ \phi/\phi_c}{1 - \phi/\phi_c} \right)^2 \qquad (3)$$

where the critical volume fraction ϕ_c is the only additional parameter and is naturally larger for a broad particle size distribution than the value ~0.6 appropriate for a single particle size. Although there is some experimental support for this expression (Chong et al., 1971), the evaluation of ϕ_c is difficult and there is no good theoretical reason to suppose that η_r depends only on ϕ and ϕ_c. In fact, ϕ_c should approach unity for a sufficiently diverse particle size distribution, but equation (3) then violates the absolute lower bound on η_r that Roscoe (1952) obtained by assuming that particles of different size do not hydrodynamically interact. This lower bound is

$$\eta_r(\text{min}) = (1 - \phi)^{-5/2} \qquad (4)$$

Figure 1 shows the predicted lower and upper bounds for the relative viscosity, implied by equations (2) and (4). The lower bound is probably nearer to the actual situation and is used in our analysis of convection in Section 3.

Figure 1: Relative viscosity vs. particle volume fraction, ϕ. a) Uniform-sized particles. The empirical formula due to Thomas breaks down near $\phi = 0.6$. b) Lower bound for the relative viscosity. The relative viscosity for any particle size distribution must lie between these two curves.

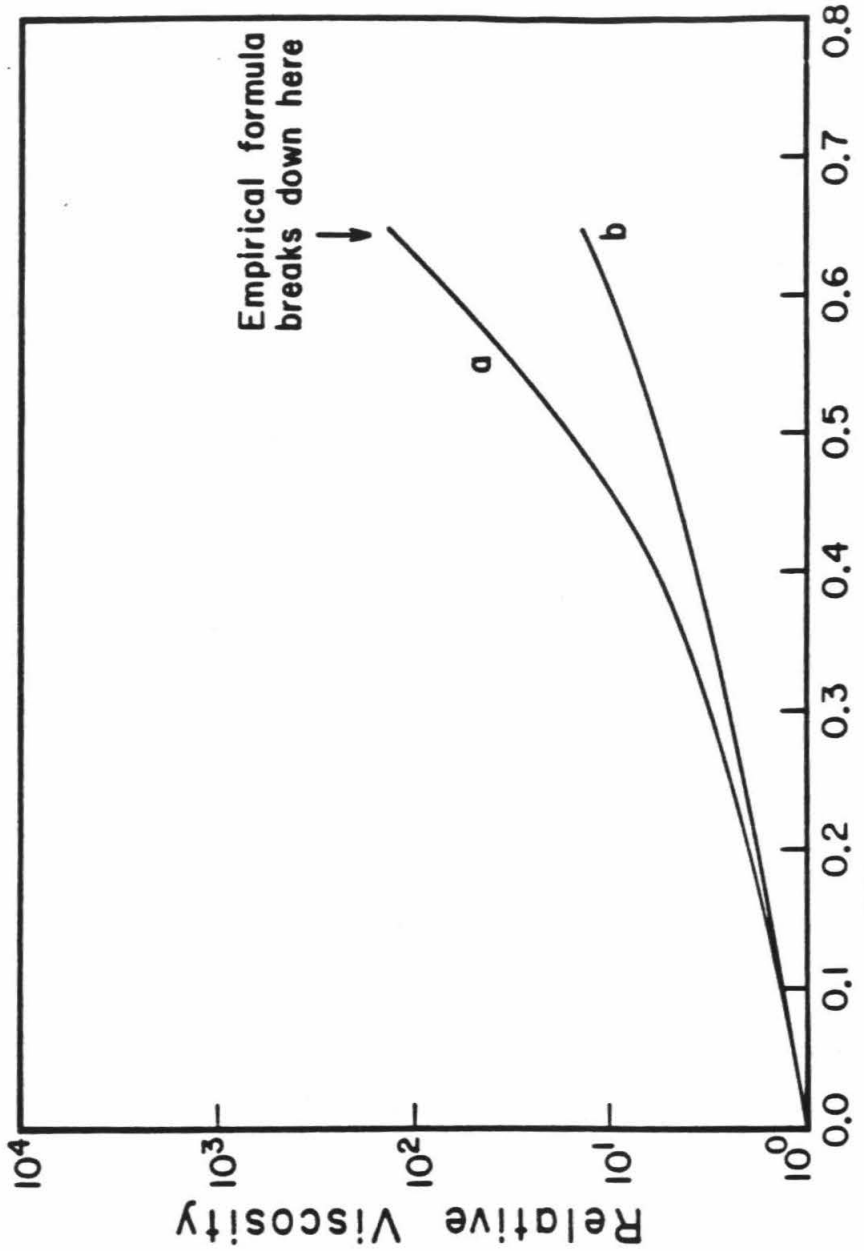
Empirical formula
breaks down here
a
b
Relative Viscosity
Silicate Volume Fraction
10^0
10^1
10^2
10^3
10^4
0.0
0.1
0.2
0.3
0.4
0.5
0.6
0.7
0.8

The above discussion concerning the viscosity of a suspension is valid only when the ambient fluid is Newtonian (i.e., the relationship between the viscous shear stress and the strain rate is linear). Hence, the accuracy of this model for the rheology of an ice-silicate mixture depends on the extent to which ice behaves like a Newtonian fluid over geologic time.

Ice I may be expected to creep via diffusional flow or by the motion of dislocations (Shoji and Higashi, 1978; Goodman et al., 1981; Weertman, 1983). In the former mechanism, the strain rate is proportional to the shear stress, while in the latter it is approximately proportional to the cube of the stress. The dominance of one mechanism over the other depends on the shear stress causing the flow, and on the temperature and grain size of the ice. For shear stresses of ~1 bar or less, temperatures of ~ -15°C, and grain size of $\lesssim$1 mm, diffusional flow will be the dominant creep mechanism (Goodman et al., 1981). At lower temperatures (~ -30°C), diffusion may dominate for a grain size $\lesssim$1 cm (Shoji and Higashi, 1978). However, the dependence on grain size is controversial (Weertman, 1983). Since diffusional creep mimics Newtonian flow, ice I would behave as a Newtonian fluid if diffusion dominates.

In non-Newtonian flow, the strain rate depends more strongly on stress. The energy dissipation is a product of stress and strain rate and is consequently a weaker function

of strain rate than in the Newtonian case. The effect of the suspended silicate particles is to increase the straining motion of the flow but since the energy dissipation is less dependent on strain rate in the non-Newtonian case, it follows that the effective relative viscosity is lower for a non-Newtonian fluid than for a Newtonian fluid, other factors being equal. This assertion must remain qualitative, unfortunately, because of the lack of experimental data. In particular, we cannot determine whether Newtonian or non-Newtonian flow dominates in the icy satellites because we cannot estimate the grain size.

Another effect not included in the Newtonian suspension model is that of dispersion hardening. This effect will be important when there are silicate particles of the same size as or smaller than the ice grain size. The data of Baker et al. (1979) show that the inclusion of a small fraction of silicate particles leads to an increase of the apparent activation energy for diffusion-controlled creep between -10°C and -40°C (also see Hooke et al., 1972). For a silicate fraction of about 0.01 or less, this increase is approximately 20%, and is about 30% for a silicate fraction of ~0.05. If one considers a particle size distribution in which $n(m) \sim m^{-1}$ then it is possible that a large fraction of the silicate volume resides in particles $\lesssim$ the grain size, but only if the low mass cut-off is much smaller than the grain size. Since the low mass cut-off is very poorly

constrained (even if we knew in detail the satellite accumulation process), evaluation of the importance of dispersion hardening is not yet possible. However, a 20% increase in activation energy can give as much as two orders of magnitude increase in viscosity, so this process could dominate over the simple suspension effect.

As an example of the possible role of dispersion hardening, consider the case where the particle size distribution extends from 1 km (planetesimals) to 0.1 μ (dust) according to $n(m) \propto m^{-1}$. The mass fraction residing in particles $\leq$1 mm, our nominal ice grain size, is then ~40%. For a body composed of 50% ice, 50% rock, dispersion hardening may increase the viscosity at -10°C by about one order of magnitude relative to pure ice (Hooke et al., 1972).

At the large mass end, the settling of large silicate rocks in the polydisperse rock-ice medium is complicated because it may depend on the pair distribution function of the inclusions as well as the volume concentration (Batchelor, 1982). An application of Stokes law together with elementary sedimentation theory (Allen, 1970) indicates that inclusions $>$0.1 km in diameter will settle from the convecting medium (Anderson, 1981). As in the small particle limit, we are unable to assess the fraction of the total silicate mass involved.

3. Subsolidus Convection

We consider the interior of a homogeneous rock-water ice satellite in which a specified heat flux F_{conv} is transported by subsolidus convection. For simplicity, we assume a balance between this heat flux and the instantaneous radiogenic heat production, although significant deviations from this steady state are known to be possible. The heat flux can be expressed as

$$F_{conv} = \frac{k\Delta T}{a} Nu \qquad (5)$$

where k is the thermal conductivity, a is the satellite radius, ΔT is the temperature drop (in excess of the adiabatic temperature drop) across the convecting region and Nu is the Nusselt number given by

$$Nu \cong c\, Ra^{1/3} \qquad (6)$$

$$Ra \equiv \frac{g\alpha\Delta T a^3}{\kappa\nu} \qquad (7)$$

Here, c is a constant (discussed below), Ra is a Rayleigh number, g is the acceleration of gravity, α is the

coefficient of thermal expansion, ν is the kinematic viscosity of the medium (evaluated in a way to be described) and κ is the thermal diffusivity. Parameterizations of this kind have been used extensively in planetary modeling and are discussed more fully in Schubert (1979), for example.

It is assumed that the outermost shell of the satellite can be treated as a rigid, conducting layer. The important physical assumption here is that the convection does not penetrate to the surface. The thermal structure of the model is then as shown in Figure 2. The structure illustrated assumes adiabaticity everywhere below the upper boundary layer, implying that the convective flow is uninhibited by phase boundaries. Flow through a phase boundary involves the potentially competing effects of latent heat and phase boundary distortion (Schubert et al., 1975) and linear stability analysis suggests that there may be circumstances for which ice phase boundaries are stabilizing (see also Thurber et al., 1980). However, linear stability analysis has little relevance at Ra ~ 10^8, the situation of interest, and there are no relevant finite amplitude calculations of the kind performed by Richter (1973) for the earth. Consequently, the effect of phase transitions is not yet known for icy satellites.

The largest uncertainty in the parameterization of equations (5)-(7) is in the choice of temperature at which to evaluate the viscosity ν. We have chosen to evaluate ν

Figure 2: Thermal structure of the convection model discussed in Section 3. The situation shown is that of a subcritical case in which the thermal profile is everywhere subsolidus. Note there is an 11 K temperature jump in the adiabat at the Ice I-Ice III phase boundary. The thicknesses and depths of the rigid cap and boundary layer are exaggerated for the purposes of exposition.

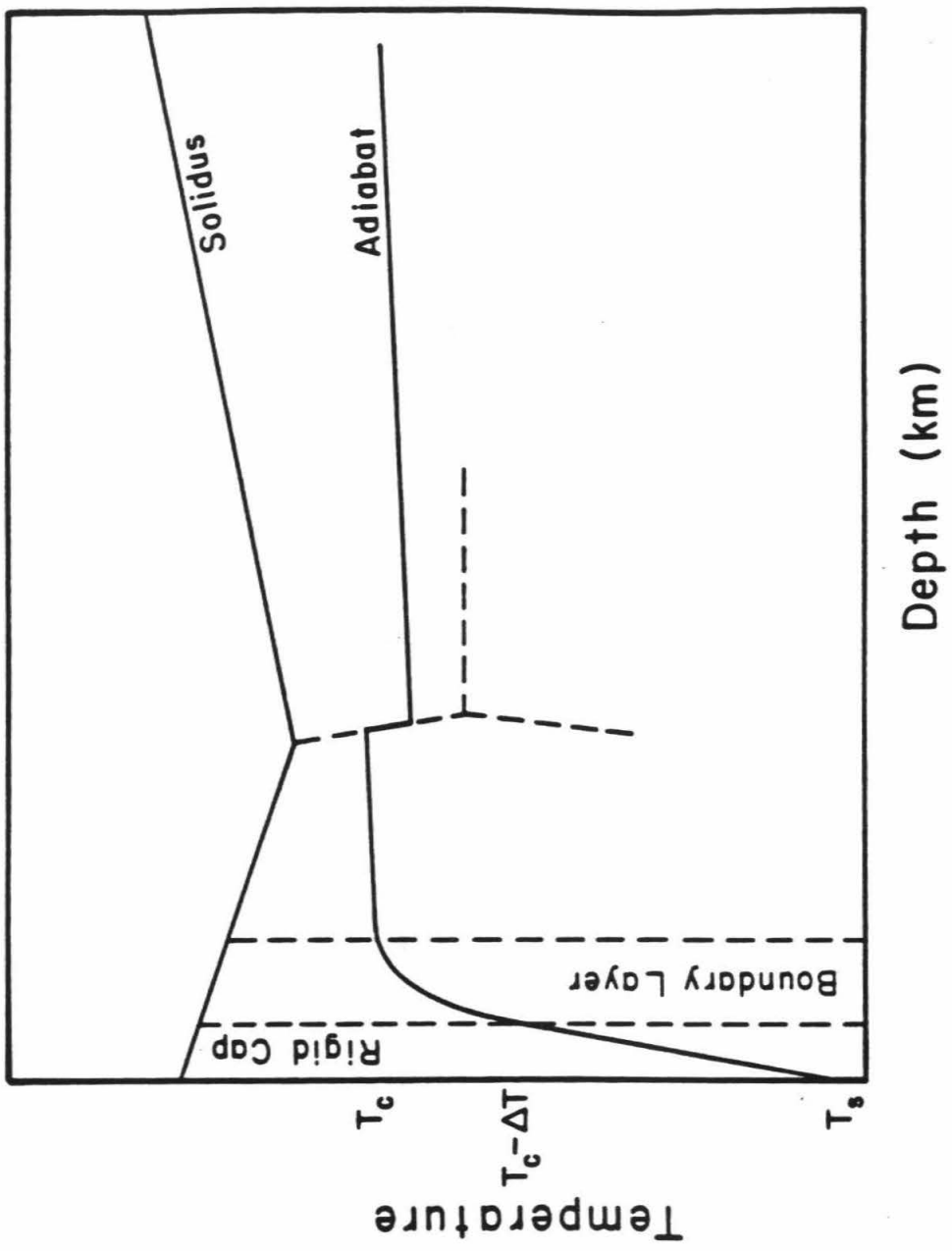
Solidus
Adiabat
Rigid Cap
Boundary Layer
T_c
$T_c-\Delta T$
T_s
Temperature
Depth (km)

at the mean temperature of the boundary layer, $T_c - \Delta T/2$, where T_c is the temperature at the top of the adiabatic interior region. This was also the choice of Reynolds and Cassen (1979). It is not directly compatible with the experimental work of Booker (1976) and Booker and Stengel (1978), or the more recent work of Richter et al. (1982). The problem is that the experiments involved viscosity variations of $\leq 10^5$, but the viscosity of a satellite varies by a factor $\sim 10^9$-10^{12} between the interior and the surface. If one applies the above experimental results, without modification, to convection in icy satellites, then the viscosity is to be evaluated at the temperature which is the average of the top and bottom boundary conditions, i.e., the temperature just below the regolith and the temperature in the convecting mantle, respectively. For Ganymede this temperature would be the average of ~130 K (Shoemaker et al., 1982) and 253 K (when we are considering the onset of melting). However, if the top and bottom boundary conditions are taken to be the temperature at the top and bottom of the boundary layer, then the viscosity should be evaluated at a temperature of ~220 K (if we were to assume $\Delta T \sim 60$ K). Therefore, the manner in which the experimental results are applied may lead to effective viscosities that differ by a factor of ~100, and uncertainties of up to a factor ~3 in the value of F_{conv} for a given choice of T_c.

Clearly, our choice (and that of Reynolds and Cassen) is more reasonable in the limit of infinite viscosity contrast since there must be an asymptotic state in which the viscosity at the mean of the boundary temperatures is so enormous that it plays no role in the convection. It is not known whether ten orders of magnitude is enough viscosity variation to provide asymptopic conditions. Our choice is conservative in the sense that it tends to underestimate the viscosity and make internal melting less likely.

The value of the constant c in equation (6) is uncertain because it includes the effects of a spherical geometry and boundary conditions, and must also compensate for the likelihood that the exponent of 1/3 in equation (6) is only an approximation. Based on the experimental results (Booker, 1976; Richter et al., 1982) and theoretical considerations (Schubert, 1979) it is likely that c is in the range 0.08 and 0.16. We have performed calculations for these limiting cases. (It is worth mentioning at this point that if c is even lower, about 0.06, then the calculations described below would predict that partial melting could occur in a pure ice mantle in a completely differentiated body with the composition of Ganymede. This illustrates the difficulty of accurately evaluating the importance of suspended silicates.)

Combining equations (5), (6), and (7),

$$F_{conv} = c \left(\frac{k^3 g \alpha}{\kappa} \right)^{1/3} \left(\Delta T \right)^{4/3} \nu^{-1/3} \qquad (8)$$

The viscosity is a function of the temperature and of the silicate volume fraction of the mixture. We adopt

$$\nu = \eta_r(\phi)\ \nu_0\ \exp\{ A \left[\frac{T_m}{T_\nu} - 1 \right] \} \qquad (9)$$

where η_r is the relative viscosity; ν_0 the viscosity of pure ice at the zero-pressure melting point;, T_m is the melting temperature in the boundary layer (~273 K); T_ν is the average temperature in the boundary layer; and A is a constant. We consider cases in which the value of A is 20, 25, and 35. Passey (1982) has found that A = 25 ± 3 leads to a best fit for his crater relaxation models of Ganymede. Hence, for pure ice A = 25 may be most realistic. However, as mentioned in the previous section, if dispersion hardening effects are important, then the apparent activation energy for creep is higher, and the value chosen for both ν_0 and A should be larger.

Implicit in this discussion has been the assumption that the ice will flow in a Newtonian manner. The maximum shear stress to which the ice is subjected in the convection will

occur in a cold, sinking plume, and is of order $0.01\alpha g\Delta Ta$ (Schubert et al., 1981). For a body like Ganymede, and with $\Delta T \sim 60$ K, the maximum shear stress is about 1 bar. Hence, if the ice grain size is sufficiently small ($\lesssim$1 mm - 1 cm), diffusional creep should be the dominant flow mechanism in the boundary layer, and therefore the ice will flow in a Newtonian manner. For ice grain size of about 1 cm or larger, the Newtonian flow assumption should break down. If such is the case, our simple Newtonian suspension model for the ice-silicate mixture's viscosity would no longer be applicable. The Nusselt-Rayleigh number relation may still be approximately applicable, however (Parmentier and Morgan, 1982).

We evaluate ΔT by assuming that the system adjusts ΔT in order to maximize the convective heat flux for given T. This assumption <u>minimizes</u> the likelihood of melting. One finds

$$\Delta T = 2\,\Upsilon(T_c) \equiv 2\{\, b(T_c) - [\, b^2(T_c) - T_c^2 \,]^{1/2} \,\} \qquad (10)$$

where

$$b(T_c) = T_c + \frac{A}{8} T_m \quad . \qquad (11)$$

Substituting equation (10) into (8) and (9),

$$F_{conv} = c\left(\frac{k^3 g\alpha}{\eta_r \nu_0 \kappa}\right)^{1/3} \left[\, 2\gamma(T_c) \,\right]^{4/3}$$

$$\exp\left\{ -\frac{A}{3} \left[\frac{T_m}{T_c - \gamma(T_c)} - 1 \right] \right\} \quad . \tag{12}$$

In steady-state the convective heat flux near the surface is balanced by the radiogenic heat production in the interior. If H is the chondritic heating rate per unit mass, ρ_r is the average density of the silicates, and ϕ is the volume concentration of silicate particles in the mixture, then the radiogenic heat production per unit volume is

$$H_v = \rho_r \, \phi \, H \quad . \tag{13}$$

If the silicate particles are uniformly distributed throughout the icy body, then, in steady-state,

$$F_{conv} = \frac{a}{3} \rho_r \, \phi \, H \quad . \tag{14}$$

The radiogenic heat production in the outer rigid cap is justifiably neglected. Substituting for F_{conv} from equation (12), we have

$$F_{conv} = c\left(\frac{k^3 g\alpha}{\eta_r \nu_0 \kappa} \right)^{1/3} \left[2\gamma(T_c) \right]^{4/3}$$

$$\exp\left\{ -\frac{A}{3} \left[\frac{T_m}{T_c - \gamma(T_c)} - 1 \right] \right\} = \frac{a}{3} \rho_r \phi H \quad . \quad (15)$$

Given ϕ, this equation may be solved for T_c, the steady-state mantle temperature. Conversely, if T_c is specified beforehand, equation (15) may be solved for ϕ. Since the adiabatic temperature gradient is very small (~0.02 K/km), it is a good approximation to define the critical state as the one for which T_c = 253 K. If T_c < 253 K then the adiabat shown in Figure 2 intercepts the ice I-ice III phase boundary and remains subsolidus at greater depths (assuming the convection penetrates phase boundaries). If T_c > 253 K, then the adiabat intercepts the ice I-liquid phase boundary and partial melting must ensue. Solution of equation (15) with T_c = 253 K provides an estimate of the "critical" volume fraction ϕ_{max} above which at least partial melting must occur. This "critical" value of ϕ should not be confused with the parameter ϕ_c introduced in Section 2.

In Figure 3, ϕ_{max} is shown as a function of satellite radius, assuming the relative viscosity is given by the lower bound, equation (4). Parameter choices are listed in Table I. The heating rate chosen is appropriate to that of carbonaceous chondrites taken back four billion years (Davies, 1980). Figure 3 is based on the choices A = 25, ρ_r = 2.5 and 3.5 g cm^{-3}; selected results for other choices are tabulated in Table II.

If one assumes an average silicate density of 2.5 g cm^{-3} (appropriate for hydrated silicates) for the outer satellites, then a body of the size of Ganymede or Callisto (a ~ 2500 km) would have a critical silicate volume fraction of about 0.43 (for the choices c = 0.08 and A = 25). Once a value for the average silicate density is adopted, it is possible to estimate the actual silicate volume fraction from the mean density of the satellite. The density of Ganymede is 1.93 g cm^{-3}, and that of Callisto is 1.83 g cm^{-3} (Smith et al., 1979). These densities translate to silicate volume fractions for Ganymede and Callisto of ϕ = 0.55 and ϕ = 0.44, respectively. For Ganymede, $\phi > \phi_{max}$, whereas for Callisto, $\phi \approx \phi_{max}$. Hence, if a silicate density of 2.5 g cm^{-3} is realistic for these satellites, Ganymede could have suffered partial melting, beginning at the melting-curve minimum, due to radiogenic heating alone. The result for Callisto is too marginal to make the same conclusion.

Figure 3: Critical silicate volume fraction vs. satellite radius. a) $c = 0.08$, $A = 25$, $\rho_r = 2.5\ g.cm^{-3}$; b) $c = 0.16$, $A = 25$, $\rho_r = 3.5\ g.cm^{-3}$. The points labeled Ganymede, Callisto, and Rhea indicate the radius and the actual silicate volume fraction of those satellites.

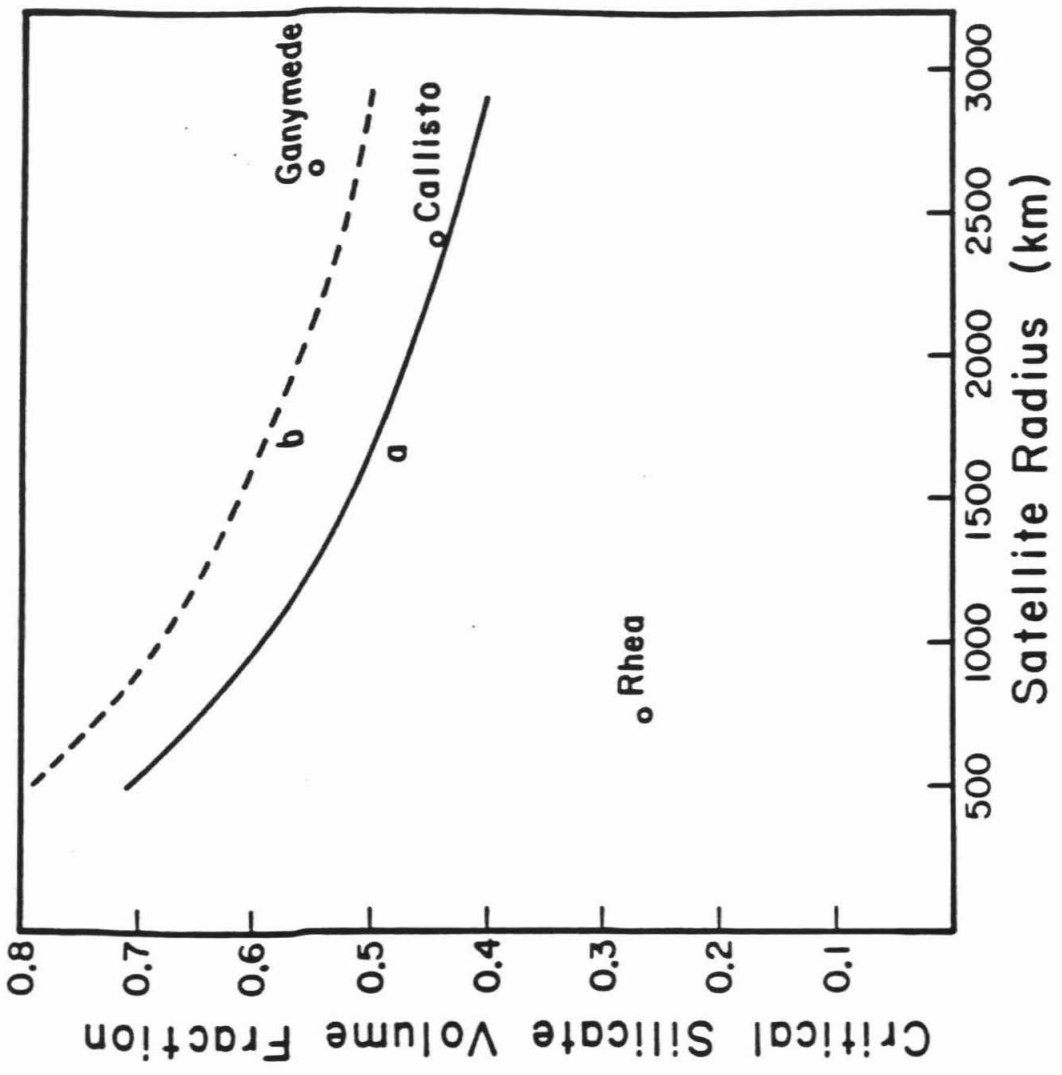
Critical Silicate Volume Fraction
0.8
0.7
0.6
0.5
0.4
0.3
0.2
0.1
500
1000
1500
2000
2500
3000
Satellite Radius (km)
Ganymede
Callisto
Rhea
a
b

Table I. Values of Parameters Used in the Model.

k	3×10^{5} erg cm^{-1} sec^{-1} K^{-1}
g	0.05 a(km) cm/sec^{2}
α	10^{-4} K^{-1}
κ	10^{-2} cm^{2}/sec
ν_0	10^{14}-10^{15} cm^{2} sec^{-1}
a	500-2500 km
A	20-35
T_m	273 K
ρ_r	2.5-3.5 g cm^{-3}
H	1.6×10^{-7} erg gm^{-1}
c	0.08-0.16

Table II: Critical Silicate Volume Fraction for Bodies with Different Radii and Average Silicate Densities.

Rad. (km)	Silicate Dens. ($g\ cm^{-3}$)	c = 0.08 A = 20	c = 0.08 A = 25	c = 0.08 A = 35	c = 0.16 A = 25
500	2.5	.79	.71	.55	>.80
	3.0	.75	.66	.50	>.80
	3.5	.72	.62	.46	.79
1500	2.5	.62	.52	.35	.70
	3.0	.57	.47	.31	.66
	3.5	.53	.43	.28	.62
2500	2.5	.53	.43	.28	.62
	3.0	.47	.38	.22	.56
	3.5	.44	.34	.21	.52

Notice from Table II that if a silicate density of 3.5 g cm^{-3} is assumed, the critical volume fraction is 0.35. The actual silicate volume fractions of Ganymede and Callisto implied by this silicate density are only 0.31 and 0.26, respectively. Therefore, for the high silicate density case, the conclusion concerning internal melting in Ganymede may be reversed, and Callisto will also not melt. The results for choices of c and A other than 0.08 and 25 are shown in Table II.

In Table III the critical volume fraction and the actual volume fraction are shown for a few icy satellites. The values for the critical volume fraction are for the case where c = 0.08 and A = 25, and we have assumed a mean silicate density of 2.5 g cm^{-3} in deriving the actual silicate fractions for the satellites. The Saturnian satellites are included for comparison as if they were composed of just water ice and silicates. Except for Titan, they are too small to have suffered any melting.

Table III. Critical Silicate Volume Fraction and Actual Silicate Volume Fraction for a Few Icy Satellites ($c = 0.08$ and $A = 25$; $\rho_{silicate} = 2.5$ g cm^{-3})

Satellite	Critical Volume Fraction	Actual Volume Fraction
Ganymede	0.42	0.55
Callisto	0.44	0.44
Dione	0.68	0.33
Rhea	0.63	0.27
Titan	0.42	0.52

4. Melting and Differentiation

Consider a homogeneous rock-water ice satellite which starts out cold and heats up by radiogenic heating until the temperature at 2 kbar pressure is 253 K, the solidus of water ice. Partial melting takes place, with the water percolating buoyantly upwards along narrow channels created at grain boundaries. This porous flow is seen in the migration of brine through sea ice (Kingery and Goodnow, 1963) and is the commonly assumed mechanism for magma migration in partially molten rock (Turcotte, 1982). Subsequent, macroscopic water transport in diapirs or along cracks may occur. The remaining, silicate-rich, residue is heavier than the underlying material and can undergo a Rayleigh-Taylor instability (Chandrasekhar, 1961; Ramberg, 1981; Schubert et al., 1981).

Two questions are posed in this section. Is the energy release from gravitational energy sufficient to melt the rest of the ice? Can the differentiation and melting occur rapidly once initiated? The answer to both questions for large satellites such as Ganymede is a qualified yes. We begin the analysis by considering the gravitational energy associated with differentiation. For simplicity, we initially neglect the phase changes and compressibility of ice.

A uniform density body of mass M and radius R has a gravitational energy

$$E_{Gr,i} = -\frac{3}{5}\frac{GM^2}{R} \qquad (16)$$

If this body differentiates into a rock core and ice mantle, then it is straightforward to show that the gravitational energy is then

$$E_{Gr,f} = -\frac{3}{5}\frac{GM^2}{R}\left[z_1^2 y^5 + z_2^2(1-y^5) + \frac{5}{2} z_2(z_1-z_2)y^3(1-y^2)\right] \qquad (17)$$

where $z_1 = \rho_r/\bar{\rho}$, $z_2 = \rho_i/\bar{\rho}$, $y = a_c/a$, ρ_r is the rock density, ρ_i is the ice density, $\bar{\rho}$ is the average (satellite) density, and a_c is the radius of the rock core in a satellite of radius a. The difference, $E_{Gr,i} - E_{Gr,f}$, must go into heat. Numerical computation shows that to an adequate approximation, the energy released per unit mass is

$$Q_{Gr} \simeq 6 \times 10^9 \beta(1-\beta)\bar{\rho}\left(\frac{R}{2500\ \text{km}}\right)^2 \text{erg} \qquad (18)$$

where β is the silicate mass fraction. It is assumed that $\rho_r = 2.5\ \text{g cm}^{-3}$ and $\rho_i = 1.2\ \text{g cm}^{-3}$. Although this formula has the right limits as $\beta \to 0$ and $\beta \to 1$, the numerical

coefficient is most accurate for $\beta \sim 0.7$ and $\bar{\rho} \sim 1.9$ g cm^{-3}. For Ganymede, $Q_{Gr} \simeq 2 \times 10^9$ erg/g. The latent heat of water ice per gram of the mixture is within 20% of 0.85×10^9 erg/g for each of the ice phases (Bridgman, 1937). The excess of $\sim 1.1 \times 10^9$ erg/g is sufficient, in principle, to raise the temperature of the satellite by about 100 K. It follows that Ganymede or Callisto is (just) capable of melting all its water ice if all the energy of differentiation were suddenly supplied when the interior is at ~250 K. A more accurate calculation is not presently warranted due to the larger uncertainties associated with differentiation dynamics (discussed below).

Differentiation would also redistribute the ice among the various ice phases. This can substantially change the satellite radius (Squyres, 1980) and, necessarily, the gravitational energy. It is important to realize, however, that only the latent heats are available for thermal energy changes; the gravitational energy change associated with the volume change is accommodated by the work done by pressure. (This is an example of Le Chatelier's principle.) The latent heat effect is rather small, equivalent to ~20 K drop averaged over the satellite (primarily due to ice VIII displaced to ice VI). The consequences of finite compressibility are even smaller, of order ~5 K.

We turn now to the issue of differentiation dynamics. Figure 4 shows a likely thermal structure during

Figure 4: Thermal structure during differentiation. The temperature profile in the partially molten region, of width δ, follows the solidus.

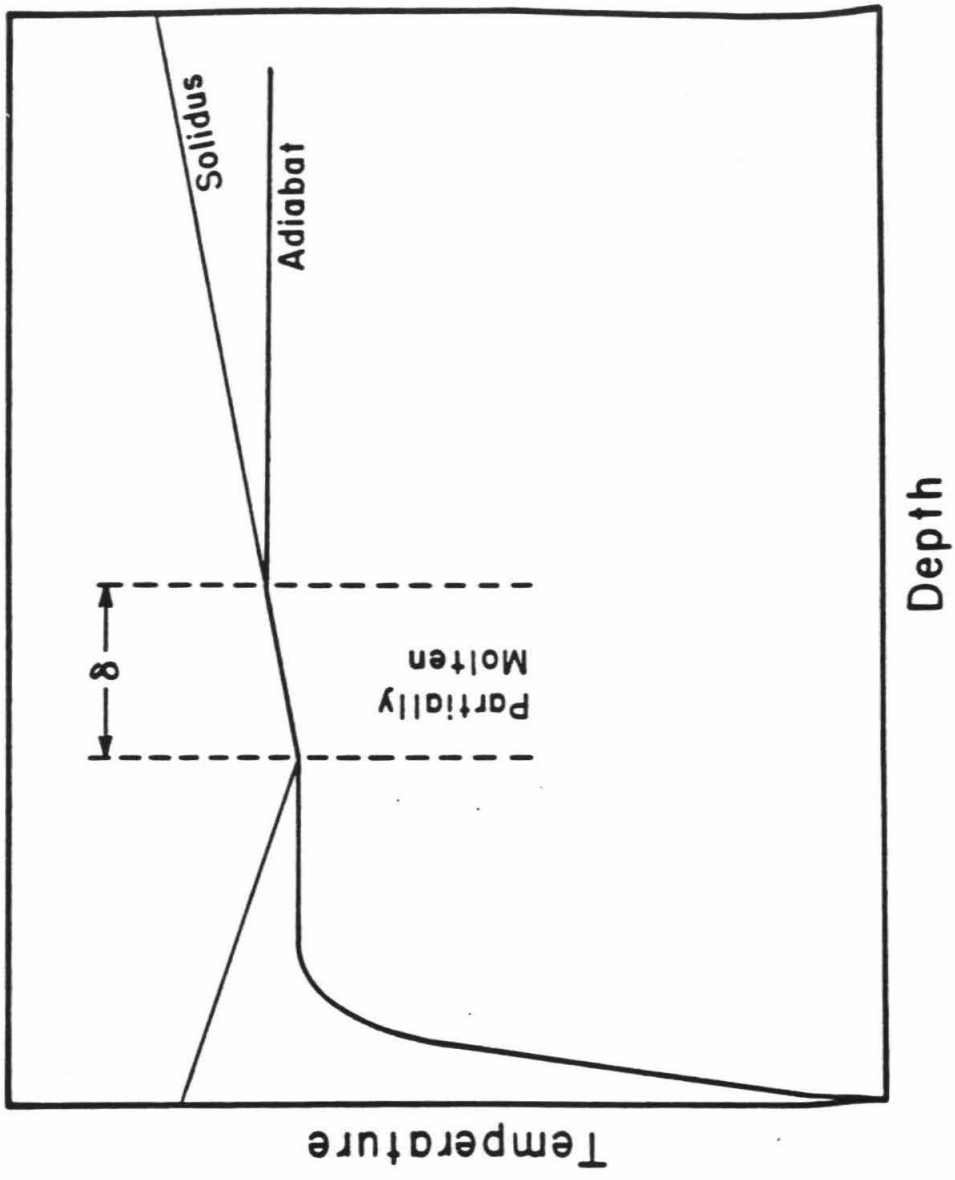
Solidus
Adiabat
Partially
Molten
δ
Depth
Temperature

differentation. So long as the ice I region contains enough silicates to be heavier than water, a macroscopic water layer is buoyantly unstable. The temperature profile in this layer is likely to follow part of the solidus, as indicated. We assume, for the moment, that differentiation is so rapid that the energy released by differentiation cannot be eliminated to the surface by convection. The deeper regions must then heat up, increasing the thickness δ of the partially molten region. The physical picture is as follows: water percolates upward from the partially molten region leaving behind a silicate-rich residue. The Rayleigh-Taylor instability time scale for this residue is given by

$$\tau_{RT} \simeq \frac{4\nu}{g(\Delta\rho/\rho)\delta} \qquad (19)$$

where $\Delta\rho$ is the average density difference between the residue and the underlying material of density ρ and kinematic viscosity ν. After each interval of time τ_{RT}, silicate-rich globules $\sim\delta$ in radius break away from the phase boundary region, to be immediately replaced by more ice-rich material from below. This replacement material rises adiabatically a distance δ and any heat in excess of

the solidus is used to melt the ice. It follows that if the water thereby produced is allowed to escape, then

$$\frac{\Delta\rho}{\rho} \simeq -\frac{\delta C_p}{L}\left(\frac{dT}{dr}\right)_{ph} \qquad (20)$$

where L is the latent heat, C_p is the specific heat of the mixture, and the derivative represents the Clausius-Clapeyron slope of the ice solidus.

It is assumed that the downgoing 'blobs' of residue mix uniformly with deeper regions. This material eventually returns to the partially molten region to undergo further refinement. The total differentiation time τ_{diff} for the whole satellite is then $\sim(a/\delta)(\rho/\Delta\rho)\tau_{RT}$ if δ is constant. This can be expressed as

$$\tau_{diff} \simeq (4 \times 10^4 \text{ yrs})\left(\frac{100 \text{ km}}{\delta}\right)^4\left(\frac{\nu}{10^{15} \text{ cm}^2/\text{s}}\right) \qquad (21)$$

for parameters appropriate to Ganymede. The appropriate viscosity is that of high pressure phases of ice, modified by silicate inclusions, and may be similar to that for ice I (Poirier, 1982), although his experiments are at higher stress levels than encountered in convection. It is clear that once δ becomes of order 10^2 km, the process is

extremely rapid and the assumption of heat retention is reasonable.

However, this analysis overlooks the problem of initiation: δ must start small and the time scale for δ = 10 km is already $\sim 10^8$ years. The value of δ depends on the extent to which the satellite has differentiated. If no heat is lost, then δ becomes comparable to the radius near the completion of differentiation. In other words, $\delta \sim xa$ where x is the fraction of the satellite that has differentiated. However,

$$x(t) \simeq \int_0^t \frac{dt}{\tau_{diff}} \simeq \int_0^t \frac{\delta(t)\Delta\rho(t)}{a\rho\tau_{RT}(t)}\, dt \qquad (22)$$

where t = 0 is the onset of differentiation. It follows that

$$\frac{d\delta(t)}{dt} \simeq \frac{a}{\tau_0}\left(\frac{\delta}{a}\right)^4 + \Delta \qquad (23)$$

where $\tau_0 \sim 0.1$ yr and Δ is the effect of radiogenic heating alone. It is possible to increase δ from 0 to ~10 km in $\sim 10^7$ years by radiogenic heating, at which point a differentiation-driven thermal runaway ensues. Over 90% of the differentiation could take as little as 10^3 yr.

Clearly, radiogenic heating must play a crucial role. It is not sufficient to just reach 253 K, rather it is necessary to heat the deeper regions to ~300 K. However, this is only a modest additional requirement. It is also apparent that the latter stages of the differentiation may be inhibited by the increasing viscosity of silicate-rich residues. Complete expulsion of water may not occur until later radiogenic heating in a rock-rich core melts the remaining trapped ice and allows the water to escape upwards. Despite the possible rapidity of the major part of the differentiation, the entire process from an initially cold undifferentiated satellite to complete differentiation may take up to 10^9 years.

It is conceivable that this analysis may help explain the strikingly different surficial appearances of Ganymede and Callisto observed by Voyager (Smith et al., 1979a,b). Suppose that both Ganymede and Callisto accreted homogeneously without undergoing any substantial accretional heating. Three effects may combine to make Ganymede more susceptible to subsequent melting and differentiation than Callisto: it may have started warmer (because it formed in a warmer region of the protojovian nebula), it has a higher silicate content and it has a higher heat flow. Ganymede may have reached the solidus after about 5×10^8 years and undergone 'runaway' differentiation. The availability of buoyant, clean ice together with the volumetric expansion

that accompanies differentiation may have provided the environment in which the grooved terrain could form. (The smooth units on Ganymede must, however, have come much later than 4.0 b yr if estimates of cratering fluxes are anywhere near correct; Shoemaker, 1982.) In contrast, Callisto may have never reached the solidus and never differentiated.

Other proposals to explain the differences between Ganymede and Callisto rely on small differences in heat flux (Cassen et al., 1980) or on differences in the accretional environment, which may have allowed Ganymede, but not Callisto, to differentiate during accretion (Schubert et al., 1981; Lunine and Stevenson, 1982). The interesting feature of the scenario described above is that unlike the other proposals, it shows that two very different evolutionary outcomes (runaway differentiation and no differentiation) can arise from small changes in bulk parameters such as silicate content. The scenario proposed here does have some unsatisfactory aspects, however (as do all the current proposals). First, it cannot be quantified with sufficient precision to be tested with confidence. Second, it requires the coincidence that the critical state lie between Ganymede and Callisto. The a priori probability of this is low. Third, it requires cold accretion. This is difficult to reconcile with current models of the accretion process. More work, including observations and experiments, is needed before a choice can be made between competing

hypotheses seeking to explain why Ganymede and Callisto differ so much.

5. Conclusions

Several general conclusions arise from the calculations presented here:

1. Rock inclusions in ice at a level encountered in cosmic bodies are likely to increase the viscosity of the medium by about one order of magnitude, perhaps even more. This is a large enough effect to be important in thermal evolution and crater relaxation calculations.
2. Convective self-regulation may fail during the evolution of large icy satellites. "Self-regulation" refers here to the ability of solid state convection to eliminate radiogenic heat production without the temperature reaching the melting point of ice. The critical parameters (satellite radius and silicate content) characterizing the onset of a failure of self-regulation are similar to the actual characteristics of Ganymede and Callisto.
3. In homogeneous satellites of this size or larger, the onset of partial melting can trigger a runaway differentiation into a rock core and almost pure ice mantle.

The application of these general conclusions to observable features of the solar system is necessarily speculative at this stage, because of the difficulty of quantification. We have offered the conjecture that Ganymede may have undergone runaway differentiation whereas Callisto remained an undifferentiated, primordial mixture. This might explain the striking surficial dissimilarity of these two satellites, provided they accreted as cold, undifferentiated bodies. However, the most important need at this stage is more experimental data on rock-ice mixtures. We hope that the ideas presented here have provided sufficient motivation and stimulation to justify the appropriate experiments and observations.

Acknowledgments

This work is supported by NASA grant NAGW-185 of the Planetary Geophysics and Geochemistry program.

References

Allen, J.R.L. (1970). Physical Processes of Sedimentation, pp. 36-57. New York: American Elsevier Publishing Co., Inc.

Anderson, A. (1981). Rock and convection in icy bodies. Unpublished term paper, Caltech (available from D.J. Stevenson).

Baker, R.W. and W.W. Gerberich. (1979). The effect of crystal size and dispersed-solid inclusions on the activation energy for creep of ice. J. Glaciol. **24**, 179-194.

Batchelor, G.K. (1982). Sedimentation in a dilute polydisperse system of interacting spheres. J. Fluid Mech. **119**, 379-408.

Booker, J.R. (1976). Thermal convection with strongly temperature-dependent viscosity. J. Fluid Mech. **76**, 741-754.

Booker, J.R. and K.C. Stengel. (1978). Further thoughts on convective heat transport in a variable-viscosity fluid. J. Fluid Mech. **86**, 289-291.

Bridgman, P.W. (1937). The phase diagram of water to 45,000 kg/cm^2. J. Chem. Phys. **5**, 964-966.

Cassen, P.M., S.J. Peale, and R.T. Reynolds. (1980). On the comparative evolution of Ganymede and Callisto. Icarus **41**, 232-239.

Chandrasekhar, S. (1961). Hydrodynamic and Hydromagnetic Stability. Oxford Univ. Press, London.

Cheng, D.C-H. and Richmond, R.A. (1978). Some observations on the rheological behavior of dense suspensions. Rheol. Acta 17, 446-453.

Chong, T.S., E.B. Christiansen and A.D. Baer. (1971). Rheology of concentrated suspensions. J. Appl. Polymer Sci. 15, 2007-2021.

Consolmagno, G.J. and J.S. Lewis. (1976). Structural and thermal models of icy Galilean satellites. In Jupiter, (T. Gehrels, Ed.), pp. 1035-1051. Univ. of Arizona Press, Tucson.

Davies, G.F. (1980). Thermal histories of the Earth. J. Geophys. Res. 85, 2527.

Eilers, V.H. (1941). Die viskositat von emulsionen hochviskoser stoffe als funktion der konzentration. Kollid Z. 97, 313-321.

Einstein, A. (1906). Eine neve bestimmung der molekuldimensionen. Ann. Phys. 19, 286.

Farris, R.J. (1968). Prediction of the viscosity of multimodal suspensions from unimodal viscosity data. Trans. Soc. Rheol. 12, 281-301.

Fujiwara, A., G. Kamimoto and A. Tsukamoto. (1977). Destruction of basaltic bodies by high velocity impact. Icarus 31, 277-288.

Goodman, D.J., H.J. Frost and M.F. Ashby. (1981). The plasticity of poly-crystalline ice. Philos. Mag. 43, 665-695.

Hartmann, W.K. (1969). Terrestrial, lunar and interplanetary rock fragmentation. Icarus 10, 201-213.

Hooke, R.L., B.B. Dahlin and M.T. Kauper. (1972). Creep of ice containing dispersed fine sand. J. Glaciol. 11, 327-336.

Kingery, W.D. and W.H. Goodnow. (1963). Brine migration in sea ice. In Ice and Snow, (W.D. Kingery, Ed.), pp. 237-247. MIT Press, Cambridge, Mass.

Lanciano, P., C. Federico and A. Coradini. (1981). Primordial thermal history of growing planetary objects. Lunar Planet. Sci. XII Abs, 586-588.

Lewis, J.S. (1971). Satellites of the outer planets: Thermal models. Science 172, 1127-1128.

Lunine, J.I. and D.J. Stevenson. (1982). Formation of the Galilean satellites in a gaseous nebula. Icarus 52, 14-39.

Moshev, V.V. (1979). Viscosity relationships for heavily filled suspensions. Fluid Mech.-Soviet Res. 8, 88-96.

Parmentier, E.M. and J. Morgan. (1982). Thermal convection in non-Newtonian fluids: Volumentric heating and boundary layer scaling. Geophys. Res. 87, 7757-7762.

Parmentier, E.M. and J.W. Head. (1979). Internal processes affecting surfaces of low density satellites: Ganymede and Callisto. J. Geophys. Res. 84, 6263-6276.

Passey, Q. (1982). Viscosity structure of the lithospheres of Ganymede, Callisto, and Enceladus, and the Earth's upper mantle. Thesis, California Institute of Technology.

Poirier, J.P. (1982). The rheology of ices: A key to the tectonics of the ice moons of Jupiter and Saturn. Nature 299, 683-688.

Ramberg, H. (1981). Gravity, Deformation and the Earth's Crust. Academic Press, New York.

Reynolds, R.T. and P.M. Cassen. (1979). On the internal structure of the major satellites of the outer planets. Geophys. Res. Lett. 6, 121-124.

Richter, F.M. (1973). Finite amplitude convection through a phase boundary. Geophys. J. R. Astron. Soc. 35, 265-276.

Richter, F.M., H.-C. Nataf and S.F. Daly. (1982). Heat transfer and horizontally averaged temperature of convection with large viscosity variations. Submitted to J. Fluid Mech.

Roscoe, R. (1952). The viscosity of suspensions of rigid spheres. British J. Appl. Phys. 3, 267-269.

Safronov, V.F. (1972). Evolution of the Protoplanetary Cloud and Formation of the Earth and Planets. NASA Tech. Transl. TTF-677.

Schubert, G. (1979). Subsolidus convection in the mantles of the terrestrial planets. Ann. Rev. Earth Planet. Sci. 7, 289-342.

Schubert, G., D.J. Stevenson and K. Ellsworth. (1981). Internal structures of the Galilean satellites. Icarus **47**, 46-59.

Schubert, G., Yuen, D.A. and Turcotte, D.L. (1975). Role of phase transitions in a dynamic mantle. Geophys. J.R. Astron. Soc. **42**, 705-735.

Shoemaker, E.M., Lucchitta, B.K., Wilhelms, D.L., Plescia, J.B. and Squyres, S.W. (1982). The geology of Ganymede. In The Satellites of Jupiter, (D. Morrison, Ed.), pp. 435-520. Univ. of Arizona Press, Tucson.

Shoji, H. and Higashi, A. (1978). A deformation mechanism map of ice. J. Glaciol. **21**, 419-427.

Smith, B.A., L.A. Soderblom, T.V. Johnson, A.P. Ingersoll, S.A. Collins, E.M. Shoemaker, G.E. Hunt, H. Masursky, M.H. Carr, M.E. Davies, A.F. Cook II, J. Boyce, G.E. Danielson, T. Owen, C. Sagan, R.F. Beebe, J. Veverka, R.G. Strom, J.F. McCauley, D. Morrison, G.A. Briggs, V.E. Suomi. (1979a). The Jupiter system through the eyes of Voyager 1. Science **204**, 951-971.

Smith, B.A., L.A. Soderblom, R.F. Beebe, J. Boyce, G.A. Briggs, M.H. Carr, S.A. Collins, A.F. Cook II, G.E. Danielson, M.E. Davies, G.E. Hunt, A.P. Ingersoll, T.V. Johnson, H. Masursky, J.F. McCauley, D. Morrison, T. Owen, C. Sagan, E.M. Shoemaker, R.G. Strom, V.E. Suomi, J. Veverka. (1979b). The Galilean satellites and Jupiter: Voyager 2 imaging science results. Science **206**, 927-950.

Squyres, S.W. (1980). Volume changes in Ganymede and Callisto and the origin of grooved terrain. Geophys. Res. Lett. **7**, 593-596.

Thomas, D.G. (1965). Transport characteristics of suspensions: VIII. A note on the viscosity of Newtonian suspensions of uniform spherical particles. Jour. Collid. Sci. **20**, 267-277.

Thurber, C.H., A.T. Hsui and M.N. Toksoz. (1980). Thermal evolution of Ganymede and Callisto: Effects of solid-state convection and constraints from Voyager imagery. Proc. Lunar Planet. Sci. Conf. 11th, 1957-1977.

Tozer, D. (1965). Heat transfer and convection currents. Philos. Trans. Roy. Soc. London Ser. A. **258**, 252-271.

Turcotte, D.L. (1982). Magma migration. Ann. Rev. Earth Planet. Sci. **10**, 397-408.

Weertman, J. (1983). Creep deformation of ice. Ann. Rev. Earth Planet. Sci. **11**, 215-240.

PART III. The Thermosphere of Titan

A. James Friedson and Yuk L. Yung

Division of Geological and Planetary Sciences

California Institute of Technology

Pasadena, California 91125

Published in J. Geophys. Res. 89, 85-90 (1984)

Contribution number 3907 from the Division of Geological and Planetary Sciences, California Institute of Technology, Pasadena, CA 91125.

Abstract

The diurnal variation of the vertical structure of Titan's thermosphere is calculated through simultaneous solution of the equations of heat transfer and hydrostatic equilibrium. The temperature and density profiles are found above the mesopause. The dynamical response of the thermosphere to heating is for the most part neglected. Nevertheless, we are able to draw some interesting qualitative and quantitative conclusions regarding the vertical structure. Heating of the upper thermosphere occurs primarily through absorption of solar Lyman α radiation by methane, with an additional amount of heating ($\lesssim$20%) due to low energy magnetospheric electron precipitation. The heat is conducted downward to the mesopause, where it is removed by IR cooling due principally to acetylene. The mesopause is found to occur where the density is 2.2×10^{12} cm^{-3} (736 km), and has a temperature of ~110 K. The exospheric temperature is unlikely to exceed 225 K in the course of a Titan day. The diurnally-averaged exospheric temperature is in the range 187-197 K depending on the amount of magnetospheric electron heating that is included in the model. The amplitude of the diurnal variation is found to be $\lesssim$28 K. We find that the vertical extent of the hydrogen cloud is too large to be explained in

terms of simple thermal escape of hydrogen from a ~225 K exosphere, and conclude that other processes must be important for populating or heating the neutral torus.

1. Introduction

As Voyager 1 passed through Titan's shadow, an occultation of the sun was observed at the morning and evening terminators by the ultraviolet spectrometer. Analysis of the occultation data has yielded the temperature and density near the exobase. The temperature at 3840 km (measured from the center of Titan) has been inferred to be 176 ± 20 K at the evening terminator and 196 ± 20 K at the morning terminator, while the N_2 density at the same altitude is seen to be nearly the same at each terminator and equal to $2.7 \pm 0.2 \times 10^8$ cm^{-3} (Smith et al., 1982).

It is apparent from the UVS observation that the morning and evening exospheric temperatures do not differ by much and may in fact be equal. This suggests that there may be little diurnal variation of the exospheric temperature. It should be pointed out, however, that the exospheric temperature at the morning and evening terminators of Venus was also measured to be quite similar (Keating et al., 1980), yet the exospheric temperature there exhibits a strong dependence on local time. Consequently, it would be ill-advised to conclude <u>a priori</u> that Titan's exospheric temperature does not substantially vary during one rotation period.

Our aim in the present study is to calculate the vertical structure of the thermosphere, down to the

mesopause, as a function of local time. In so doing we have ignored any dynamical response of the thermosphere except that associated with the "breathing velocity" of constant-pressure surfaces. Hence the amplitude of any diurnal variation predicted by our model must be interpreted as an upper limit. In addition, the calculation of the vertical structure is appropriate only for Titan's equator.

Our task of modeling the temperature profile in the upper thermosphere is complicated by the fact that it is difficult to accurately quantify the heating due to precipitating magnetospheric electrons. Results of the Plasma Science experiment on Voyagers 1 and 2 (Bridge et al., 1981, 1982) have shown that conditions in the magnetospheric environment at the orbit of Titan are complex and highly variable. While the Voyager 1 UVS observation provided useful information on the energy flux of electrons incident on Titan at the time of the observation, the electron flux at other points along Titan's orbit is poorly constrained. Hence, a model of the diurnal variation of the thermosphere which incorporates electron heating must make some initial, arbitrary assumption about the plasma conditions along the orbit.

The lack of any data concerning the rotation rate of the thermosphere becomes an additional source of uncertainty for the modeling. The Voyager 1 IRIS experimenters have inferred the presence of superrotating winds in the strato-

sphere, but there is no compelling reason to believe that this superrotation extends all the way up to the thermosphere. In view of the complexity of plasma conditions at Titan's orbit and of our lack of knowledge of the thermospheric rotation rate, we cannot hope to present a comprehensive quantitative model of the thermosphere. However, some aspects of the thermospheric structure, such as the location and temperature of the mesopause, are fairly insensitive to the uncertainties discussed above. In addition, we can set an upper limit to the exospheric temperature that can be achieved during a Titan day.

The thermal time scales that characterize the diurnal behavior of the thermosphere are discussed in section 2. In section 3, we present the input model atmosphere used to calculate the temperature profile and discuss the dominant heating and cooling mechanisms in the thermosphere. The temperature profiles obtained by integrating the heat transfer equation with and without electron heating are presented and discussed in section 4. In section 5 we investigate what implications the derived exospheric temperatures have for the neutral hydrogen torus.

2. Two Thermal Time Scales

The way in which thermospheric temperatures vary in time can be understood in terms of two time scales, which are related to the two principal cooling mechanisms. The first time scale is the response time associated with NLTE (vibrational relaxation) cooling due to acetylene and methane. It is roughly the time required for a given level in the thermosphere to relax to a new steady state in response to a change in the heating, if the only cooling mechanism is NLTE cooling. This response time is given by

$$\tau = \frac{\rho C_P}{\frac{\partial R}{\partial T}\Big|_T} \qquad (1)$$

where ρ is the mass density at the level of interest, C_p is the specific heat at constant pressure of N_2, R is the total NLTE cooling rate, and T is the temperature. At all altitudes considered in our models, the response time $\tau > 3$ years. Since the longest the thermospheric rotation period is likely to be is only 16 days, we may conclude that the temperature profile at any local time is not a steady-state profile but contains a good deal of memory of the temperatures at past local times.

The second time scale of interest is simply the conduction relaxation time for the thermosphere above a given altitude level. It is given by

$$\tau_c \sim \frac{L^2}{\kappa}$$

where L is a characteristic scale length of the system and κ is the effective heat diffusivity. It is not immediately clear how to choose L and κ for an inhomogeneous medium, but it is natural to choose L to be equal to the scale height at a given altitude, and to choose κ to be the heat diffusivity there. The time scale τ_c is then roughly the time required for conduction to bring the atmosphere above the altitude of interest into equilibrium with the lower layers.

We may estimate the density of the level where the conduction relaxation time is comparable to the thermospheric rotation period. It is given by

$$n \cong \frac{Pk}{mC_pH^2} \qquad (2)$$

where n is the number density, P the thermospheric rotation period, k the heat conductivity of N_2, m the mass of an N_2 molecule, and H the local scale height. If P is taken to be 16 days (corresponding to rigid corotation), then n ~ 8 x

10^{10} cm^{-3}, corresponding to an altitude of ~860 km above the surface. Therefore, we expect very little diurnal variation of the temperature below this altitude. The amplitude of the diurnal variation need not be small above this level. In our numerical calculations, we find that the actual level where the diurnal amplitude is ~5 K lies at $n \simeq 5 \times 10^{10}$ cm^{-3}, which tends to support the scaling arguments used here.

3. Model

For our model of the thermosphere, we use the results of the UVS solar occultation experiment, as reported by Smith et al. (1982), together with the photochemical model produced by Yung et al. (1982). Only three constituents of the upper atmosphere are important to the energy balance: N_2, CH_4, and C_2H_2. The mixing ratio of methane is taken to be 8% near the exobase and falls off to ~3% in the lower thermosphere. The acetylene mixing ratio drops from a value of 2% near the exobase to only 0.2% in the lower thermosphere, in accordance with the best-fit model presented in Smith et al. The initial input altitude profiles of these constituents are shown in Figure 1.

Two sources of energy are available to heat the thermosphere: solar energy and energetic magnetospheric electrons (Strobel and Shemansky, 1982). The solar flux

Figure 1. Altitude profiles of N_2, CH_4, and C_2H_2 chosen as initial input for model calculations. These profiles are recalculated simultaneously with the temperature profile.

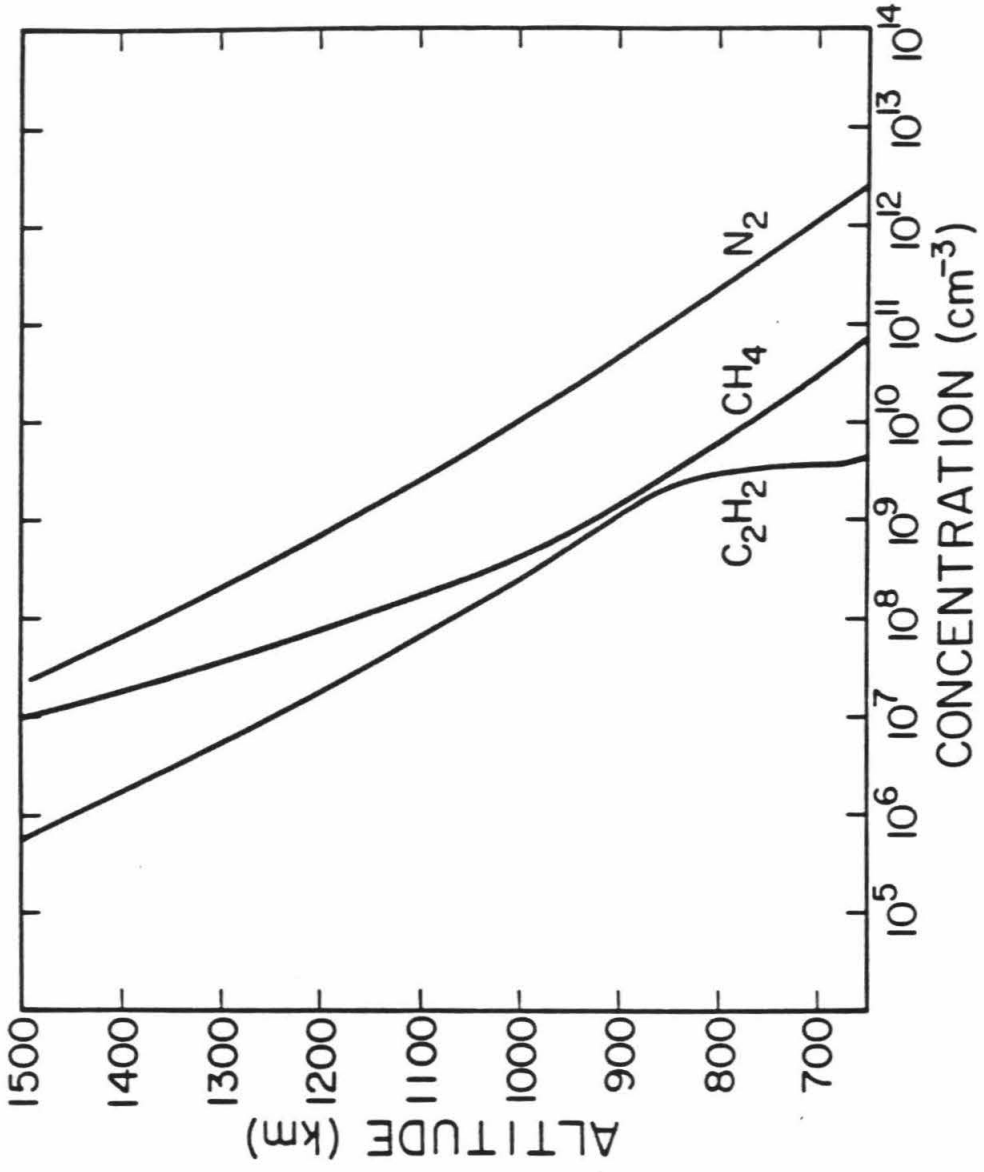
ALTITUDE (km)
1500
1400
1300
1200
1100
1000
900
800
700
CONCENTRATION (cm^{-3})
10^5 10^6 10^7 10^8 10^9 10^{10} 10^{11} 10^{12} 10^{13} 10^{14}
N_2
CH_4
C_2H_2

used in our model is taken from Mount and Rottman (1981). The flux in Lyman α incident on Titan is 5.5×10^9 photons cm^{-2} sec^{-1}. The bulk of the solar heating occurs through absorption of Lyman α by methane. Acetylene also contributes to the heating through its absorption at wavelengths less than 2000 A. Although nitrogen is an order of magnitude more abundant than methane, it only absorbs at wavelengths shortward of 1000 A, where the solar flux is low. Hence it contributes only ~10 percent to the solar heating.

Methane is dissociated at Lyman α via three channels (Slanger, 1982):

$$CH_4 + h\nu \rightarrow {}^1CH_2 + H_2 \qquad 40\%$$
$$\rightarrow CH_2 + 2H \qquad 50\%$$
$$\rightarrow CH + H_2 + H \qquad 8\%$$

The heating efficiency due to CH_4 absorption is calculated for each channel separately, and the weighted average over the channels is then taken to yield a mean heating efficiency. In each channel, the kinetic energy of the dissociation fragments as well as 50% of the CH_2 (or CH) recombination energy contributes to the local heating. Once the ${}^1CH_2$ radical is formed, it is rapidly quenched in collisions with N_2 to ${}^3CH_2$. Subsequently, two ${}^3CH_2$ radicals combine to produce C_2H_2 and H_2 (Yung et al., 1982). Since

C_2H_2 is chemically stable in the thermosphere, the reaction sequence terminates at this point. This set of reactions releases 2.8 eV of heat, and we include 50% of this recombination energy, or 1.4 eV, with the kinetic energy of the dissociation fragments when the heating efficiency is calculated. The recombination energy of H, however, does not contribute to the local heating as H is slow to react compared with the transport time scale. The average heating efficiency over the three methane channels is found to be 0.35 at Lyman α. It varies from a maximum of 0.47 at 1000 A to 0.32 at 1300 A. A similar analysis done for acetylene yields a mean heating efficiency of 0.45 between 1300 and 2000 A.

The solar heating is given by

$$H(r,\theta) = \Sigma_i \, n_i(r) \int d\lambda \, \varepsilon_i(\lambda) \, \sigma_i(\lambda) \, F_\infty(\lambda) \, e^{-\tau(r,\lambda)\chi(\theta)} \quad (3)$$

where r is the radial distance from Titan's center; n_i is the concentration, ε_i the heating efficiency, and σ_i the absorption cross section for constituent i; $F_\infty(\lambda)$ is the incident solar flux per unit wavelength; τ is the total normal optical depth; $\chi(\theta)$ is the Chapman function for solar zenith angle θ. The integration over wavelength is performed between 50 A and 2000 A.

Another energy source for heating the thermosphere is derived from electron impact on N_2. Some features of Titan's EUV emission spectra obtained during the Voyager 1 encounter suggest that some of the emission originates below the exobase (Strobel and Shemansky, 1982). The emission is consistent with being caused by a secondary electron energy distribution that is roughly a Maxwellian with an electron temperature of $T_e = 2 \times 10^5$ K. This temperature corresponds to an average electron energy of ~26 eV. Observation of the emission from the bright limb constrained the source altitude to be above ~1100 km. If photoelectrons produced ~25 Rayleighs of N_2 LBH emission, then the hemispheric-averaged energy flux below the exobase was ~0.01 erg cm^{-2} sec^{-1} at the time of the observation (Strobel, 1983). The altitude at which the source of this emission occurs, however, is still uncertain. Clearly, the actual electron energy flux incident on Titan should depend on the position of the satellite along its orbit. It is possible, in view of the complexity of the Saturnian magnetosphere at Titan's orbit, that this flux fluctuates substantially.

It is very difficult to calculate directly an effective heating efficiency for electron impact on N_2 that would correctly take into account the numerous physical and chemical processes that determine the fraction of energy that is ultimately dissipated as heat. Generally, this quantity will lie somewhere between 0.3 and 0.7. Since the

electron energy flux below the exobase is probably uncertain by a factor of 2 or so, it seems pointless at this time to specify a unique value for the electron heating efficiency. We will lump the uncertainty in the electron energy flux and the heating efficiency together and treat their product, $\varepsilon\phi$, as an adjustable parameter. The value of $\varepsilon\phi$ is not well constrained by the data. Nevertheless, we have included a model run which incorporates a plausible amount of electron heating for illustrative purposes. We model the electron heating in the simple parametrized form

$$E(r,\beta) = \varepsilon\phi(\beta)\, n(r)\, \sigma\, \exp[-\tau(r)] \qquad (4)$$

where

$$\tau(r) = \int_r^\infty n(r')\, \sigma\, dr' \qquad (4a)$$

is the absorption path length for electron scattering; σ is an "absorption" cross section; ε is the electron heating efficiency; ϕ is the hemispherically-averaged electron flux incident below the exobase; and β is the angle between the Saturn-Sun line and the position of Titan in its orbit. The cross-section σ is chosen to put the peak in the electron heating above the 1100 km level. The value used for σ is 4.2×10^{-17} cm^2. We consider the electron flux to have

reached its peak during Voyager 1 closest approach ($\beta = 0$), and allow $\phi(\beta) = 0$ on the night side. This model is intended to roughly account for the dayside-nightside asymmetry in the plasma flux-tube content observed by the Plasma Science experiments on Voyagers 1 and 2 (Bridge et al., 1981, 1982). It is a crude approximation in that it ignores the longitudinal asymmetry in the electron deposition at Titan observed by the UVS experiment (Broadfoot et al., 1981; Strobel and Shemansky, 1982). $\varepsilon\phi(\beta = 0)$ is taken to be 6×10^{-3} erg cm^{-2} sec^{-1}. Admitting a larger electron energy flux at the morning terminator causes the exospheric temperature to exceed the range allowed by the UVS observation.

The solar heating at a zenith angle of 60° is plotted as a function of altitude in Figure 2. The peak electron heating as a function of altitude is shown in Figure 3.

Heat can be removed from the thermosphere by NLTE cooling. The cool-to-space approximation (Chamberlain and McElroy, 1966) is quite adequate at all levels in our model. The 13.7 μ band of acetylene and, to a smaller degree, the 7.7 μ band of methane are responsible for the bulk of the NLTE cooling. Although methane is more abundant than acetylene in the thermosphere, acetylene dominates the NLTE cooling. This is true for two reasons: 1) The relaxation rate of the 13.7 μ acetylene band in collisions with N_2 is an order of magnitude greater than that of the methane 7.7 μ

Figure 2. Solar heating profile for solar zenith angle of 60°.

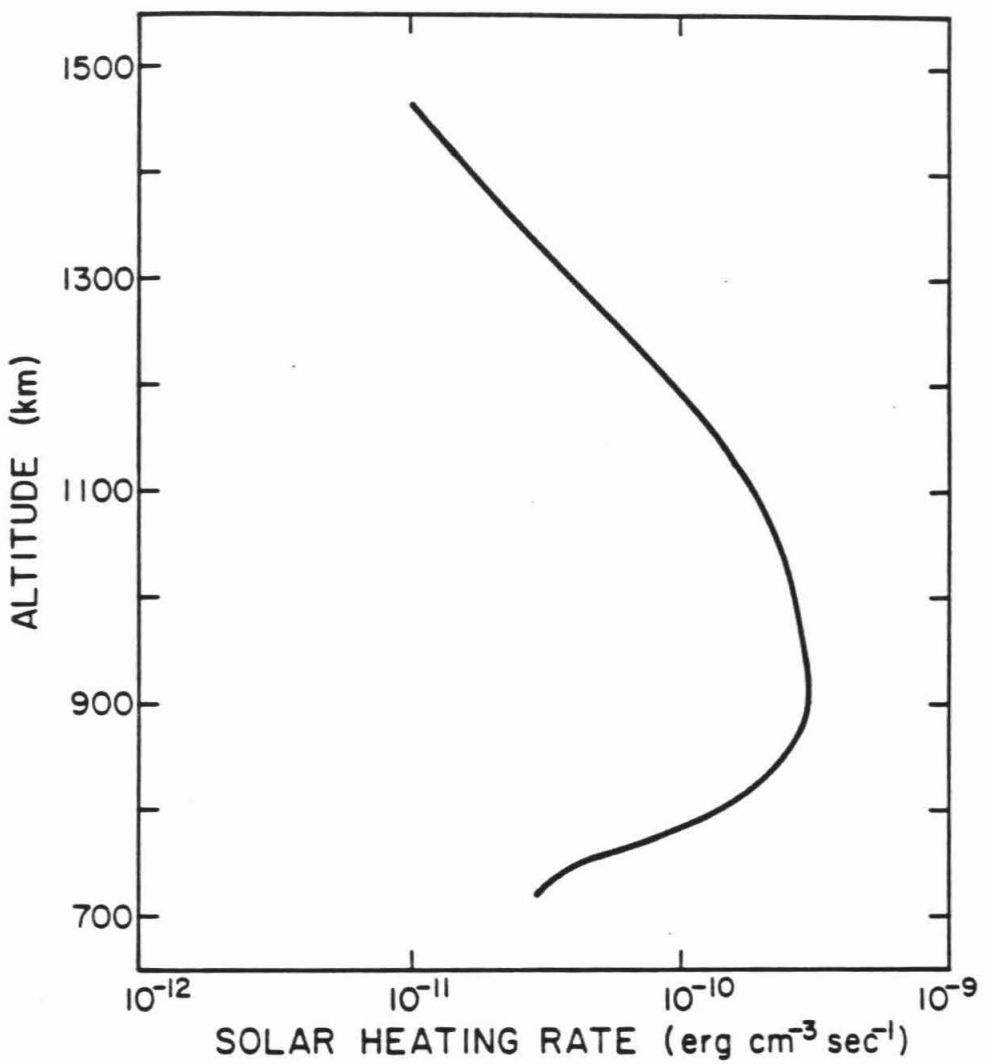
1500
1300
1100
900
700
ALTITUDE (km)
10^{-12}
10^{-11}
10^{-10}
10^{-9}
SOLAR HEATING RATE (erg cm^{-3} sec^{-1})

Figure 3. Peak electron heating profile.

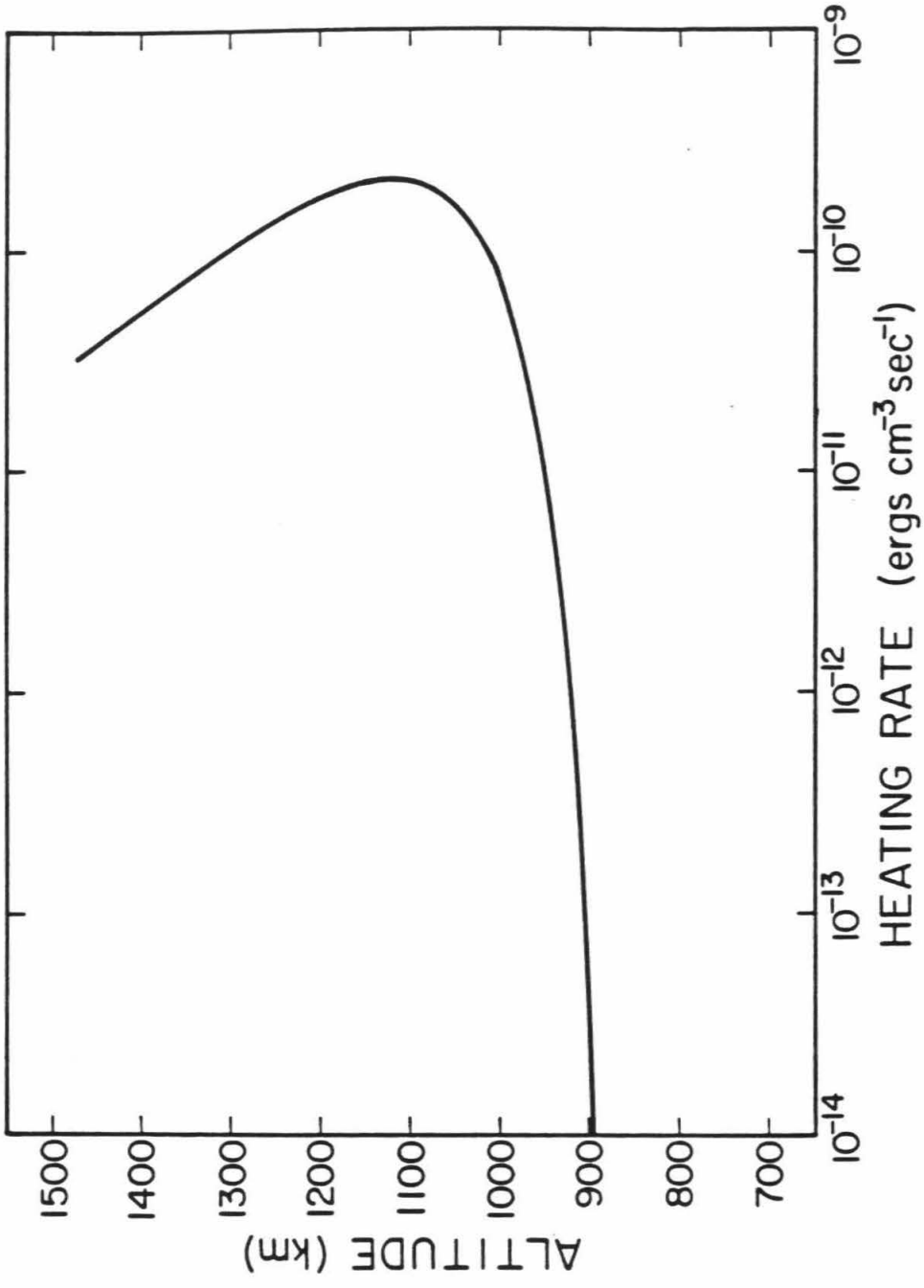
ALTITUDE (km)
1500
1400
1300
1200
1100
1000
900
800
700
HEATING RATE (ergs cm^{-3}sec^{-1})
10^{-14}
10^{-13}
10^{-12}
10^{-11}
10^{-10}
10^{-9}

band, for the same temperature and pressure (Yardley et al., 1970; Hager et al., 1981); 2) The lower energy associated with the 13.7 μ transition gives it a higher probability of excitation relative to the 7.7 μ transition by a factor of >100.

If we denote the total NLTE cooling rate per unit volume as R(r,T), then

$$R(r,T) = \Sigma_i \alpha_i h\nu_i \eta_i(T) e^{-h\nu_i/kT} f_i[n(r)]^2 Y_i(r). \quad (5)$$

Here ν_i is the frequency of a 13.7 μ or 7.7 μ transition, T is the kinetic temperature of the ambient gas, f_i is the mixing ratio of acetylene or methane, n is the total density, η_i is the collisional relaxation rate for the appropriate transition, α_i is the ratio of the statistical weights of the first excited state to the ground state, and Y_i is the net collisional bracket for the transition. For a transition whose optical depth is ≤1% of its thermalization depth, $Y_i \simeq 1$ (Avrett and Hummer, 1965). This is the case, at all altitudes of the model, for individual lines in the methane 7.7 μ band. Some lines in the acetylene 13.7 μ band, however, will have optical depths of $\tau \sim 100$, or as much as ~10% of the thermalization depth, at the lowest altitudes of the model. For these lines, the value of Y_i may differ substantially from unity. The value of Y_i for the strongest lines is approximately 0.7 at the mesopause

(740 km), and it decreases almost linearly to ~0.1 at the lower boundary of the model (680 km). We have determined, by numerical calculation, that the effect of setting $Y_i = 1$ in equation (5) is to underestimate the mesopause temperature by 7 K and to overestimate the lapse rate in the vicinity of the mesopause. (In particular, the temperature gradient at the lower boundary of the model as shown in Figure 5, is slightly superadiabatic. Allowing Y_i to differ from unity in equation (5) causes the lapse rate to become subadiabatic.) For simplicity, we have set $Y_i = 1$ in equation (5). Uncertainties associated with other aspects of the model are potentially more important.

The collisional relaxation rate of the 13.7 u band of C_2H_2 by N_2 has been determined at room temperature (Hager et al., 1981). We have not located any experimental data for this rate at other temperatures. Consequently, we have used data for the temperature dependence of C_2H_4 vibrational relaxation in N_2 (Wang and Springer, 1977), and expect that this data should give an adequate description of the temperature dependence of the C_2H_2-N_2 system. The collisional relaxation rate for C_2H_2-N_2 is taken to be

$$\eta_{C_2H_2}(T) = 5.08 \times 10^{-14}\ T^{1/2}\ e^{-28/T^{1/3}}\ cm^3/sec \qquad (6)$$

The collisional relaxation rate of the CH_4 7.7 μ transition in N_2 is given by (Wang and Springer, 1977)

$$\eta_{CH_4}(T) = 1.02 \times 10^{-13}\, T^{1/2}\, e^{-56/T^{1/3}} \quad cm^3/sec \qquad (7)$$

Heat is transported in the thermosphere by molecular conduction. For the conductivity of N_2 we use

$$k_{N_2}(T) = 42.7\, T^{0.69} + 2.61\, T - 355.6 \qquad (8)$$

which fits the data to within 5% between 80 K and 500 K (Weast, 1967). We neglect eddy heat conduction, since it is not clear to what extent the downward transport of heat due to eddies is able to balance or overcome the heat generated by viscous dissipation (Schoeberl et al., 1983; Walterscheid, 1981).

Given the heating and cooling rates, we calculate the vertical temperature profile as a function of local time by solving the time-dependent heat transfer equation;

$$\rho C_P \frac{\partial T}{\partial t} - \frac{1}{r^2} \frac{\partial}{\partial r} \left(r^2\, k_{N_2}(T) \frac{\partial T}{\partial r} \right) = H(r,t) + E(r,t) + R(r,t) \qquad (9)$$

where H(r,t) is the total solar heating rate, E(r,t) is the electron heating rate, and R(r,T) is the NLTE cooling rate. The specific heat at constant pressure, C_p, is used rather than C_v in equation (9) in order to take account of the general expansion or contraction of constant pressure surfaces in response to heating and cooling. This thermospheric "breathing" acts to reduce the diurnal temperature variation. Horizontal conduction and dynamical advection of heat are neglected in equation (9). These processes must reduce horizontal and vertical temperature gradients in the thermosphere, so the diurnal amplitude predicted by equation (9) must be considered as an upper limit.

Equation (9) must be supplemented with boundary conditions at the upper and lower boundaries of our model as well as with an initial temperature profile specified at a particular local time. The upper boundary condition is that the vertical temperature gradient must vanish above the exobase for all local times. We set the temperature to a constant value at the lower boundary, which occurs at an altitude of 680 km. Choosing the temperature at 680 km to be independent of time is supported by the scaling arguments presented in section 2. Numerical solution of equation (9) has shown that the vertical structure obtained at and above the mesopause is insensitive to the particular value chosen for the temperature at the lower boundary. Specifically,

the vertical temperature profile was found to be the same for lower boundary temperatures in the range 100-160 K.

To guess an initial temperature profile for the morning terminator, we impose a steady-state profile with a slightly reduced heating efficiency to account for the thermal inertia of the system. The validity of the initial guess is determined by the degree to which the solution returns to the initial profile after one rotation. Below 860 km, where the diurnal temperature variation is expected to be negligible, the initial profile should be that associated with diurnally-averaged heating conditions. A model run with diurnally-averaged heating showed the initial guess fulfilled this requirement.

The density profile at each local time is found simultaneously with the temperature profile by integrating the equation of hydrostatic equilibrium. The density at the lower boundary is chosen in order that the vertical profile at the morning terminator predicts a density at 1270 km of 2.6×10^8 cm^{-3}, in agreement with the UVS observation. The mixing ratios of the minor species are held fixed during the diurnal run.

Equation (9) is integrated numerically by a finite difference relaxation technique. The vertical resolution is 8 km, hence there are at least six steps per scale height in the model. The validity of the numerical solutions is

checked by requiring energy to be conserved both locally and globally.

4. Results and Discussion

The vertical structure of the thermosphere is found through simultaneous solution of the heat transfer equation and the equation of hydrostatic equilibrium. The value of the total density at the lower boundary is fixed by the condition that the density at 1270 km on the morning terminator agrees with the UVS solar occultation observation.

We have considered two model runs which differ only in the sources of heating for the thermosphere. Both models assume the rotation period of the thermosphere to be equal to Titan's orbital period (16 days). The first model considers the effects of solar heating alone, while the second introduces some amount of magnetospheric electron heating which might be representative of the conditions at Titan's orbit. The product $\varepsilon\phi(\beta = 0)$ for the electron heating is taken to be 6×10^{-3} erg cm^{-2} sec^{-1}. For a hemispherically-averaged electron energy flux below the exobase of 0.01 erg cm^{-2} sec^{-1}, this corresponds to an electron heating efficiency of 0.6. It must be emphasized here that the actual amount of electron heating at Titan and its diurnal variation are highly uncertain. The true value

of $\varepsilon\phi(\beta = 0)$ could be negligible, or it could be twice the value used in the model. Our purpose in including this model is to determine what, if any, effect the inclusion of an electron heat source has on the conclusions we make in this study.

In Figure 4 is shown the diurnal temperature variation at five altitudes when solar EUV radiation is the only source of heating. The data points shown on the curve for the 1270 km level represent the UVS solar occultation measurements at each terminator. The peak exospheric temperature is 216 K and occurs at ~1600 hrs local time, while the minimum of 159 K occurs at ~0400 hrs. The diurnal amplitude of the exospheric temperature is $\Delta T \sim 30$ K. Also shown in Figure 4 is the diurnal variation at 1270 km when electron heating is included. The peak exospheric temperature for this case is ~6 K warmer than for the solar heating case. Both models predict a temperature at 1270 km on the evening terminator which is 15 K warmer than the highest temperature allowed by the UVS observation. The dynamical response of the thermosphere or superrotation would be expected to reduce the diurnal amplitude of the temperature variation. Hence, it is possible that winds or superrotation of the thermosphere could explain the discrepancy at the evening terminator.

The diurnal average temperature and density profiles for solar heating only are shown in Figure 5. These profiles

Figure 4. Diurnal temperature variation at five altitudes -- solar heating only. The dashed curve for 1270 km is for the model which includes electron heating.

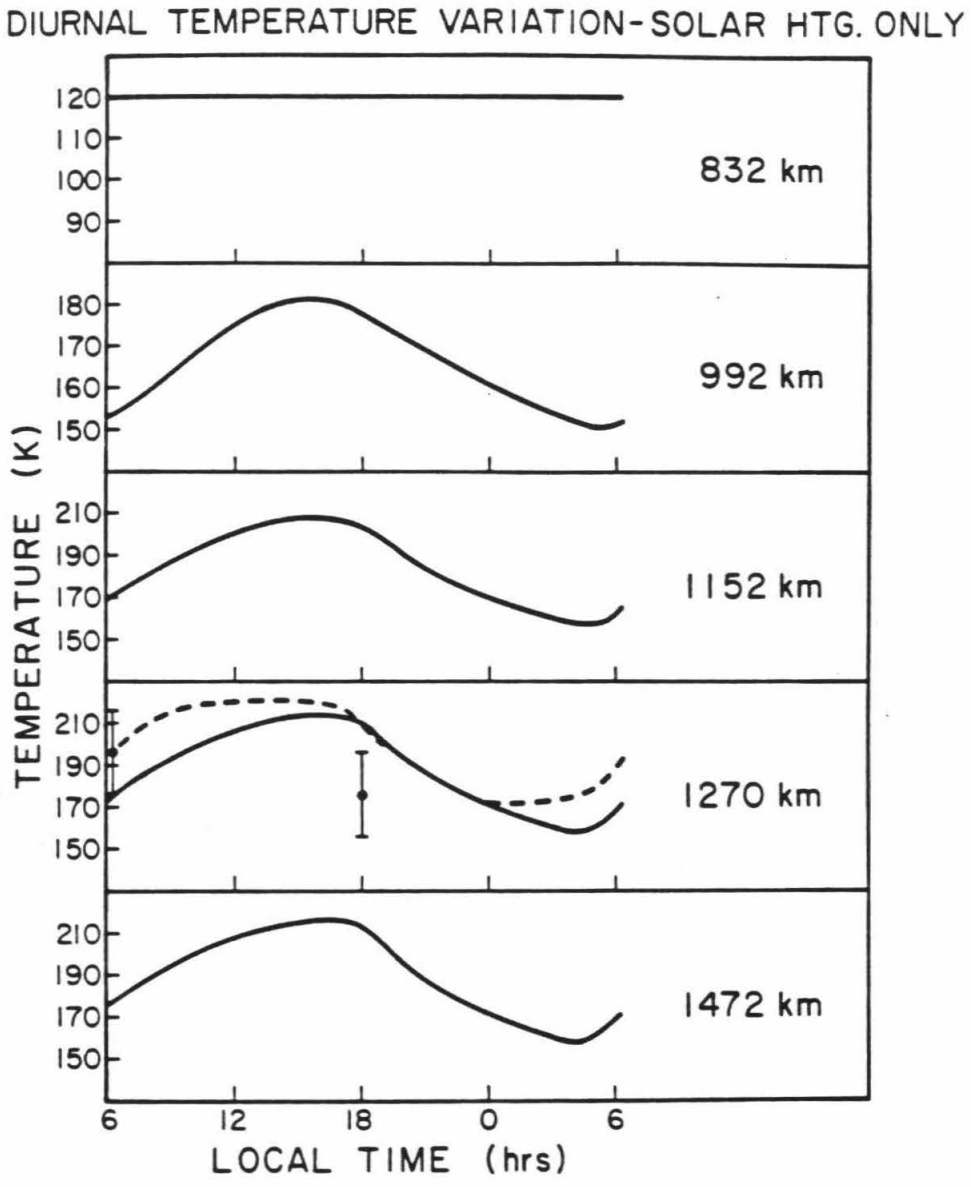
DIURNAL TEMPERATURE VARIATION-SOLAR HTG. ONLY
TEMPERATURE (K)
120
110
100
90
832 km
180
170
160
150
992 km
210
190
170
150
1152 km
210
190
170
150
1270 km
210
190
170
150
1472 km
6
12
18
0
6
LOCAL TIME (hrs)

Figure 5. Diurnal average temperature and density profiles for solar heating. Solid line -- temperature. Dashed line -- density.

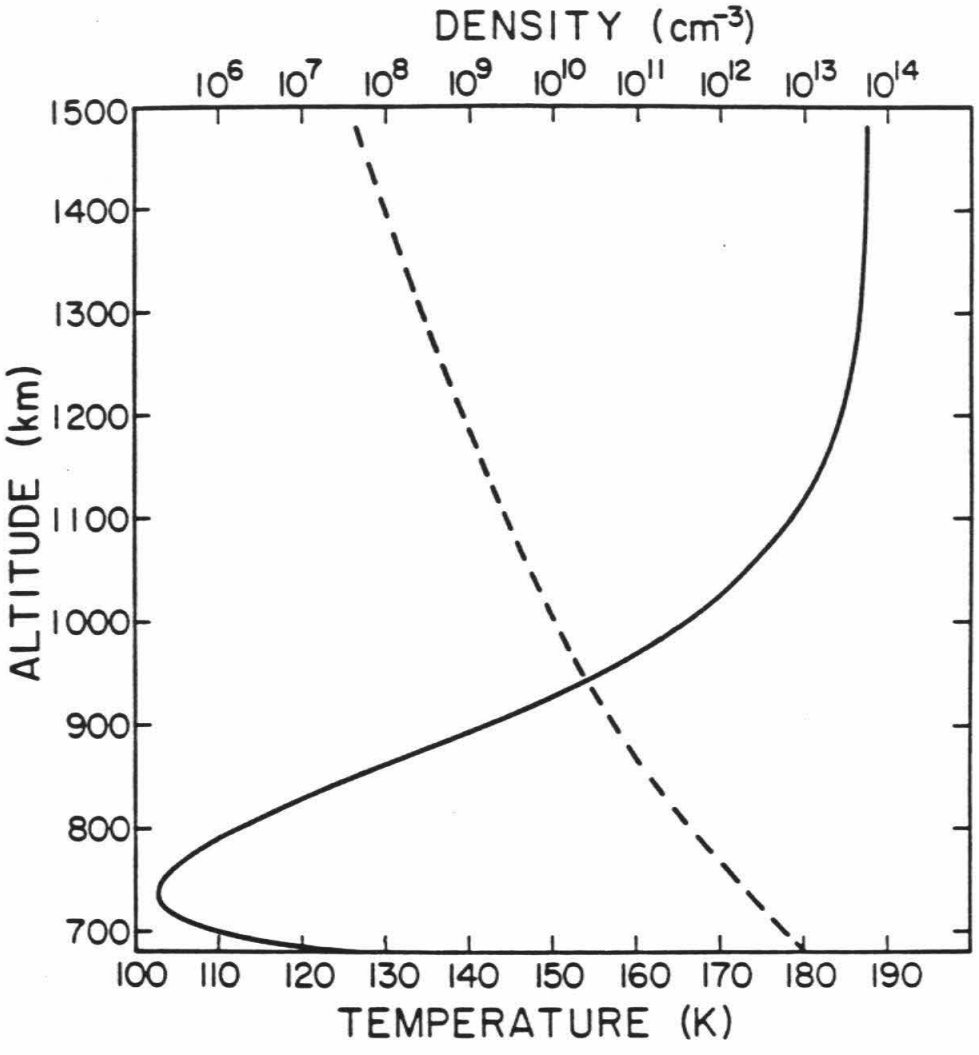
DENSITY (cm⁻³)
10⁶ 10⁷ 10⁸ 10⁹ 10¹⁰ 10¹¹ 10¹² 10¹³ 10¹⁴
1500
1400
1300
1200
1100
1000
900
800
700
ALTITUDE (km)
100 110 120 130 140 150 160 170 180 190
TEMPERATURE (K)

were found as solutions to the diurnal average of equation (9) and to the equation of hydrostatic equilibrium. In order to fit the observed density at 1270 km on the morning terminator, we find the density at the mesopause must be $n_m = 2.3 \times 10^{12}$ cm^{-3}. The mesopause is located at an altitude of 736 km, and is quite cold, T_m = 104 K (110 K if we include opacity effects, see eq. (5)). The diurnally-averaged exospheric temperature is 187 K. The diurnally-averaged exospheric temperature is ~10 K warmer than this when electron heating is included. The mesopause location and temperature are the same in both models, and are therefore insensitive to the assumptions made concerning electron heating.

Superrotation of the thermosphere would tend to reduce the amplitude of the diurnal variation and tend to increase the time lag of the response to the heating. If there is a diurnal temperature variation in the thermosphere, the average cooling rate at each level is greater than the cooling rate in a thermosphere with the same average temperature but no diurnal variation. This arises from the non-linear dependence of the cooling rate on temperature. As a consequence, a superrotating thermosphere with little diurnal temperature variation should exhibit a slightly higher diurnally-averaged exospheric temperature than a slower rotator. In the limit where Titan's thermosphere is considered to rotate so fast as to not experience any

diurnal variation, the average exospheric temperature is ≈190 K when only solar heating is included. If these models come close to describing the actual heating conditions at Titan, it appears unlikely that the exospheric temperature exceeds 225 K. A fluctuation in electron heating conditions (a local magnetospheric "storm," for example) could temporarily raise the exospheric temperature above this limit; however, the diurnal average of the exospheric temperature should stay below 225 K.

5. The Hydrogen Torus

The neutral hydrogen torus orbiting Saturn has been reported to extend radially between 8 R_s and 25 R_s, and to have a vertical half-thickness of 6 to 8 R_s (Sandel et al., 1982). It is interesting to consider to what extent the morphology of the torus is determined by simple Jeans escape of hydrogen from Titan.

In order to understand the torus geometry, it is necessary to know first whether or not collisions between atoms are important to the dynamics of the cloud. Recent data of the flux of neutral particles, detected by the LECP detector aboard Voyager 2 during the pre-encounter phase, has been used to set an upper limit of 100 cm^{-3} for the total neutral density in the torus (Ip, 1982). The mean free time for collisions, τ_C, is of order $\tau_C \sim (n\sigma v)^{-1}$,

where n is the torus density, σ is the collisional cross section, and v is the average relative velocity between atoms. The relative velocity between atoms is approximately $\sim e\Omega a$ where Ω is the orbital frequency, e the eccentricity, and a the semi-major axis of a typical particle orbit. Adopting values for a and Ω appropriate for particles near Titan, $\sigma \simeq 10^{-15}$ cm^2, and n $\simeq$ 100 cm^{-3}, the mean free collision time is of order $\tau_C \simeq 2 \times 10^7$ 1/e sec. Thus, for eccentricities $\lesssim$0.2, the collision time is greater than the torus lifetime of 10^8 sec estimated by Bridge et al. (1982). A collisionless treatment for the torus would then be appropriate. Due to the uncertainties involved in this analysis, however, the question of the importance of collisions in the torus must be left open for the present.

Smyth (1981) used a detailed computer model to study the structure of a collisionless torus. For a mean emission velocity for H atoms of 2.0 km sec^{-1}, corresponding to an exospheric temperature of ~240 K, the vertical half-thickness of the torus was found to be 1.5 R_s. This is considerably less than the 6-8 R_s inferred from the Voyager 1 and 2 UVS data. Therefore, if the torus is collisionless, it is much thicker than can be explained by simple thermal escape from a ~225 K exosphere.

The same conclusion can be reached if the torus is collision-dominated. A vertical scale height of 8 R_s implies a cloud temperature of 260 K (Sandel et al., 1982).

This is warmer than the 225 K upper limit we have set for the exospheric temperature. More complicated processes than thermal escape must be involved in forming a torus with half-thickness ~8 R_S. Among the viable alternatives are non-thermal escape from Titan, gravitational scattering in the torus, local heating in the torus, or perhaps a source of neutral hydrogen other than Titan.

The diurnal variation of Titan's thermospheric temperature and density profiles has been calculated by simultaneously solving numerically the heat transfer equation and the equation of hydrostatic equilibrium. It is found that the exospheric temperature is unlikely to exceed 225 K during a Titan day. Its diurnally-averaged value lies in the range 187-197 K. The amplitude of the diurnal variation is $\lesssim$30 K. The mesopause is fairly cold, ~110 K, and is located at a density of 2.3×10^{12} cm^{-3} (736 km). This density is greater than that expected at 736 km if Titan's upper atmosphere were isothermal above 190 km with a temperature of 170 K. This suggests that the temperature reaches a local maximum, warmer than 170 K, somewhere between 200 km and 700 km altitude. The vertical extent of the hydrogen torus is too large to be explained by simple thermal escape from a ~225 K exosphere. We conclude that other mechanisms must be more important in populating the torus.

Acknowledgements

The authors wish to thank A.P. Ingersoll, M. Allen, M.E. Summers, and G.R. Gladstone for helpful discussions. This research was supported by NASA grant NSG 7376 to the California Institute of Technology.

References

Avrett, E.H. and D.G. Hummer. Non-coherent scattering. MNRAS 130, 295, 1965.

Bridge, H.S., J.W. Belcher, A.J. Lazarus, R.L. McNutt, J.D. Sullivan, P.R. Gazis, R.E. Hartle, K.W. Ogilvie, J.D. Scudder, E.C. Sittler, A. Eviatar, G.L. Siscoe, C.K. Goertz, and V.M. Vasyliunas. Plasma observations near Saturn: Initial results from Voyager 2. Science 215, 563, 1982.

Bridge, H.S., J.W. Belcher, A.J. Lazarus, S. Olbert, J.D. Sullivan, F. Bagenal, P.R. Gazis, R.E. Hartle, K.W. Ogilvie, J.D. Scudder, E.C. Sittler, A. Eviatar, G.L. Siscoe, C.K. Goertz, and V.M. Vasyliunas. Plasma observations near Saturn: Initial results from Voyager 1. Science 212, 217, 1981.

Broadfoot, A.L., B.R. Sandel, D.E. Shemansky, J.B. Holberg, G.R. Smith, D.F. Strobel, J.C. McConnell, S. Kumar, D.M. Hunten, S.K. Atreya, T.M. Donahue, H.W. Moos, J.L. Bertaux, J.E. Blamont, R.B. Pomphrey, and S. Linick. Extreme ultraviolet observations from Voyager 1 encounter with Saturn. Science 212, 206, 1981.

Chamberlain, J.W. and M.B. McElroy. Martian atmosphere: The Mariner occultation experiment. Science 152, 1966.

Hager, J., W. Krieger, and J. Pfab. Collisional deactivation of laser-excited acetylene by H, HBr, N2, and CO. J. Chem. Soc., Faraday Trans. 77, 469, 1981.

Ip, W.H. On an estimate of the H_2 density in the atomic hydrogen cloud of Titan. Preprint, 1982.

Keating, G.M., J.Y. Nicholson III, and L.R. Lake. Venus upper atmosphere structure. J. Geophys. Res. 85, 7941, 1980.

Mount, G.H. and G.J. Rottman. The solar spectral irradiance 1200-3184 angstrom near solar maximum: July 15, 1980. J. Geophys. Res. 86, 9193, 1981.

Sandel, B.R., D.E. Shemansky, A.L. Broadfoot, J.B. Holberg, G.R. Smith, J.C. McConnell, D.F. Strobel, S.K. Atreya, T.M. Donahue, H.W. Moos, D.M. Hunten, R.B. Pomphrey, and S. Linick. Extreme ultraviolet observations from the Voyager 2 encounter with Saturn. Science 215, 548, 1982.

Schoeberl, M.R., D.F. Strobel, and J.P. Apruzese. A numerical model of gravity wave breaking and stress in the mesosphere. J. Geophys. Res. 88, 5249, 1983.

Slanger, T.G. Photodissociation channels at 1216 A for H_2O, NH_3 and CH_4, J. Chem. Phys. 77, 2432, 1982.

Smith, G.R. and D.F. Strobel. Titan's upper atmosphere: Composition and temperature from the EUV solar occultation results. J. Geophys. Res. 87, 1351, 1982.

Smyth, W.H. Titan's hydrogen torus. Ap. J. 246, 344, 1981.

Strobel, D.F. Upper atmosphere and torus of Titan. In Saturn, (T. Gehrels, Ed.), in press, 1983.

Strobel, D.F. and D.E. Shemansky. EUV emission from Titan's upper atmosphere: Voyager 1 encounter. J. Geophys. Res. 87, 1361, 1982.

Strobel, D.F. and G.R. Smith. On the temperature of the Jovian thermosphere. J. Atmos. Sci. 30, 718, 1973.

Walterscheid, R.L. Dynamical cooling induced by dissipating internal gravity waves. Geophys. Res. Lett. 8, 1235, 1981.

Wang, J.C.F. and G.S. Springer. Vibrational relaxation times in CH_4-N_2 and C_2H_4-N_2 mixtures. Progress in Astronaut. and Aeronaut. 51, 849, 1977.

Weast, R.C. (Ed.), Handbook of Chemistry and Physics, CRC, Cleveland, 1967.

Yardley, J.T., M.N. Fertig, and C.B. Moore. Vibrational deactivation in methane mixtures. J. Chem. Phys. 52, 1450, 1970.

Yung, Y.L., M. Allen, and J.P. Pinto. Photochemistry of methane, nitrogen and carbon monoxide on Titan: Abiotic synthesis of organic compounds. Paper presented at the First Symposium on Chemical Evolution and the Origin and Evolution of Life, Ames Research Center, NASA, August 2-4, 1982.